



**HAL**  
open science

# Implementation of the EPICS2017 electron-photon database in Geant4: developments and applications

Zhuxin Li

► **To cite this version:**

Zhuxin Li. Implementation of the EPICS2017 electron-photon database in Geant4: developments and applications. Physics [physics]. Université de Bordeaux, 2023. English. NNT : 2023BORD0185 . tel-04192465

**HAL Id: tel-04192465**

**<https://theses.hal.science/tel-04192465>**

Submitted on 31 Aug 2023

**HAL** is a multi-disciplinary open access archive for the deposit and dissemination of scientific research documents, whether they are published or not. The documents may come from teaching and research institutions in France or abroad, or from public or private research centers.

L'archive ouverte pluridisciplinaire **HAL**, est destinée au dépôt et à la diffusion de documents scientifiques de niveau recherche, publiés ou non, émanant des établissements d'enseignement et de recherche français ou étrangers, des laboratoires publics ou privés.

THÈSE PRÉSENTÉE

POUR OBTENIR LE GRADE DE

**DOCTEUR DE**

**L'UNIVERSITÉ DE BORDEAUX**

ÉCOLE DOCTORALE DES SCIENCES PHYSIQUES ET DE L'INGENIEUR

SPÉCIALITÉ : Astrophysique, Plasmas, Nucléaire

Par Zhuxin LI

**Implémentation de la base de données électrons-photons  
EPICS2017 dans Geant4 : développements et applications**

**Implementation of the EPICS2017 electron-photon database in Geant4:  
developments and applications**

Sous la direction de : Sébastien INCERTI  
(Co-directrice : Claire MICHELET)

Soutenue le 6 juillet 2023

Membres du jury :

M. INCERTI, Sébastien	Directeur de recherche	LP2IB/CNRS	Directeur de thèse
Mme. MICHELET, Claire	Maîtresse de conférences	Université de Bordeaux/LP2IB	Codirectrice de thèse
Mme. MAIGNE, Lydia	Maîtresse de conférences	Université Clermont Auvergne/LPC	Rapporteuse
M. EI BITAR, Ziad	Directeur de recherche	IPHC Strasbourg/CNRS	Rapporteur
Mme. GUATELLI, Susanna	Professeure associée	University of Wollongong, Australie	Examinatrice
Mme. SHEN, Hao	Professeure	Fudan University, Chine	Examinatrice
M. IVANTCHENKO, Vladimir	Professeur	Tomsk State University, Russie	Examineur
M. GIOVANNELLI, Jean-François	Professeur	Université de Bordeaux/IMS	Examineur



# Implémentation de la base de données électrons-photons EPICS2017 dans Geant4 : développements et applications

## Résumé :

Geant4 propose des modèles de physique complémentaires pour simuler les interactions des photons et des électrons avec la matière, en fonction de l'énergie. Un ensemble important de modèles à basse énergie (inférieure à 1 GeV) appelé « modèles Livermore » est disponible dans Geant4. Jusqu'à la version Geant4 10.6 (2021), ces modèles étaient basés sur trois bases de données du Lawrence Livermore National Laboratory (LLNL) pour les éléments de numéro atomique  $Z$  : 1-100, conçues dans les années 1990. Ces bases de données ont fait l'objet d'une mise à jour majeure sous l'égide de l'Agence Internationale de l'Energie Atomique (AIEA), aboutissant à une nouvelle version, EPICS2017 (Electron-Photon Interaction Cross Sections/Sections efficaces d'interaction électrons et photons).

Le premier objectif de cette thèse est de mettre à jour les modèles Livermore pour les photons et les électrons dans Geant4 avec la base de données EPICS2017. Après une introduction à la base de données EPICS2017 et aux modèles Livermore, présentés dans le chapitre 1, nous expliquons dans les chapitres 2 et 3 le travail réalisé pour les modèles Livermore photons et électrons, respectivement. Pour les photons, quatre processus ont été pris en compte : la création de paires/triplets, la diffusion Compton, l'effet photoélectrique et la diffusion Rayleigh. De nouvelles paramétrisations basées sur EPICS2017 ont été effectuées pour les fonctions de diffusion pour l'effet Compton, les sections efficaces des sous-couches pour l'effet photoélectrique et les facteurs de forme pour la diffusion Rayleigh. Une étude comparative entre la version Geant4 10.6, basée sur la base de données précédente, et Geant4 11.0, mise à jour avec EPICS2017, a montré que notre mise en œuvre améliorerait la précision des paramétrisations considérées. De plus, les coefficients d'atténuation massique calculés à partir des simulations Geant4 pour l'interaction totale des photons, et pour chaque processus, ont été comparés à la base de données XCOM et cette comparaison confirme la bonne concordance des résultats. Pour les électrons, une possible mise à jour du modèle décrivant l'ionisation et l'excitation a été considérée. Les études comparatives réalisées sur les sections efficaces et les pouvoirs d'arrêt n'ont pas montré de différences significatives entre EPICS2017 et les modèles Livermore existants. Par conséquent, l'implémentation de l'EPICS2017 pour les électrons s'est révélée non nécessaire.

Les modèles de basse énergie de Geant4 jouent un rôle important dans la modélisation des expériences de caractérisation des matériaux, notamment pour les expériences basées sur l'émission de rayons X, telles que l'imagerie par micro-tomographie protonique réalisée au LP2I Bordeaux. Dans ce contexte, le deuxième objectif de la thèse a été d'utiliser Geant4 pour simuler les expériences d'imagerie 3D par micro-tomographie protonique et quantifier la précision des méthodes de reconstruction. Le chapitre 4 décrit les simulations d'imagerie tomographique sur différents fantômes numériques, comprenant la partie supérieure d'un nématode *C. elegans* et une cible de fusion par confinement inertiel. La géométrie, la masse volumique et la composition de ces fantômes ont été dérivées de données expérimentales. La comparaison entre les images reconstruites, basées sur les résultats de simulation, et les fantômes originaux, pris comme référence, nous a permis d'évaluer l'exactitude des différentes méthodes de reconstruction testées et de vérifier les corrections d'atténuation des rayons X mises en œuvre dans le logiciel de reconstruction. Une précision  $\leq 4\%$  pour le phosphore, qui était l'élément le plus atténué, a été obtenue.

**Mots clés** : Simulation Geant4, EPICS2017, Livermore, micro-tomographie protonique, correction d'atténuation X



# Implementation of the EPICS2017 electron-photon database in Geant4: developments and applications

## Abstract:

Geant4 provides complementary and alternative physics models for the interaction of photons and electrons with matter, according to the energy range. An important set of models in the low energy (below 1 GeV) sub-package is the so-called Livermore models. Up to Geant4 10.6 version (2021), these models were based on three evaluated data libraries of the Lawrence Livermore National Laboratory (LLNL) for elements with atomic number  $Z$ : 1–100, designed in the 1990' s. These libraries have undergone a major updating process under the auspices of the International Atomic Energy Agency (IAEA), resulting in a new version, EPICS2017 (Electron-Photon Interaction Cross Sections).

The first objective of this PhD is to update Geant4 Livermore photon and electron models with the EPICS2017 database. After an introduction to the EPICS2017 database and Livermore models presented in chapter 1, we will explain in chapter 2 and 3 the implementation carried out for Livermore photon and electron models respectively. For photons, four processes were considered: gamma conversion, Compton scattering, photoelectric effect and Rayleigh scattering. New parameterizations based on EPICS2017 were performed for scattering functions of Compton effect, subshell cross-sections of the photoelectric effect and form factors of Rayleigh scattering. A comparative study between Geant4 10.6, based on the previous database, and Geant4 11.0, updated with EPICS2017 showed that our implementation improved the precision of the considered parameterizations. Moreover, the mass attenuation coefficients calculated from Geant4 simulations for both total photon interaction and each process were compared with XCOM database and found in good agreement. For electrons, the possible update of the ionisation and excitation model was considered. Comparative studies carried-out on cross-sections and stopping powers did not show any significant differences between EPICS2017 and the existing Livermore models. Consequently, the implementation of EPICS2017 for electrons is not required.

The low energy models of Geant4 play an important role in modelling the experiments of material characterization, especially for the experiments based on X-ray emission, such as proton micro-tomography imaging carried-out at LP2I Bordeaux. In this context, the second objective of my PhD is to apply Geant4 to simulate 3D proton micro-tomography experiments and quantify the accuracy of reconstruction methods. Chapter 4 describes tomography-imaging simulations on different phantoms including the upper part of a *C. elegans* nematode and an inertial confinement fusion target. The geometry, mass density and composition of the phantoms were derived from experimental data. The comparison between reconstructed images based on simulation results and original phantoms, taken as a reference, allowed us to assess the accuracy of the different reconstruction methods tested and to verify the X-ray attenuation corrections implemented in the reconstruction software package. An accuracy  $\leq 4\%$  for phosphorus, which was the most attenuated element, was obtained.

**Keywords:** Geant4 simulation, EPICS2017, Livermore, proton micro-tomography, correction of X-ray attenuation

---

## Unité de recherche

[UMR, 5797, Laboratoire de Physique des Deux Infinis Bordeaux, 19 Chemin du Solarium, 33170 Gradignan]



# Acknowledgements

---

I would like to express my deepest gratitude to my supervisors Claire Michelet and Sébastien Incerti, for their unwavering support, guidance and expertise throughout my doctoral journey. Their mentorship has been invaluable, and I am truly grateful for their patience, encouragement and belief in my abilities. Your listening ear, words of wisdom and uplifting spirit have helped me navigate through the challenges. I extend my heartfelt appreciation to the research participants, Vladimir Ivantchenko, Mihaly Novak, Susanna Guatelli, Daniel Beasley, Hao Shen and Shimei Wang, who generously shared their time and insights, without whom this study would not have been possible.

I am thankful to the staff and resources at LP2I Bordeaux for their assistance in analysis and logistical support, especially to Abdelaziz Habbouse and Catherine Sez nec. I would also like to acknowledge the support from my working team iRiBio, for their camaraderie and intellectual discussions.

I am grateful to the financial support provided by China Scholarship Council that enabled me to pursue my research. Furthermore, I express my thanks to the Geant4 collaboration community for providing me with access to necessary resources and facilities. I am truly grateful for the collaborative environment fostered by Fudan University. The collaboration has significantly contributed to the success of my doctoral research.

I would like to express my deep appreciation to my dear friend Xuewan. Thank you for being there for me, not just as a friend, but also as a confidante and a pillar of support. Your presence in my life has made this journey more meaningful, and I am grateful for your friendship.





# List of Abbreviations

---

<i>C. elegans</i>	<i>Caenorhabditis elegans</i>
EADL	Evaluated Atomic Data Library
EEDL	Evaluated Electron Data Library
EPDL	Evaluated Photon Data Library
EPICS2017	Electron Photon Interaction Cross Sections (2017)
FBP	Filtered Back Projection
ICF	Inertial Confinement Fusion
MLEM	Maximum Likelihood Expectation Maximization
NAAD	Normalized Average Absolute Deviation
NLXP	Non Linear X-ray production
NRMSD	Normalized Root Mean Squared Deviation
PIXE-T	Particle Induced X-ray Emission Tomography
RD	Relative Difference
ROI	Region Of Interest
STIM-T	Scanning Transmission Ion Microscopy Tomography
TR	TomoRebuild
XA	X-ray absorption



## Table of Contents

Résumé .....	3
Abstract .....	5
Acknowledgements .....	7
List of Abbreviations .....	9
Table of Contents .....	11
Chapter 1: Introduction .....	15
1. General introduction.....	15
2. Implementation of EPICS2017 for photon models .....	18
2.1. Photon processes in Geant4.....	18
2.2. Objective and method.....	19
3. Study of EPICS2017 and Livermore electron models.....	21
3.1. Electron processes in Geant4.....	21
3.2. Objective and method.....	22
4. Application to proton micro-tomography imaging.....	23
4.1. Purpose of proton tomography experiments.....	23
4.2. Objectives of Geant4 simulation .....	26
References .....	28
Chapter 2: Implementation of EPDL2017 for Livermore photon models.....	35
1. Introduction .....	35
2. Photon data in EPDL2017 .....	36
2.1. Data source .....	36
2.2. Physical quantities for photons in EPDL2017.....	36
2.3. Format of data .....	37
2.4. Main changes.....	40
3. Implementation of EPDL2017 .....	42
3.1. Gamma conversion.....	42
3.2. Compton scattering.....	44
3.3. Photoelectric effect.....	51

3.4. Rayleigh scattering .....	60
4. Comparative study of Geant4 photon models with respect to the XCOM data library .....	67
4.1. Method .....	67
4.2. Simulation uncertainty .....	67
4.3. Results .....	69
4.4. Discussion .....	76
5. Conclusion.....	77
References .....	79
Chapter 3: Updates in EEDL2017 and their impact on Livermore models.....	81
1. Introduction .....	81
2. Electron data in EEDL2017.....	82
2.1. Physical quantities for electrons.....	82
2.2. Format of data .....	83
2.3. Main changes.....	85
2.4. Comparative study of ionisation data .....	85
2.5. Comparison of excitation cross-sections .....	89
2.6. Discussion .....	91
3. Livermore ionisation model .....	92
3.1. Ionisation process in Geant4 .....	92
3.2. Calculation of ionisation cross-section.....	93
3.3. Calculation of continuous energy loss.....	93
4. Comparison of ionisation cross-section and stopping power between Livermore model and EEDL2017.....	95
4.1. Cross-section .....	95
4.2. Stopping power.....	97
5. Conclusion.....	104
References .....	105
Chapter 4: Application to proton micro-tomography imaging.....	107
1. Introduction .....	107

2. Design of the <i>stim_pixe_tomography</i> application .....	108
2.1. Principle of proton micro-tomography .....	108
2.2. Principle of STIM-T and PIXE-T experiments .....	110
2.3. Description of STIM-T and PIXE-T simulations .....	112
2.4. Selection of simulated data.....	120
3. Simulations.....	125
3.1. Numerical phantoms.....	125
3.2. Scan parameters.....	128
3.3. Physics models and optimization of duration.....	130
3.4. Parameters used for the selection of simulated data.....	131
4. Reconstruction of tomographic images .....	132
4.1. Reconstruction methods .....	132
4.2. Reconstructed image analysis.....	133
4.3. Construction of voxelized phantoms .....	133
5. Results .....	136
5.1. STIM-T analysis.....	136
5.2. PIXE-T analysis .....	144
6. Conclusion.....	156
References .....	158
Chapter 5: Conclusions and perspectives .....	161
Reference.....	166
Publications and Conferences .....	167
Publications .....	167
International conference .....	167
Oral contributions to collaboration meetings .....	167
International collaborations .....	169
Appendices .....	171
Appendix A: Atomic subshell designators .....	171
Appendix B: Simulation with constant proton energy .....	172



# Chapter 1: Introduction

---

## 1. General introduction

Based on the microbeam set-up of the AIFIRA (Applications Interdisciplinaires des Faisceaux d'Ions en Région Aquitaine) platform, the iRiBio (Ionising Radiation and Biology Interactions) team has been dedicated to the development of innovative techniques of irradiation and imaging for applications in biology. More precisely, the research seeks to accomplish the following objectives:

- The experimental study of the biological effects on living organisms or cells following exposure to ionising radiation. For this purpose, an ion microbeam line, where the delivered particles are controlled in time, quantity and space, is used for targeted irradiation at the cellular level [1-3].
- The detection, localization and quantification of chemical elements in biological samples exposed to exogenous compounds, such as pollutants, pharmacological drugs or nanoparticles, using 2D and 3D (tomography) quantitative imaging and analysis techniques [4-6].

In addition to experimental studies, the iRiBio team has initiated simulation activities based on Geant4, which is the most widely-used open-source Monte Carlo toolkit for the simulation of particle interactions with matter [7-9]. Originally designed to answer the needs of high energy physics, including the CERN experiments ATLAS and CMS, which discovered the Higgs boson in 2012, Geant4 has been found useful in other fields, such as space exploration and medical physics. With the development of parallel computing, the execution speed has been improved, leading to an expansion of the capabilities to describe more and more complex phenomena. The iRiBio group is involved in the Geant4 community not only as a user, but also as a developer, with the two distinct objectives previously mentioned:

- In order to simulate biological damages induced by ionising radiation at the cellular and sub-cellular scale, the team contributes to the development of the Geant4-DNA project, an extension of Geant4 [10]. The tracking capabilities at the sub-micrometer scale allows one to propose a complete simulation platform at the subcellular level;
- Furthermore, regarding imaging applications, the group has initiated since 2017 a simulation application to model proton micro-tomography imaging using Geant4 [11]. The primary goal of this project is to validate the accuracy of the reconstruction methods used to obtain tomographic images. For this, the tomography experiments have been simulated based on phantoms that have been defined according to experimental data. I was involved in this development from the beginning, during my internship in 2017 (internship of the end of studies at IMT Atlantique engineering school), by designing such phantoms.

For these reasons, the development of Geant4 simulation capabilities constitutes an indispensable component for the research undertaken in the iRiBio team. Driven by the need for accurate simulation,



the team devoted itself to developing the physics models used in Geant4. More precisely, each physical particle-matter interaction is described by a “physics process” class in Geant4. For each physics process, Geant4 provides several physics models, based on different assumptions (*e.g.*, theoretical, semi-empirical...) and applicable to different energy ranges or particle types. Therefore, a process is a fundamental concept in Geant4 that describes a physical interaction, while a model is a specific implementation of a process that takes into account various parameters and assumptions.

Geant4 provides a low energy electromagnetic sub-package dedicated to improve the accuracy and precision of simulations at low energies below 1 GeV [12, 13]. It includes complementary and alternative physics models according to the energy range, describing the electromagnetic interactions of photons (gamma conversion, Compton scattering, photoelectric effect and Rayleigh scattering), electrons and positrons (ionisation and bremsstrahlung) as well as annihilation for positrons. Two main sets of models are available in this sub-package:

- PENELOPE (PENetration and Energy LOss of Positrons and Electrons), version 2008 [14] implemented in C++;
- Livermore.

Livermore physics models constitute an important component of the low energy electromagnetic sub-package. They are based on three evaluated data libraries of the Lawrence Livermore National Laboratory (LLNL) for elements with atomic number  $Z = 1-100$ :

- EADL91 (Evaluated Atomic Data Library) [15];
- EEDL91 (Evaluated Electrons Data Library) [16];
- EPDL97 (Evaluated Photons Data Library) [17];

These models have been utilized in space radiation [18], archaeology [19] and medical physics applications, particularly in radiotherapy [20, 21], micro-and nanodosimetry [22, 23], imaging [24, 25] and spectrometry [26, 27]. Especially for medical physics, it is now possible to model the interaction of particles with living matter down to the molecular level (DNA), opening the way to a finer understanding of the mechanisms occurring during and following irradiation of biological media [28, 29]. For these reasons, the use of Geant4 in this field is now quickly growing, especially in the frame of the optimization of novel techniques of radiation therapy (for instance for image guided radiotherapy and for proton/hadron-therapy). Livermore models are also adopted in the Geant4-DNA set of physics models [10, 30-32] and by other medical physics oriented simulation platforms based on Geant4, like TOPAS (<http://www.topasmc.org>) [33, 34], GATE (<http://www.opengatecollaboration.org>) [35, 36] and GAMOS (<http://fismed.ciemat.es/GAMOS/>) [37, 38]. Comprehensive validations have been performed by the Geant4 community for photon cross-sections [39, 40] and more specifically for medical applications [41]. These benchmarking tests compared Livermore models with respect to different well-known databases, such as XCOM [42], SANDIA [43], Penelope [44], in the 1 keV - 100 GeV energy range. This range corresponds to the data available in the XCOM library. Poon *et al.* [45] carried out a validation specifically for water and tungsten in the 1 keV - 100 MeV energy range for

radiotherapy physics applications. Furthermore, some studies compared simulated results based on the Livermore models with XCOM data and experimental data for specific energy values, using radioactive sources in the keV - MeV energy range, for typical biological, geological and industrial materials [46-48]. All these publications have highlighted the applicability of the Livermore models.

However, the EPDL97, EEDL91 and EADL libraries, which were designed in the 1990's, have undergone a major update resulting in a new version, EPICS2017 (Electron-Photon Interaction Cross Sections) under the auspices of the International Atomic Energy Agency (IAEA) (<https://www-nds.iaea.org/epics/>) [49]. It is important that Geant4 takes into account these new databases to improve the precision and reliability of the Livermore models, which constitutes the first objective of this PhD project, *i.e.*, to implement EPICS2017 in Livermore photon and electron models.

The low energy models of Geant4 play an important role in modelling the experiments of material characterization, especially for the experiments based on X-ray emission, such as proton micro-tomography imaging carried-out at LP2I Bordeaux. In this context, the second objective of this PhD project is to apply Geant4 to simulate 3D proton micro-tomography experiments and quantify the accuracy of image reconstruction methods.

## 2. Implementation of EPICS2017 for photon models

### 2.1. Photon processes in Geant4

The first task of this PhD project consists in the implementation of the EPICS2017 database for photon models. In Geant4, four main physics processes are included for photons:

- **The gamma conversion:** when an incident photon energy exceeds  $2m_e c^2$  (1.022 MeV), the absorption and conversion of the incident photon into an electron-positron pair by an atom becomes energetically possible. However, to conserve the momentum simultaneously with total energy, the gamma conversion cannot occur in free space. It can only occur in the Coulomb field of a collision partner, either an atomic nucleus (pair production) or an orbital electron (triplet production) that can take up a suitable fraction of the momentum carried by the photon:
  - Pair production in the field of the nucleus: the extra momentum is absorbed by the atomic nucleus of the medium with two particles (electron and positron) generated;
  - Triplet production in the field of orbital electron: when an orbital electron picks up the extra photon momentum, the recoil energy may be significant. Three particles (two electrons and a positron) are generated. The threshold energy for triplet production is  $4m_e c^2$  (2.044 MeV).
- **Compton scattering:** an incident photon interacts with a loosely bound orbital electron of an atom. During the interaction, some of the energy and momentum of the photon is transferred to the electron, which recoils and is scattered in a different direction. The remaining energy of the photon is reduced, resulting in a scattered photon with lower energy than the original photon;
- **The photoelectric effect:** an incident photon is completely absorbed by an atomic electron, transferring all of its energy to the electron, which becomes free and is ejected from the atom. The electron is also known as photoelectron;
- **Rayleigh scattering:** an incident photon is elastically scattered by an atom as a whole with essentially the same energy as the original photon. The medium atoms are neither excited nor ionised and only the direction of the photon is changed.

In Geant4, for each physics process, several alternative physics models are available, grouped together in different sub-packages. Among those models, Livermore photon models are particularly suited to low energy, with recommended low limit down to 250 eV (except 1.022 MeV for pair production and 2.044 for triplet production). The upper limit depends on the process. Other processes such as Thomson scattering and Delbrück scattering are not specifically considered in Livermore models, but implemented in the JAEA (Japan Atomic Energy Agency) elastic scattering model [50].

## 2.2. Objective and method

The first objective of the PhD is to update Livermore photon models with the EPICS2017 database, which will be described in chapter 2. In Geant4, a physics model performs two major tasks:

- Computation of important physical quantities, such as cross-section and stopping power. For photon processes, the computation of cross-section is necessary to determine the probability of a photon undergoing a particular interaction as it passes through a material. It is performed by the *ComputeCrossSectionPerAtom()* method;
- Sampling of the final state after an interaction, performed by the *SampleSecondaries()* method. This method is called to generate the final state of the incident photon after a step interaction, such as its energy and momentum. It also simulates the generation of the secondary particle(s) produced as a result of the interaction.

In general, two different modelling approaches are involved in the implementation of the tasks:

- A model based on evaluated data libraries; it uses pre-determined data to calculate interactions between particles. These data libraries are typically compiled from experimental measurements and theoretical calculations. This is the case for the Livermore models.
- An analytical model, based on a set of mathematical formulas describing the physical processes in a simplified way, often resulting in faster simulations.

As mentioned before, Livermore models were developed based on evaluated data libraries (EADL91, EEDL91 an EPDL91). The data were employed in the computation of cross-sections and the sampling of the final state. The data were either directly used as tabulated values, after a conversion to a specific Geant4 format, or parameterized to improve speed and memory management, especially when the data vary smoothly.

In this context, the first step in the implementation of EPICS2017 is to identify the physical quantities that are used in the Livermore models and study if they are modified in EPICS2017 compared to previous versions.

The physical quantities related to Livermore photon models are as follows:

- For the gamma conversion:
  - The total cross-section.
- For Compton scattering:
  - The total cross-section;
  - The scattering function.
- For the photoelectric effect:
  - The total cross-section;
  - The subshell cross-section.
- For the Rayleigh scattering:
  - The total cross-section;

- The form factor.

Some of those data are directly read as tabulated input, such as total cross-section data for the gamma conversion process. Some data are used through a parameterization, such as the scattering function for Compton effect. For this reason, the implementation of EPICS2017 includes the update of both the tabulated values and the parameterizations. After the implementation, the whole update is validated by comparing the mass attenuation coefficients calculated from updated models with those calculated from previous models and XCOM database. This physical quantity was chosen because it is a fundamental physical quantity used for describing photon attenuation characteristics.

## 3. Study of EPICS2017 and Livermore electron models

### 3.1. Electron processes in Geant4

As mentioned in section 1, the implementation of EPICS2017 data for Livermore models is composed of two parts: the first one is for photons, introduced above and detailed in the next chapter; the second is for electrons. In Geant4, several processes of electron-matter interactions are implemented. As an electron travels through a material, the predominant interactions are due to Coulomb forces. The electron slows down and is deflected from its original path via inelastic or elastic collisions with atomic electrons and nuclei:

- **Inelastic collisions with atomic electrons** lead to excitation or ionisation of atoms. If the energy transferred to an orbital electron is sufficient for this orbital electron to escape from the atom, the ionisation occurs, leaving the atom ionised. If the transferred energy is only sufficient for this orbital electron to ascend to a higher shell, then the atom is excited, which corresponds to the excitation process. Both ionised and excited states are unstable, the vacant shell is rapidly filled by another orbital electron with the generation of photon(s) or Auger electron(s);
- **Elastic scattering from nuclei** occurs frequently, although not as often as electron collisions. In general, a negligible energy is transferred in these collisions, since the mass of a nucleus is larger than that of an electron. The incident electron may be elastically scattered once (single scattering) or many times (multiple scattering), being deflected from its original path;
- **Bremsstrahlung** is an inelastic process occurring in a material when a high energy (mainly above 1 MeV) electron is decelerated by the electric field of a charged nucleus. As a result, a fraction of the kinetic energy of the electron is emitted in form of X-rays.

In addition to the processes described above, Geant4 enables to simulate the following processes:

- Scintillation: an electron excites atoms or molecules in a medium, resulting in the emission of photons;
- Synchrotron radiation: a relativistic electron is accelerated or deflected in a magnetic field, resulting in the emission of photons;
- Cherenkov radiation: an electron travels through a medium at a speed greater than the phase velocity of light in that medium, resulting in the emission of electromagnetic radiation;

Among these processes, Livermore electron models are specifically designed for:

- Ionisation (including excitation process);
- Bremsstrahlung.

The other processes are handled by different models.

## 3.2. Objective and method

Livermore electron models were based on the EEDL91 database. Thus, the objective of our study is to reveal the changes in EPICS2017 compared to EEDL91, in order to see if there is a necessity for an update, which will be described in chapter 3. For this, we will first compare these two versions of the database to identify the main changes. Moreover, all the physical quantities used in Livermore electron models, which could be possibly impacted by these changes, will be studied and compared:

- Ionisation, excitation and bremsstrahlung cross-sections;
- Energy spectrum of the scattered electron due to ionisation;
- Energy spectrum of the emitted photon induced by bremsstrahlung.

## 4. Application to proton micro-tomography imaging

### 4.1. Purpose of proton tomography experiments

Chapter 4 of this thesis focuses on the application of Geant4 to proton tomography imaging. The first proton transmission tomography experiments were performed in 1976 by Cormack and Koehler with a 158 MeV proton beam of 2 mm diameter on polymer test samples [51]. These pioneering experiments showed a better density contrast compared to a conventional X-ray source. This observation was renewed by the first experiments on human organs, *in vitro*, also showing an advantage in terms of deposited dose [52], which refers to that the use of protons instead of X-rays reduces the dose required to achieve a given contrast sensitivity. In parallel, and in a very similar way, the development of micro beam technologies has opened the way to imaging microscopic samples using ions (generally protons) of a few MeV. Two techniques have been applied to proton micro-tomography:

- Scanning Transmission Ion Microscopy (STIM) displays the inner structure of the object by density contrast [53];
- Particle Induced X-ray Emission (PIXE) gives the distribution of chemical elements, with a high sensitivity, the limit of detection being  $\sim\mu\text{g/g}$  [54, 55].

The feasibility of 3D STIM imaging was first demonstrated by Pontau *et al.* on glass tubes and polymer foams [56]. The first experiment combining STIM and PIXE tomography (STIM-T and PIXE-T) was carried out by Schofield and Lefevre to reveal the composition of a scorpion sting [57] and showed the capability of these technique to produce the elemental concentration and mass density distributions of microscopic samples. Based on these techniques, a wide variety of applications have been developed [58]. LP2I Bordeaux laboratory has performed proton tomography experiments on *Caenorhabditis elegans* (*C. elegans*) nematodes in the frame of nanotoxicology studies. *C. elegans* is a transparent nematode about 1 mm in length living in most terrestrial ecosystems (<http://www.wormbook.org/>). Despite its small size, *C. elegans* presents many essential biological functions, such as digestion and reproduction. It is also a physiologically and genomically well-established model organism. Moreover, it is easy to cultivate and its rapid growth facilitates the study of the consequences of environmental exposure on thousands of individuals. For example, one adult worm can generate a population of about a thousand genetically identical worms in 10 days.

In the iRiBio team of the LP2I Bordeaux, one objective is to study the biological effects of metal nanoparticles, such as TiO<sub>2</sub> nanoparticles, which are widely used in food industry, cosmetics, textiles, paints, etc. More than 10,000 tons of TiO<sub>2</sub> are produced or imported into France each year. The exposure to the environment and human being by ingestion and inhalation draws the attention to potential biological effects, which are not yet understood. To understand the possible interactions with the living, *in situ* analyses were conducted by the iRiBio team at the cellular level. In this study, *C. elegans* exposed to TiO<sub>2</sub> nanoparticles were analyzed using STIM and PIXE techniques [59]. STIM gives access to the



worm morphology as well as its internal structure (Figure 1 - 1 (b)). By comparison to optical microscopy, STIM allows the identification of pharynx, intestine, embryos, gonads (Figure 1 - 1 (a) and Figure 1 - 1 (b)). This internal structure is also visible in PIXE images, mapping the elemental content of the worm. For biological samples, the high sensitivity of PIXE makes it suited to the analysis of minor minerals (such as phosphorus, sulfur, chlorine, potassium, calcium...) and trace elements (iron, copper, zinc...) involved in cellular metabolism. For example the distribution of phosphorus (green), calcium (blue) and titanium (red) are displayed in Figure 1 - 1 (c-e). PIXE images reveal a highly specific distribution of the elements in organs (*e.g.*, calcium in the intestine) suggesting a link between chemical anatomical structure and their functions.

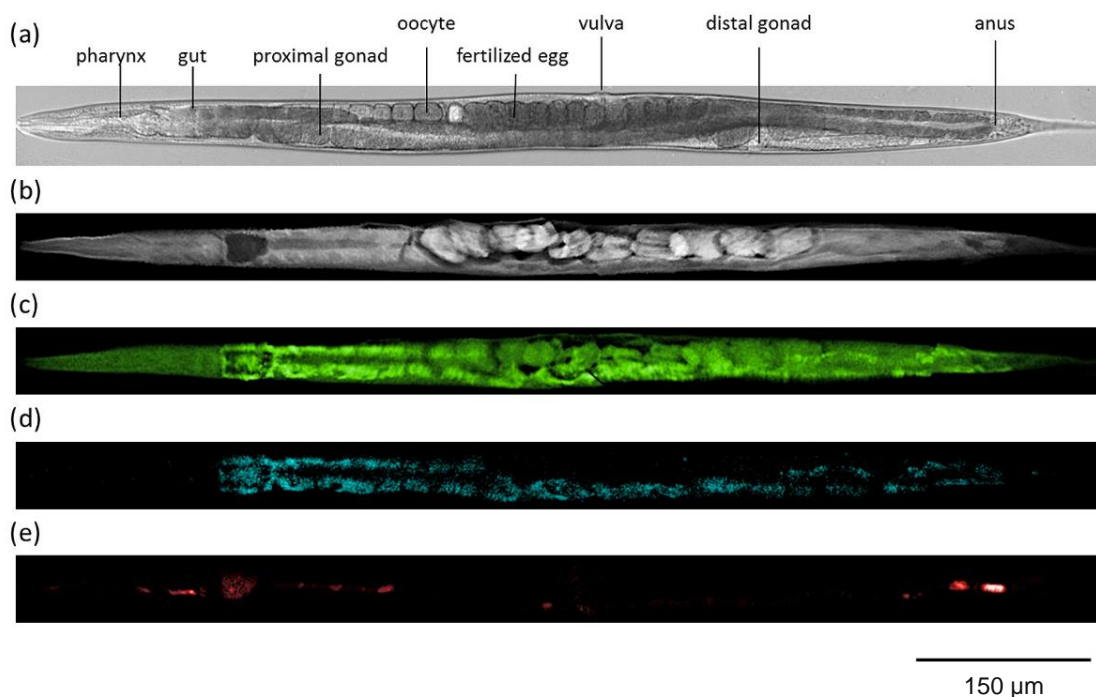


Figure 1 - 1. *In situ* chemical imaging of a lyophilized *C. elegans*: (a) Conventional optical microscopy. The different organs of the worm are depicted. (b) STIM image, also revealing, by mass density contrast, the different organs such as pharynx, intestine, embryos. (c-e) PIXE images showing the distribution of phosphorus (c, green), calcium (d, blue) and titanium (e, red). (Adapted from [59], page 62 ).

The images in Figure 1 - 1 are projections taken at a specific orientation, displaying namely the 2D distribution of areal mass expressed in  $\text{g}/\text{cm}^2$ . In order to obtain the three-dimensional structure of *C. elegans*, 3D proton tomography experiments were performed [60]. STIM-T provides the 3D distribution of the mass density (expressed in  $\text{g}/\text{cm}^3$ ) of the analyzed volume (Figure 1 - 2). PIXE-T gives access to the distribution of mass density (expressed in  $\text{g}/\text{cm}^3$ ) for each considered chemical element as shown in Figure 1 - 3. The reconstruction of these quantitative images is performed using a specific data reduction software, such as the TomoRebuild software package developed at LP2I Bordeaux [6].

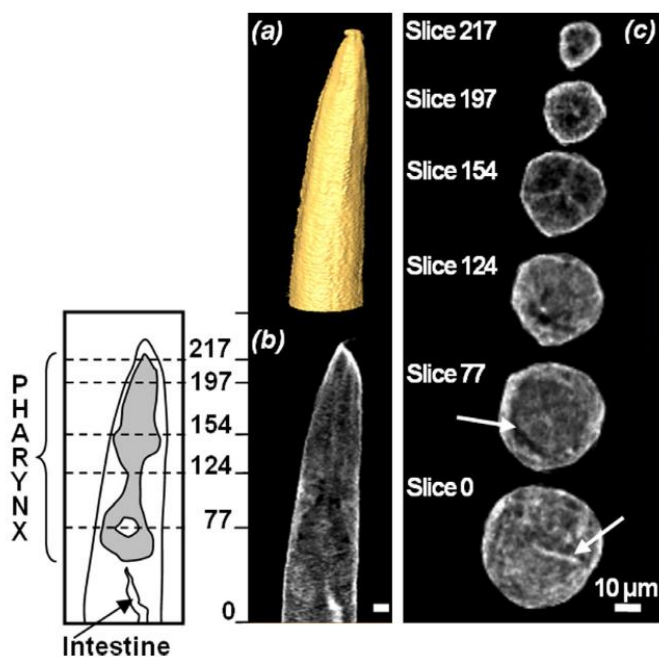


Figure 1 - 2. Three-dimensional structure of the upper part of the *C. elegans* sample of 255 STIM-T slices: 3D view of the outer surface of the worm (a); longitudinal slice through the reconstructed volume and its corresponding sketch (b); a few horizontal slices (c). The vertical position of the slices is indicated on the left. Reconstructed mass density values were coded on a linear gray scale ranging from 0.01 (black) to 0.9  $\text{g}/\text{cm}^3$  (white), except for slice 217, which presents denser regions, ranging from 0.25 to 1.1  $\text{g}/\text{cm}^3$ . (Adapted from [60], page 47).

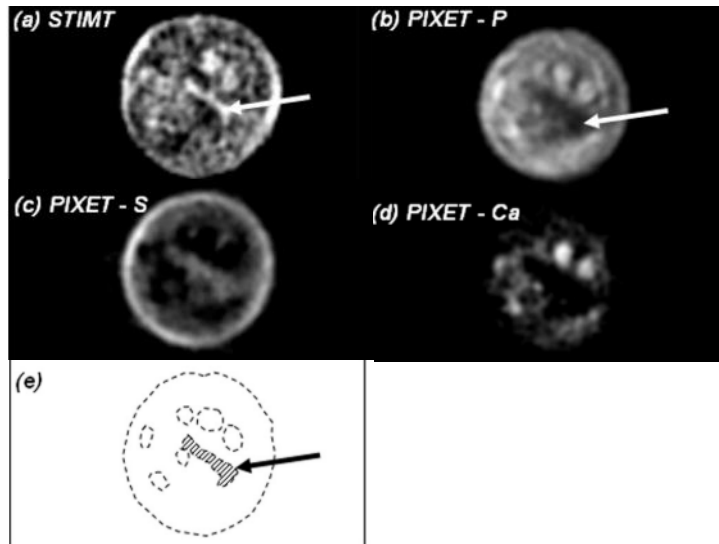


Figure 1 - 3. Tomographic reconstructions corresponding to the STIMT slice number 23 (a). The mass density STIM-T map was represented using a linear gray scale ranging from 0.09 (black) to 0.9 g/cm<sup>3</sup> (white). Element distributions are presented for phosphorus, sulfur and calcium (b–d). Several high-density spots, noticeable in the STIMT map and also visible especially in the PIXET-phosphorus map (b), were schematically represented in (e) to guides the eye. As in Figure 1 - 2, the intestine can be identified from the STIMT map (arrow) and was represented by a hatched area in (e). (Adapted from [60], page 48).

## 4.2. Objectives of Geant4 simulation

PIXE-T experiments consist of measuring the X-rays emitted by atoms of the material following their ionisation by incident protons. Two physical phenomena have an impact on the count of X-rays and eventually influence the accuracy of the quantification:

- Non-linear X-ray production (NLXP) effect, caused by the decrease of proton energy in the material, leading to a variation of the probability of ionisation, quantified by the ionisation cross-section;
- X-ray absorption (XA) in the material, on the way from the emitting point to the detector.

Even for small samples like *C. elegans*, the X-ray attenuation is not negligible. Previous experimental results on *C. elegans* have revealed that NLXP and XA effects can lead to about 40% attenuation of X-ray signal [6]. Thus, it is essential to consider a correction of the attenuation in the reconstruction process. NLXP and XA corrections have been implemented in TomoRebuild. One objective of my PhD project is to verify the accuracy of these corrections and the accuracy of the reconstruction methods in terms of quantification of mass density.

Previous proton tomography experiments carried out on reference micro-samples with known uniform mass density, have demonstrated the effectiveness of STIM-T in determining accurately the mass density of the analyzed materials [61, 62]. However, for PIXE-T, we would need a reference sample with certified density and composition, for chemical elements present at very low concentrations (mg/g

and even lower), similar to the case of biological samples. Such sample does not exist yet to our knowledge. So, a first attempt to evaluate the accuracy of PIXE-T was to compare the reconstruction results from different software packages on the same experimental data. For this, five reconstruction methods have been compared, from the DISRA [63], JPIXET [64, 65] and TomoRebuild software packages, which are the only codes able to take into account precise NLXP and XA corrections at present. This comparative study was performed on experimental data of *C. elegans*. The mass densities obtained by different methods were found similar [6, 66]. However, this was only a rough comparison of one package relative to the other. To perform a precise study, we chose to use Monte Carlo simulations to generate tomography data, similar to experiments, using *numerical* reference samples. For this, we decide to use the Geant4 toolkit.

Geant4 has been already applied to tomographic imaging in the medical field. Geant4 provides users with complete examples, which are ready-to-use applications. For instance, the *doiPET* so-called “advanced example” is available to simulate positron emission tomography (PET) imaging [67-69]. Moreover, specific applications related to PIXE experiments are provided. For example, the *xray\_fluorescence* advanced example reproduces various setups for PIXE or XRF experiments [70]. To answer our needs, the *TestEm5* extended example was well suited, as it is used to test the low energy physics processes in the energy range of a few MeV or below, typically involved in PIXE. *TestEm5* was used to simulate X-ray spectra that were compared with experimental spectra obtained from 1.5 MeV proton irradiation of thin foils of Au, Pt, GdF<sub>3</sub> and Fe. This study considered a proton beam at a fixed position. This comparison results showed the ability of Geant4 to predict X-ray spectra for these high-Z samples [26]. Based on this example, we developed a new application dedicated to proton micro-tomography imaging by STIM-T and PIXE-T. In chapter 4, we describe how we developed this application and the results we obtained from numerical phantoms, used as reference. Our purpose is to answer the following questions: are the reconstructed images comparable to the original phantom? Is the shape of the phantom preserved in the reconstructed images? Are the reconstructed density values accurate? What is the accuracy of the NLXP and XA corrections? The answers of these questions highly rely on Geant4’s functionalities.

Geant4 allows one to perform simulations under standard conditions, making it possible to validate the corrections totally and assess the accuracy of reconstruction process. Besides, Geant4 enables to make simulation under non-standard conditions, which are impossible to achieve in experiments, leading to the possibility to access specific simulated results. This will be detailed in chapter 4. Thanks to this remarkable feature, some benchmarking tests were designed so that the NLXP and XA corrections could be validated independently.

## References

- [1] Barberet P, Seznec H. Advances in microbeam technologies and applications to radiation biology. *Radiation Protection Dosimetry*. 2015;166(1-4):182-7. <https://doi.org/10.1093/rpd/ncv192>.
- [2] Muggiolu G, Pomorski M, Claverie G, Berthet G, Mer-Calfati C, Saada S, et al. Single  $\alpha$ -particle irradiation permits real-time visualization of RNF8 accumulation at DNA damaged sites. *Sci Rep*. 2017;7(1):41764. <https://doi.org/10.1038/srep41764>.
- [3] Torfeh E, Simon M, Muggiolu G, Devès G, Vianna F, Bourret S, et al. Monte-Carlo dosimetry and real-time imaging of targeted irradiation consequences in 2-cell stage *Caenorhabditis elegans* embryo. *Sci Rep*. 2019;9(1):10568. <https://doi.org/10.1038/s41598-019-47122-7>.
- [4] Simon M, Saez G, Muggiolu G, Lavenas M, Le Trequesser Q, Michelet C, et al. In situ quantification of diverse titanium dioxide nanoparticles unveils selective endoplasmic reticulum stress-dependent toxicity. *Nanotoxicology*. 2017;11(1):134-45. <https://doi.org/10.1080/17435390.2017.1278803>.
- [5] Le Trequesser Q, Saez G, Simon M, Devès G, Daudin L, Barberet P, et al. Multimodal correlative microscopy for in situ detection and quantification of chemical elements in biological specimens. Applications to nanotoxicology. *J Chem Biol*. 2015;8(4):159-67. <https://doi.org/10.1007/s12154-015-0133-5>.
- [6] Michelet C, Barberet P, Desbarats P, Giovannelli JF, Schou C, Chebil I, et al. An implementation of the NiftyRec medical imaging library for PIXE-tomography reconstruction. *Nucl Instrum Methods Phys Res B*. 2017;404:131-9. <https://doi.org/10.1016/j.nimb.2017.01.067>.
- [7] Agostinelli S, Allison J, Amako Ka, Apostolakis J, Araujo H, Arce P, et al. GEANT4—a simulation toolkit. *Nucl Instrum Methods Phys Res A*. 2003;506(3):250-303. [https://doi.org/10.1016/s0168-9002\(03\)01368-8](https://doi.org/10.1016/s0168-9002(03)01368-8).
- [8] Allison J, Amako K, Apostolakis J, Araujo H, Arce Dubois P, Asai M, et al. Geant4 developments and applications. *IEEE Trans Nucl Sci*. 2006;53(1):270-8. <https://doi.org/10.1109/tns.2006.869826>.
- [9] Allison J, Amako K, Apostolakis J, Arce P, Asai M, Aso T, et al. Recent developments in Geant4. *Nucl Instrum Methods Phys Res A*. 2016;835:186-225. <https://doi.org/10.1016/j.nima.2016.06.125>.
- [10] Incerti S, Baldacchino G, Bernal M, Capra R, Champion C, Francis Z, et al. The Geant4-DNA project. *Int J Model Simul Sci Comput*. 2010;1(02):157-78. <https://doi.org/10.1142/S1793962310000122>.
- [11] Michelet C, Li Z, Yang W, Incerti S, Desbarats P, Giovannelli J-F, et al. A Geant4 simulation for three-dimensional proton imaging of microscopic samples. *Phys Med*. 2019;65:172-80. <https://doi.org/10.1016/j.ejmp.2019.08.022>.
- [12] Ivanchenko V, Apostolakis J, Bagulya A, Abdelouahed HB, Black R, Bogdanov A, et al. Recent Improvements in Geant4 Electromagnetic Physics Models and Interfaces. *Prog Nucl Sci Technol*. 2011;2(0):898-903. <https://doi.org/10.15669/pnst.2.898>.
- [13] Ivanchenko VN, Incerti S, Allison J, Bagulya A, Brown JMC, Champion C, et al. Geant4 electromagnetic physics: improving simulation performance and accuracy. *SNA + MC 2013 - Joint*

- International Conference on Supercomputing in Nuclear Applications + Monte Carlo; 2014. <https://doi.org/10.1051/snamc/201403101>.
- [14] Salvat F, Fernández-Varea J, Sempau J. PENELOPE-2008: A Code System for Monte Carlo Simulation of Electron and Photon Transport. Workshop Proceedings; 2008; Barcelona, Spain. <https://www.oecd-nea.org/upload/docs/application/pdf/2019-12/nea6416-penelope.pdf>.
- [15] Perkins S, Cullen D, Chen M, Rathkopf J, Scofield J, Hubbell J. Tables and graphs of atomic subshell and relaxation data derived from the LLNL Evaluated Atomic Data Library (EADL), Z= 1--100. 1991. <https://doi.org/10.2172/10121422>.
- [16] Perkins S, Cullen D, Seltzer S. Tables and graphs of electron-interaction cross-sections from 10 eV to 100 GeV derived from the LLNL evaluated electron data library (EEDL), Z= 1-100. UCRL-50400. 1991;31:21-4. <https://doi.org/10.2172/5691165>.
- [17] Cullen DE, Hubbell JH, Kissel L. EPDL97: the evaluated photon data library 97 version. 1997. <https://doi.org/10.2172/295438>.
- [18] Inguibert C, Caron P, Gibaru Q, Sicard A, Balcon N, Ecoffet R. Surface Ionizing Dose for Space Applications Estimated With Low Energy Spectra Going Down to Hundreds of Electronvolt. IEEE Trans Nucl Sci. 2021;68(8):1754-63. <https://doi.org/10.1109/TNS.2020.3045200>.
- [19] Miceli A, Festa G, Gorini G, Senesi R, Andreani C. Pulsed neutron gamma-ray logging in archaeological site survey. Measurement Science and Technology. 2013;24(12):125903. <https://doi.org/10.1088/0957-0233/24/12/125903>.
- [20] Pope DJ, Cutajar DL, George SP, Guatelli S, Bucci JA, Enari KE, et al. The investigation of prostatic calcifications using  $\mu$ -PIXE analysis and their dosimetric effect in low dose rate brachytherapy treatments using Geant4. Phys Med Biol. 2015;60(11):4335-53. <https://doi.org/10.1088/0031-9155/60/11/4335>.
- [21] Poder J, Cutajar D, Guatelli S, Petasecca M, Howie A, Bucci J, et al. HDR brachytherapy in vivo source position verification using a 2D diode array: A Monte Carlo study. J Appl Clin Med Phys. 2018;19(4):163-72. <https://doi.org/10.1002/acm2.12360>
- [22] Lazarakis P, Incerti S, Ivanchenko V, Kyriakou I, Emfietzoglou D, Corde S, et al. Investigation of track structure and condensed history physics models for applications in radiation dosimetry on a micro and nano scale in Geant4. Biomed Phys Eng Express. 2018;4(2):024001. <https://doi.org/10.1088/2057-1976/aaa6aa>.
- [23] Liu R, Higley KA, Swat MH, Chaplain MAJ, Powathil GG, Glazier JA. Development of a coupled simulation toolkit for computational radiation biology based on Geant4 and CompuCell3D. Phys Med Biol. 2021;66(4):045026. <https://doi.org/10.1088/1361-6560/abd4f9>.
- [24] Beaudoux V, Blin G, Barbrel B, Kantor G, Zacharatou C. Geant4 physics list comparison for the simulation of phase-contrast mammography (XPulse project). Phys Med. 2019;60:66-75. <https://doi.org/10.1016/j.ejmp.2019.03.026>.
- [25] Li Z, Incerti S, Beasley D, Shen H, Wang S, Seznec H, et al. Accuracy of three-dimensional proton imaging of an inertial confinement fusion target assessed by Geant4 simulation. Nucl Instrum Methods Phys Res B. 2023;536:38-44. <https://doi.org/10.1016/j.nimb.2022.12.026>.

- [26] Incerti S, Barberet P, D ev es G, Michelet C, Francis Z, Ivantchenko V, et al. Comparison of experimental proton-induced fluorescence spectra for a selection of thin high-Z samples with Geant4 Monte Carlo simulations. *Nucl Instrum Methods Phys Res B*. 2015;358:210-22. <https://doi.org/10.1016/j.nimb.2015.06.029>.
- [27] Guembou Shouop CJ, Ndontchueng Moyo M, Nguelem Mekongtso EJ, Ousmanou M, Strivay D. Monte Carlo method for gamma spectrometry based on GEANT4 toolkit: Efficiency calibration of BE6530 detector. *J Environ Radioact*. 2018;189:109-19. <https://doi.org/10.1016/j.jenvrad.2018.03.015>.
- [28] Sakata D, Belov O, Bordage M-C, Emfietzoglou D, Guatelli S, Inaniwa T, et al. Fully integrated Monte Carlo simulation for evaluating radiation induced DNA damage and subsequent repair using Geant4-DNA. *Sci Rep*. 2020;10(1):20788. <https://doi.org/10.1038/s41598-020-75982-x>.
- [29] Sakata D, Hirayama R, Shin W-G, Belli M, Tabocchini MA, Stewart RD, et al. Prediction of DNA rejoining kinetics and cell survival after proton irradiation for V79 cells using Geant4-DNA. *Phys Med*. 2023;105:102508. <https://doi.org/10.1016/j.ejmp.2022.11.012>.
- [30] Incerti S, Ivanchenko A, Karamitros M, Mantero A, Moretto P, Tran H, et al. Comparison of GEANT4 very low energy cross section models with experimental data in water. *Med Phys*. 2010;37(9):4692-708. <https://doi.org/10.1118/1.3476457>
- [31] Bernal M, Bordage M, Brown J, Dav idkova M, Delage E, El Bitar Z, et al. Track structure modeling in liquid water: A review of the Geant4-DNA very low energy extension of the Geant4 Monte Carlo simulation toolkit. *Phys Med*. 2015;31(8):861-74. <https://doi.org/10.1016/j.ejmp.2015.10.087>.
- [32] Incerti S, Kyriakou I, Bernal M, Bordage M-C, Francis Z, Guatelli S, et al. Geant4-DNA example applications for track structure simulations in liquid water: A report from the Geant4-DNA Project. *Med Phys*. 2018;45(8):e722-e39. <https://doi.org/10.1002/mp.13048>.
- [33] Schuemann J, McNamara AL, Ramos-Mendez J, Perl J, Held KD, Paganetti H, et al. TOPAS-nBio: An Extension to the TOPAS Simulation Toolkit for Cellular and Sub-cellular Radiobiology. *Radiat Res*. 2019;191(2):125-38. <https://doi.org/10.1667/RR15226.1>.
- [34] Faddegon B, Ramos-Mendez J, Schuemann J, McNamara A, Shin J, Perl J, et al. The TOPAS tool for particle simulation, a Monte Carlo simulation tool for physics, biology and clinical research. *Phys Med*. 2020;72:114-21. <https://doi.org/10.1016/j.ejmp.2020.03.019>.
- [35] Costa GCA, Sa LVd, Bonifacio DAB. Application of GATE/Geant4 for internal dosimetry using male ICRP reference voxel phantom by specific absorbed fractions calculations for photon irradiation. *Biomed Phys Eng Express*. 2015;1(4). <https://doi.org/10.1088/2057-1976/1/4/045201>.
- [36] Pham QT, Anne A, Bony M, Delage E, Donnarieix D, Dufaure A, et al. Coupling of Geant4-DNA physics models into the GATE Monte Carlo platform: Evaluation of radiation-induced damage for clinical and preclinical radiation therapy beams. *Nucl Instrum Methods Phys Res B*. 2015;353:46-55. <https://doi.org/10.1016/j.nimb.2015.04.024>.
- [37] Arce P, Lagares JI, Harkness L, Desorgher L, Lorenzo Gd, Abreu Y, et al. GAMOS: An easy and flexible way to use GEANT4. 2011 IEEE Nuclear Science Symposium Conference Record; 2011 23-29 Oct. 2011. <https://doi.org/10.1109/NSSMIC.2011.6154455>.

- [38] Dubois PA, Thao NTP, Trung NT, Azcona JD, Aguilar-Redondo P-B. A tool for precise calculation of organ doses in voxelised geometries using GAMOS/Geant4 with a graphical user interface. *Pol J Med Phys Eng.* 2021;27(1):31-40. <https://doi.org/10.2478/pjmpe-2021-0005>.
- [39] Cirrone GAP, Cuttone G, Di Rosa F, Pandola L, Romano F, Zhang Q. Validation of the Geant4 electromagnetic photon cross-sections for elements and compounds. *Nucl Instrum Methods Phys Res A.* 2010;618(1-3):315-22. <https://doi.org/10.1016/j.nima.2010.02.112>.
- [40] Amako K, Guatelli S, Ivanchenko VN, Maire M, Mascialino B, Murakami K, et al. Comparison of Geant4 electromagnetic physics models against the NIST reference data. *IEEE Trans Nucl Sci.* 2005;52(4):910-8. <https://doi.org/10.1109/tns.2005.852691>.
- [41] Arce P, Bolst D, Bordage MC, Brown JMC, Cirrone P, Cortés-Giraldo MA, et al. Report on G4-Med, a Geant4 benchmarking system for medical physics applications developed by the Geant4 Medical Simulation Benchmarking Group. *Med Phys.* 2021;48(1):19-56. <https://doi.org/10.1002/mp.14226>.
- [42] Berger MJ, Hubbell J. XCOM: Photon cross sections on a personal computer. 1987. <https://doi.org/10.2172/6016002>.
- [43] Biggs F, Lighthill R. Analytical approximations for x-ray cross sections III. 1988. <https://doi.org/10.2172/7124946>.
- [44] Salvat F. PENELOPE-2018: A Code System for Monte Carlo Simulation of Electron and Photon Transport. Workshop Proceedings 2019; Barcelona, Spain. <https://doi.org/10.1787/32da5043-en>.
- [45] Poon E, Verhaegen F. Medical physics community Accuracy of the photon and electron physics in GEANT4 for radiotherapy applications. *Med Phys.* 2005;32(6):1696-711. <https://doi.org/10.1118/1.1895796>.
- [46] Medhat ME, Singh VP. Mass attenuation coefficients of composite materials by Geant4, XCOM and experimental data: comparative study. *Radiat Eff Defects Solids.* 2014;169:800-7. <https://doi.org/10.1080/10420150.2014.950264>.
- [47] Obaid SS, Sayyed MI, Gaikwad DK, Tekin HO, Elmahroug Y, Pawar PP. Photon attenuation coefficients of different rock samples using MCNPX, Geant4 simulation codes and experimental results: a comparison study. *Radiat Eff Defects Solids.* 2018;173(11-12):900-14. <https://doi.org/10.1080/10420150.2018.1505890>.
- [48] Al-Buriahi MS, Arslan H, Tonguç BT. Mass attenuation coefficients, water and tissue equivalence properties of some tissues by Geant4, XCOM and experimental data. *Indian Journal of Pure & Applied Physics.* 2019;57:433-7. <https://nopr.niscares.in/handle/123456789/47756>.
- [49] Cullen DE. EPICS2017: April 2019 status report. IAEA-NDS-228. 2019. <https://www-nds.iaea.org/epics/DOCUMENTS/2019-EPICS2017-Status.pdf>.
- [50] Omer M, Hajima R. Geant4 Physics Process for Elastic Scattering of  $\gamma$ -Rays. 2018. <https://jopss.jaea.go.jp/search/servlet/search?5059687>.
- [51] Cormack AM, Koehler AM. Quantitative proton tomography: preliminary experiments. *Phys Med Biol.* 1976;21(4):560-9. <https://doi.org/10.1088/0031-9155/21/4/007>.



- [52] Hanson KM, Bradbury JN, Koeppe RA, Macek RJ, Machen DR, Morgado R, et al. Proton computed tomography of human specimens. *Phys Med Biol.* 1982;27(1):25-36. <https://doi.org/10.1088/0031-9155/27/1/003>.
- [53] Michelet-Habchi C, Incerti S, Aguer P, Barberet P, Gontier E, Guinefolleau T, et al. 3D imaging of microscopic structures using a proton beam. 2003 IEEE Nuclear Science Symposium Conference Record (IEEE Cat No03CH37515); 2003 19-25 Oct. 2003. <https://doi.org/10.1109/NSSMIC.2003.1352267>.
- [54] Isabelle D. The PIXE analytical technique: principle and applications. *Radiat Phys Chem.* 1994;44(1-2):25-30. [https://doi.org/10.1016/0969-806X\(94\)90097-3](https://doi.org/10.1016/0969-806X(94)90097-3).
- [55] Johansson SA, Campbell JL, Malmqvist KG. Particle-induced X-ray emission spectrometry (PIXE). Wiley New York; 1995. <https://doi.org/10.1021/ja955314e>.
- [56] Pontau AE, Antolak AJ, Morse DH, Berkmoes AAV, Brase JM, Heikkinen DW, et al. Ion microbeam tomography. *Nucl Instrum Methods Phys Res B.* 1989;40-41:646-50. [https://doi.org/10.1016/0168-583X\(89\)91067-7](https://doi.org/10.1016/0168-583X(89)91067-7).
- [57] Schofield RMS, Lefevre HW. PIXE-STIM microtomography: Zinc and manganese concentrations in a scorpion stinger. *Nucl Instrum Methods Phys Res B.* 1992;72(1):104-10. [https://doi.org/10.1016/0168-583X\(92\)95289-4](https://doi.org/10.1016/0168-583X(92)95289-4).
- [58] Michelet C, Barberet P, Moretto P, Sez nec H. Development and applications of STIM- and PIXE-tomography: A review. *Nucl Instrum Methods Phys Res B.* 2015;363:55-60. <https://doi.org/10.1016/j.nimb.2015.08.070>.
- [59] Le Trequesser Q, Saez G, Devès G, Michelet C, Barberet P, Delville M-H, et al. In situ titanium dioxide nanoparticles quantitative microscopy in cells and in *C. elegans* using nuclear microprobe analysis. *Nucl Instrum Methods Phys Res B.* 2014;341:58-64. <https://doi.org/10.1016/j.nimb.2014.06.031>.
- [60] Habchi C, Gordillo N, Bourret S, Barberet P, Jovet C, Moretto P, et al. Beyond filtered backprojection: A reconstruction software package for ion beam microtomography data. *Nucl Instrum Methods Phys Res B.* 2013;295:42-9. <https://doi.org/10.1016/j.nimb.2012.10.006>.
- [61] Michelet-Habchi C, Incerti S, Aguer P, Barberet P, Gontier E, Grente K, et al. TomoRebuild: a new data reduction software package for scanning transmission ion microscopy tomography. *Nucl Instrum Methods Phys Res B.* 2005;231(1):142-8. <https://doi.org/10.1016/j.nimb.2005.01.048>.
- [62] Gordillo N, Habchi C, Daudin L, Sakellariou A, Delalée F, Barberet P, et al. Technical developments for computed tomography on the CENBG nanobeam line. *Nucl Instrum Methods Phys Res B.* 2011;269(20):2206-9. <https://doi.org/10.1016/j.nimb.2011.02.032>.
- [63] Sakellariou A, Jamieson DN, Legge GJF. Three-dimensional ion micro-tomography. *Nucl Instrum Methods Phys Res B.* 2001;181(1):211-8. [https://doi.org/10.1016/S0168-583X\(01\)00618-8](https://doi.org/10.1016/S0168-583X(01)00618-8).
- [64] Beasley DG, Marques AC, Alves LC, R.C. Fast simulation of Proton Induced X-Ray Emission Tomography using CUDA. *Nucl Instrum Methods Phys Res B.* 2013;306:109-12. <https://doi.org/10.1016/j.nimb.2012.12.053>.

- [65] Beasley DG, Alves LC, Barberet P, Bourret S, Devès G, Gordillo N, et al. A comparison of quantitative reconstruction techniques for PIXE-tomography analysis applied to biological samples. *Nucl Instrum Methods Phys Res B*. 2014;331:248-52. <https://doi.org/10.1016/j.nimb.2014.01.028>.
- [66] Michelet C, Barberet P, Devès G, Bouguelmouna B, Bourret S, Delville MH, et al. Quantitative reconstruction of PIXE-tomography data for thin samples using GUPIX X-ray emission yields. *Nucl Instrum Methods Phys Res B*. 2015;348:92-9. <https://doi.org/10.1016/j.nimb.2014.11.035>.
- [67] Tsuda T, Murayama H, Kitamura K, Yamaya T, Yoshida E, Omura T, et al. A four-layer depth of interaction detector block for small animal PET. *IEEE Trans Nucl Sci*. 2004;51(5):2537-42. <https://doi.org/10.1109/TNS.2004.835739>.
- [68] Hirano Y, Nitta M, Inadama N, Nishikido F, Yoshida E, Murayama H, et al. Performance evaluation of a depth-of-interaction detector by use of position-sensitive PMT with a super-bialkali photocathode. *Radiol Phys Technol*. 2014;7(1):57-66. <https://doi.org/10.1007/s12194-013-0231-4>.
- [69] Yoshida E, Tashima H, Shinaji T, Shimizu K, Wakizaka H, Mohammadi A, et al. Development of a whole-body dual ring OpenPET for in-beam PET. *IEEE trans radiat plasma med sci*. 2017;1(4):293-300. <https://doi.org/10.1109/TRPMS.2017.2703823>.
- [70] Mantero A, Bavdaz B, Owens A, Peacock T, Pia MG. Simulation of X-ray fluorescence and application to planetary astrophysics. 2003 IEEE Nuclear Science Symposium Conference Record (IEEE Cat No03CH37515); 2003 19-25 Oct. 2003. <https://ieeexplore.ieee.org/document/1352167>. <https://doi.org/10.1109/NSSMIC.2003.1352167>.



# Chapter 2: Implementation of EPDL2017 for Livermore photon models

---

## 1. Introduction

Considering the interactions of photons with matter, Livermore models are specifically designed for the simulation of four processes:

- The gamma conversion;
- Compton scattering;
- The photoelectric effect;
- Rayleigh scattering.

The objective of this chapter is to study the Livermore models based on EPDL97 and update them with EPDL2017. Therefore, in section 2, we will begin by presenting all the physical quantities for photons that are available in EPDL2017 and identify those that are directly or indirectly used in the Livermore models. In section 3, we compare EPDL2017 to EPDL97 in order to show the main modifications occurring for the physical quantities related to Livermore models. Subsequently, we detail the implementation for each process respectively. The implementation is validated, in section 4, through a comparative study with respect to the XCOM database. In this study, we calculate the mass attenuation coefficient for both total photon interaction and each process, using Geant4 10.6 (implementing EPDL97) and the updated models based on EPDL2017.

## 2. Photon data in EPDL2017

### 2.1. Data source

EPICS2017 [1] is the Electron Photon Interaction Cross Section library that provides the atomic data needed to perform electron and photon transport calculations for elements  $Z$ : 1-100, over the energy range 10 eV to 100 GeV. EPICS2017 is only applied for cold, neutral and isolated atoms. It is not suitable to handle density or molecular and other binding effects that may be important at low energy. EPICS2017 consists of three sub-libraries:

- EADL [2]: the Evaluated Atomic Data Library, describes the emission of electrons and photons following an ionising event, caused by either an electron or photon interaction on atoms;
- EEDL [3]: the Evaluated Electron Data Library, describes the interaction of electrons with matter;
- EPDL [4]: the Evaluated Photon Data Library, describes the interaction of photons with matter;

These three sub-libraries can be freely downloaded from the IAEA website: <https://www-nds.iaea.org/epics/>

### 2.2. Physical quantities for photons in EPDL2017

In EPICS2017, the sub-library describing the interaction of photons with matter is the Evaluated Photon Data Library (EPDL). EPDL2017 contains complete information for photon transport for  $Z$ : 1-100 and energies from 10 eV to 100 GeV. The tabulated physical quantities are as follows:

#### i) Coherent scattering

- Integrated cross section (barn);
- Form factor;
- Real and imaginary anomalous scattering factors;
- Average energy of the scattered photon (MeV).

#### ii) Incoherent scattering

- Integrated cross section (barn);
- Scattering function;
- Average energy of the scattered photon and recoil electron (MeV).

#### iii) Total photoelectric reaction

- Integrated cross section (barn);
- Average energy transferred to the residual atom, *i.e.*, local deposition (MeV);
- Average energy of the secondary photons and electrons (MeV).

#### iv) Photoelectric reaction, by subshell

- Integrated cross section (barn);
- Average energy transferred to the residual atom, *i.e.*, local deposition (MeV);

- Average energy of the secondary photons and electrons (MeV).

#### v) Pair production reaction

- Integrated cross section (barn);
- Average energy of the secondary electron and positron (MeV).

#### vi) Triplet production reaction

- Integrated cross section (barn);
- Average energy of the secondary electron and positron (MeV).

## 2.3. Format of data

### 2.3.1. Structure of data

EPDL2017 contains a series of tables in ASCII format. Each table starts with two header lines that contain the parameters related to the data (Figure 2 - 1). The two header lines are followed by a series of two-column physical data lines, one data point per line. Each table is terminated by an end of table line which is blank, except for a 1 placed in column 72 (column 72 is blank on all other lines in the table). Figure 2 - 1 presents an example of two complete tables contained in EPDL2017.

The screenshot shows a text editor window titled 'EPDL2017.ALL'. The data is as follows:

```

2808 9.388700000E+04 8.239800000E-15
2809 1.000000000E+05 7.736000000E-15
2810
2811 1000 7 0 1.00797 1807172 2 0.0 0.0 0.0 1
2812 73 11 91 0.0 1. 0.0 0.0 0.0
2813 1.360000000E-05 1.360000000E-05
2814 1.000000000E+05 1.360000000E-05
2815
2816 1000 7 9 1.00797 1807172 2 0.0 0.0 0.0 1
2817 73 10 91 0.0 1. 0.0 0.0 0.0
2818 1.360000000E-05 0.000000000E+00
2819 1.000000000E+05 1.000000000E+05
2820
  
```

Annotations in the image:

- first header line:** points to line 2811.
- second header line:** points to line 2812.
- physical data lines:** points to lines 2813 and 2814.
- end of table:** points to line 2815.
- first table:** label at the end of line 2811.
- second table:** label at the end of line 2816.

Figure 2 - 1. Example of two tables contained in EPDL2017. Header lines, end of table line and physical data lines are indicated (red arrows).

### 2.3.2. Information in the first header line

As an example, some detailed explanations are given in Figure 2 - 2 for the first header line extracted from the first table presented in Figure 2 - 1.

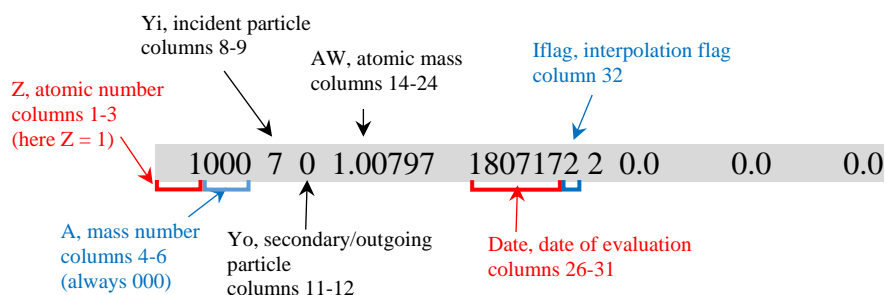


Figure 2 - 2. Information in the first header line of a table.

Additional information:

- For mass number, in EPICS2017,  $A = 000$  considering elemental data
- For **incident** particle (**i index**):
  - $Y_i = 0$ , no incident particle
  - $Y_i = 7$ , photon
  - $Y_i = 8$ , positron
  - $Y_i = 9$ , electron
- For secondary/**outgoing** particle (**o index**):
  - $Y_o = 0$ , no secondary/outgoing particle
  - $Y_o = 7$ , photon
  - $Y_o = 8$ , positron
  - $Y_o = 9$ , electron
- For date: YYMMDD
- For interpolation flag:
  - Iflag = 0, or 2, linear in x and y
  - Iflag = 3, logarithmic in x, linear in y
  - Iflag = 4, linear in x, logarithmic in y
  - Iflag = 5, logarithmic in x and y

### 2.3.3. Information in the second header line

Figure 2 - 3 illustrates the information contained in the second header line. As an example, we extract the second header line from the first table, presented in Figure 2 - 1.

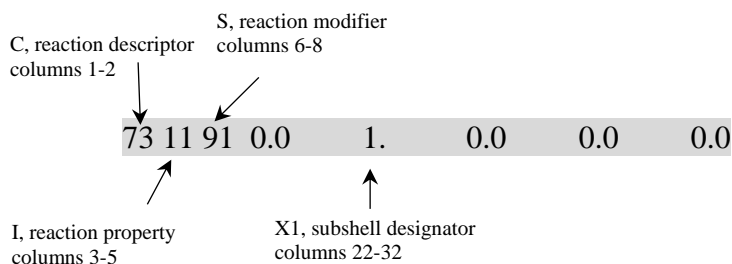


Figure 2 - 3. Information in the second line of a table.

Additional information:

- For reaction descriptor (it is equivalent to the notion of “physical process” used in Geant4):
  - C = 71, coherent scattering
  - C = 72, incoherent scattering
  - C = 73, photoelectric effect
  - C = 74, pair production
  - C = 75, triplet production
  - C = 93, whole atom parameters
- For reaction property:
  - I = 0, the table contains data about the integrated cross section
  - I = 10, the table contains data about the average energy of secondary/outgoing particle,  $Y_0$
  - I = 11, table contains data about the average energy to the residual atom
  - I = 941, table contains data about the form factor
  - I = 942, table contains data about the scattering function
  - I = 943, table contains data about the imaginary anomalous scattering factor
  - I = 944, table contains data about the real anomalous scattering factor
- For reaction modifier:
  - S = 0, no X1 field data required
  - S = 91, X1 field data required
- For X1, value depends upon the value of S:
  - S = 0, X1 = 0
  - S = 91, X1 = subshell designator. The subshells are specified by prescribed floating point designators, as shown in Appendix A,

### 2.3.4. Physical data lines

After the two header lines, the two-column physical data lines are given, with 10 significant digits. The physical quantities tabulated in these data lines depend on the value of the reaction property I, which is



indicated in the second header line (Figure 2 - 3). For example, in Figure 2 - 3,  $I = 11$ , which means that data correspond to the average energy to the residual atom.

## 2.4. Main changes

### 2.4.1. Format

The first change in EPICS2017, in its three sub-libraries EADL2017, EEDL2017 and EPDL2017, concerns the data format. Both EPICS2017 and its previous versions (EADL91, EEDL91 and EPDL97) are written in text format. However, data in EPICS2017 are in a format easier to read by computer codes, while previous data are not. The modification consists in adding a “E” for the power of 10, as shown in Figure 2 - 4.

		EEDL97							EEDL2017									
		Energy (MeV)			Cross-section (barn)				Energy (MeV)			Cross-section (barn)						
Header lines	→	1000	7	0	1.007970+0	9707045	2	0.0	1000	7	0	1.00797	1807172	2	0.0			
		72	0	0	0.0		0.0		0.0		72	0	0	0.0		0.0		0.0
Data lines	→	1.000000-6	9.562300-8						1.000000000E-06	9.562300000E-08								
		1.258900-6	1.515500-7						1.059248390E-06	1.072900000E-07								
		1.584900-6	2.401900-7						1.105977190E-06	1.169660000E-07								
		1.995300-6	3.806800-7						1.142371710E-06	1.247910000E-07								
		2.511900-6	6.033300-7						1.199221310E-06	1.375210000E-07								
		3.162300-6	9.562200-7						1.258900000E-06	1.515500000E-07								
		3.981100-6	1.515500-6						1.333502680E-06	1.700420000E-07								
		5.011900-6	2.401900-6						1.392341890E-06	1.853770000E-07								
		6.309600-6	3.806700-6						1.438168870E-06	1.977790000E-07								
		7.943300-6	6.033200-6						1.509752920E-06	2.179550000E-07								
		1.000000-5	9.561800-6						1.584900000E-06	2.401900000E-07								
		1.258900-5	1.515400-5						1.678817360E-06	2.694980000E-07								
		1.584900-5	2.401700-5						1.752889910E-06	2.938040000E-07								
		1.995300-5	3.806400-5						1.810581310E-06	3.134610000E-07								
		2.511900-5	6.032600-5						1.900698010E-06	3.454390000E-07								
		3.162300-5	9.560700-5						1.995300000E-06	3.806800000E-07								
		3.981100-5	1.515200-4						2.113521840E-06	4.271290000E-07								
		5.011900-5	2.401300-4						2.206762740E-06	4.656480000E-07								
		6.309600-5	3.805500-4						2.279383080E-06	4.968010000E-07								
		7.943300-5	6.027800-4						2.392818920E-06	5.474800000E-07								
	1.000000-4	9.546400-4						2.511900000E-06	6.033300000E-07									
	1.258900-4	1.512000-3						2.660740550E-06	6.769490000E-07									
	1.584900-4	2.392700-3						2.778130640E-06	7.380000000E-07									
								2.869559710E-06	7.873750000E-07									

Figure 2 - 4. Data lines format in EPDL97 and EPDL2017.

### 2.4.2. Interpolation

The second change in EPICS2017 (EADL2017, EEDL2017 and EPDL2017) is the way that the tabulated data are interpolated. The data are interpolated linearly in EPICS2017, whereas logarithmic interpolation was used in previous versions (EADL91, EEDL91 and EPDL97). As a result, there is generally an increase in the number of tabulated points in EPICS2017. As mentioned before, in Geant4, the data are either directly used as tabulated values, after a conversion to a specific Geant4 format, or parameterized to improve speed and memory management, especially when the data vary smoothly. The

increase in the number of points in EPICS2017 thus allows the existing parameterizations to be improved.

### **2.4.3. Modification of physical quantities**

The third major modification in EPDL2017 is the update of the atomic binding energies, with the purpose of better reproducing fluorescence X-ray energies [3, 4]. This update results in the change of cross-sections for the photoelectric and Rayleigh scattering, as discussed in sections 3.3 and 3.4.

The physical quantities used for Livermore photon models are as follows:

- For the gamma conversion:
  - The total cross-section data.
- For Compton scattering:
  - The total cross-section data;
  - The scattering function data.
- For the photoelectric effect:
  - The total cross-section data;
  - The subshell cross-section data.
- For Rayleigh scattering:
  - The total cross-section data;
  - The form factor data.

The update for those physical quantities is described in section 3.

## 3. Implementation of EPDL2017

### 3.1. Gamma conversion

#### 3.1.1. Physical process

The gamma conversion occurs when a photon interacts with a strong electric field from either a nucleus (pair production) or an electron (triplet production) of the atom. Gamma conversion can possibly occur only above a photon energy threshold of 1.022 MeV for pair production, and above 2.044 MeV for triplet production. At high photon energies, above 10 - 100 MeV, depending on the  $Z$  of material, it becomes the dominant process. At very high energies, pair and triplet production show very simple atomic number ( $Z$ ) dependence: pair production varies as  $Z^2$ , and triplet production as  $Z$ . For this reason, the contribution of triplet production is more important for low  $Z$  elements. For example, for hydrogen ( $Z = 1$ ), the cross-sections of pair and triplet production are almost equal, while for lead ( $Z = 82$ ), pair production is roughly 82 times larger than triplet production.

#### 3.1.2. Description of data

For the gamma conversion process, only the cross-section data of EPDL are used in the Livermore model and need to be updated. EPDL2017 contains tabulated cross-section data for pair and triplet production. The only difference compared with EPDL97 is that more points (about three times) are contained in EPDL2017 in order to allow the use of linear interpolation between tabulated points, whereas it was a logarithmic interpolation for EPDL97. We performed a comparison of cross-sections for pair and triplet production for all the elements ( $Z$ : 1-100). Three materials (H, Al, Pb) were arbitrarily chosen only for illustration (Figure 2 - 5). It was stated [4] that the cross-sections of EPDL2017 were in a close agreement with those available in Penelope and with XCOM data for all elements, within a maximal relative difference smaller than 1%.

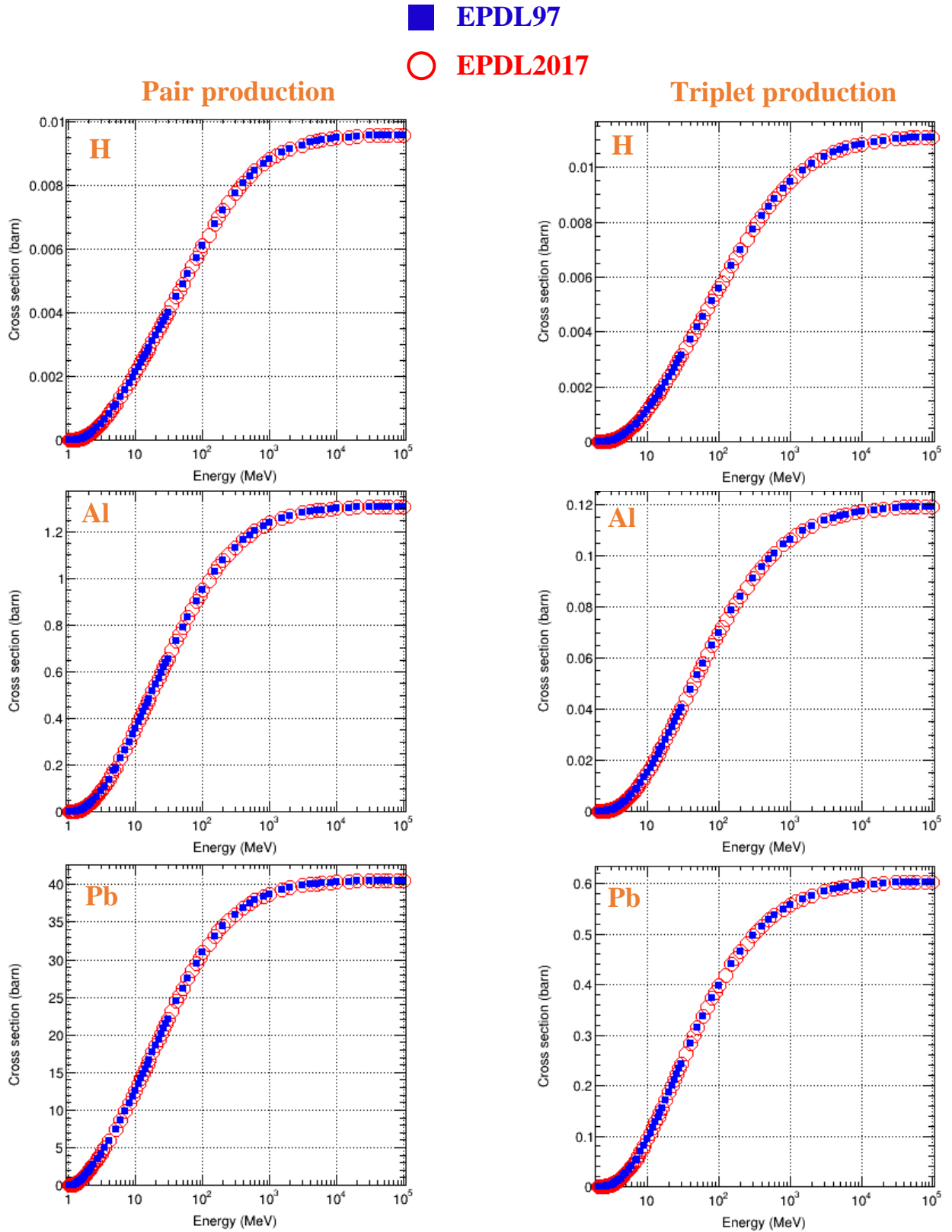


Figure 2 - 5. Cross-sections of gamma conversion as a function of energy, for hydrogen ( $Z = 1$ ), aluminum ( $Z = 13$ ) and lead ( $Z = 82$ ), for pair (left) and triplet (right) production, between EPDL2017 (open circles) and EPDL97 (filled squares).

### 3.1.3. Implementation

For the gamma conversion process, we updated two model classes in the Livermore low-energy sub-package:

- *G4LivermoreGammaConversionModel*;
- *G4LivermoreGammaConversion5DModel*.

They both perform the following tasks:

- Calculate the cross-section according to the energy value of the incident photon and the composition of material;
- Generate the final state (*e.g.*, energy and direction of primary and secondary particles).

The difference between the two models lies in the way of sampling the final state:

- *G4LivermoreGammaConversionModel* is derived from *G4PairProductionRelModel*, and thus inherits its method of sampling the final state, in which the Landau-Pomeranchuk-Migdal effect [5] is taken into account;
- *G4LivermoreGammaConversion5DModel* is a new model class, inheriting a more complex description of the final state, provided by *G4BetheHeitler5DModel*. More precisely, *G4BetheHeitler5DModel* takes into account the recoil target (isolated-charge or atomic) for nuclear or triplet conversion, and also the polarization of the incident photon if required [6]. For this reason, it is more accurate but slower than other alternative models. Users should choose the appropriate model according to their needs.

To calculate the cross-section, these two models read the same cross-section data updated with EPDL2017. These data are the sum of pair production and triplet production cross-sections. They are provided as specific data files included in Geant4. During the initialization phase, Geant4 reads the cross-section files and calculates the cross-sections according the energy of incident photons. As already mentioned, the interpolation in the Geant4 code was modified from logarithmic to linear, corresponding to the interpolation of EPDL2017.

## 3.2. Compton scattering

### 3.2.1. Physical process

The Compton scattering is an inelastic gamma scattering on an atom with the ejection of an electron. It is a prominent process in the MeV range, particularly for low  $Z$  elements. A scattering function ( $SF$ ) is used to describe the angular distribution of the incoherently scattered photon [7, 8]. It is defined as a function of momentum transfer  $q$ , which is expressed as:

$$q = \frac{1}{\lambda} \sin\left(\frac{\theta}{2}\right) \quad (2 - 1)$$

where  $\theta$  is the photon scattering angle and  $\lambda$  is its wavelength.

At low momentum transfers, the scattering function approaches zero and at high momentum transfers, it approaches a constant value, the atomic number  $Z$  of the element.

#### **3.2.2. Description of data**

For Compton scattering, the cross-section data and scattering function data are used in the Livermore model and need to be updated.

##### ***a) Cross section***

For cross-section the only difference compared with EPDL97 is that more points (about three times) are contained in EPDL2017 in order to allow one to use linear interpolation between tabulated points. Figure 2 - 6 shows an example of comparison of cross-sections between EPDL2017 and EPDL97 for H, Al and Pb. It was stated [4] that a good agreement was observed when comparing EPDL2017 with Penelope and XCOM data for all elements ( $Z$ : 1-100). Roughly, a 4% difference for cross-sections was observed in the 100 keV to 1 GeV range. At lower energies, it was shown that EPDL2017 and XCOM data remained in a very good agreement down to 1 keV, whereas the difference with Penelope data increased. However, in this low energy range, Compton scattering made a minor contribution, representing less than 1% of total absorption for low  $Z$  elements, even much less for high  $Z$  elements [4].

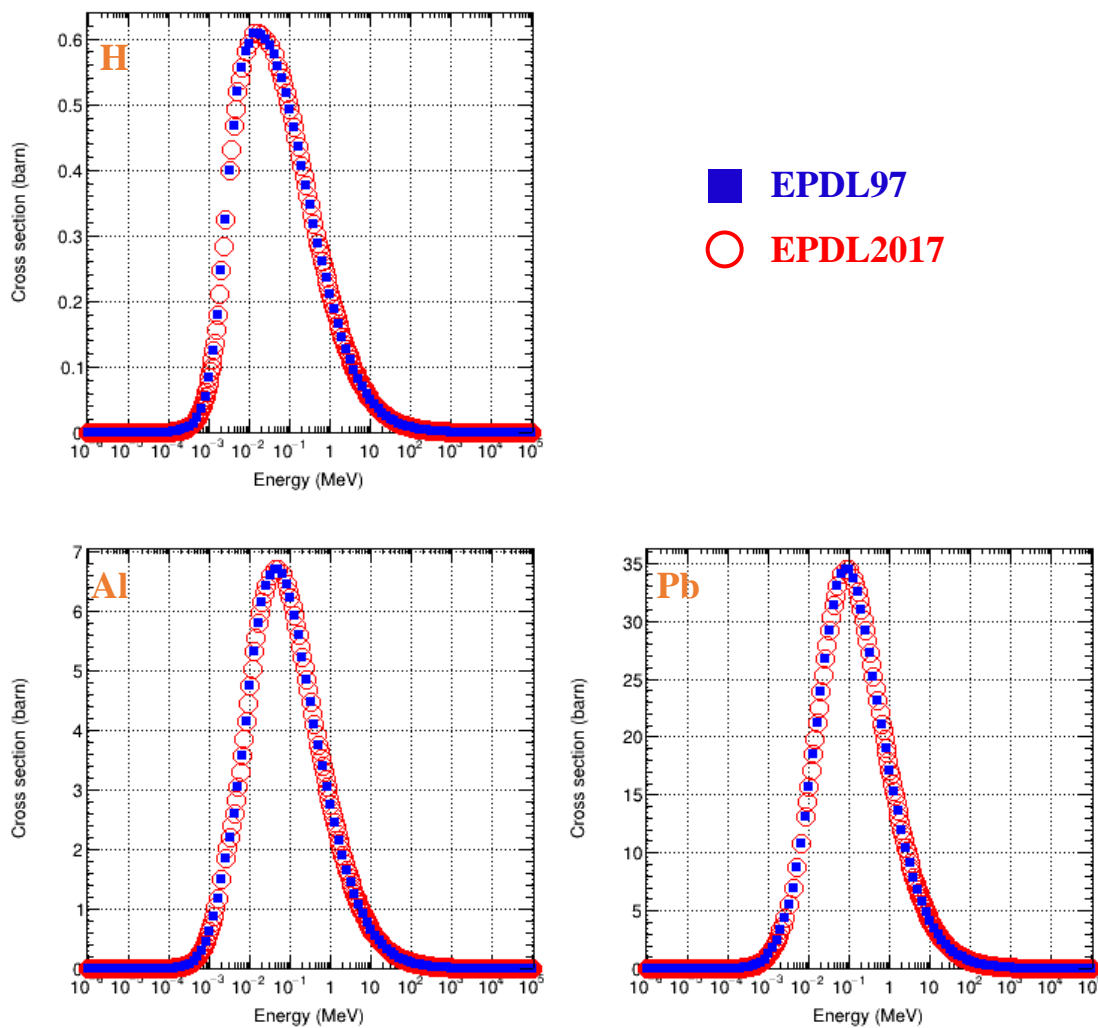


Figure 2 - 6. Compton scattering cross-sections as a function of energy for H, Al and Pb between EPDL2017 and EPDL97.

### **b) Scattering function**

An evident change of scattering function data in EPDL2017 is the unit of the momentum transfer, which is expressed in  $\text{cm}^{-1}$  in EPDL97, while in units of  $10^{16} \text{m}^{-1}$  in EPDL2017. Moreover, EPDL2017 contains more points (about three times) as shown in Figure 2 - 7 for the comparison of scattering functions between EPDL2017 and EPDL97 for H, Al and Pb.

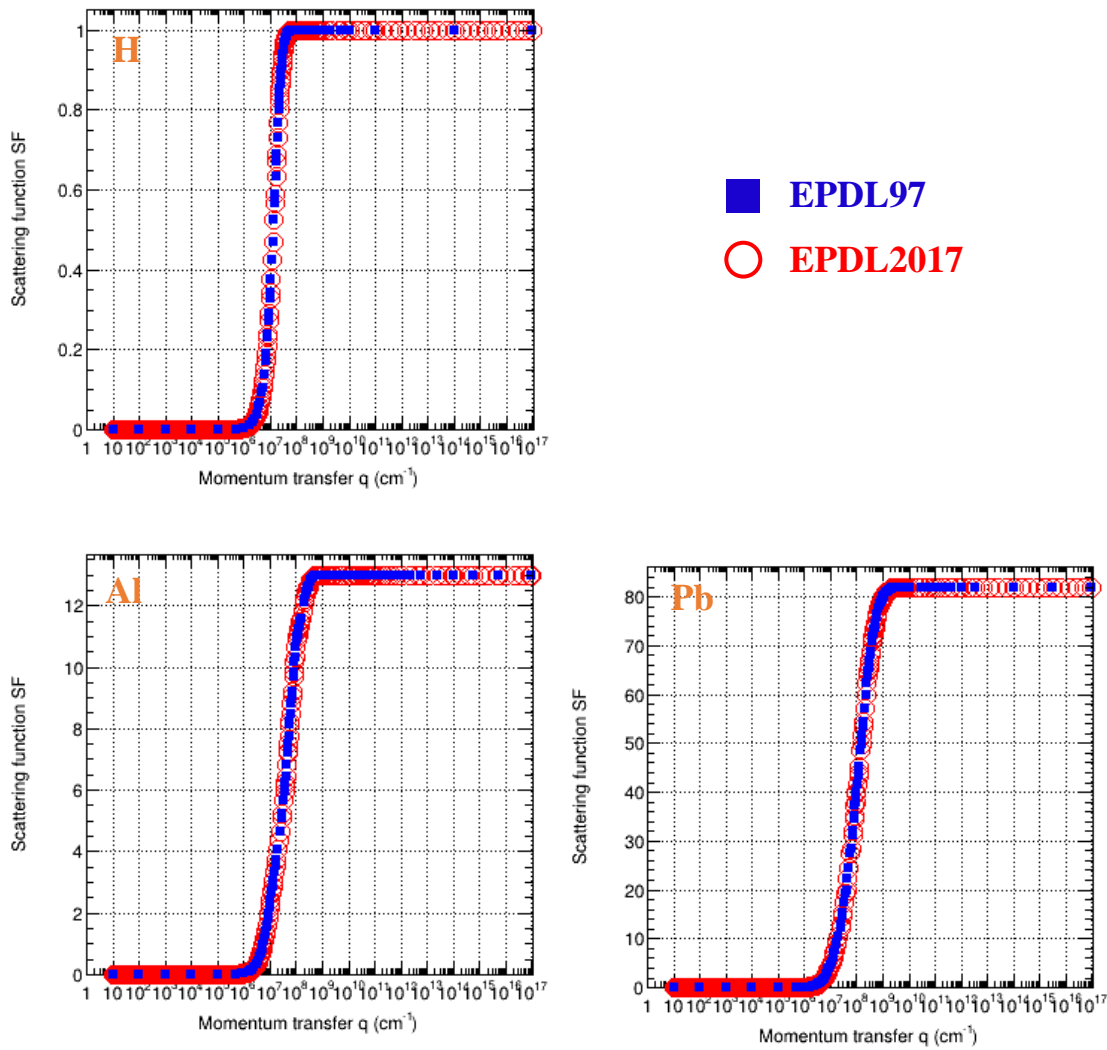


Figure 2 - 7. Scattering functions as a function of momentum transfer of Compton scattering for H, Al and Pb between EPDL2017 and EPDL97.

### 3.2.3. Implementation

Compton scattering is described by the *G4LivermoreComptonModel* class below 1 GeV.

#### a) Cross-section

Similar to the gamma conversion, the cross-section data based on EPDL2017 were updated in form of specific data files, which are read by *G4LivermoreComptonModel*.

#### b) Scattering function

As already mentioned, in Geant4 some data are not directly read as tabulated values, but instead, are calculated via a parameterization, in order to optimize computation. This is the case for scattering functions (SF), which are parameterized on several regions depending on the values of momentum



transfer  $q$ , as shown in Figure 2 - 8. In general, the scattering functions are parametrized in the following way:

- For regions 1 and 2, a polynomial fit is used:

$$\log_{10} SF = \sum_{i=0}^n a_i (\log_{10} q)^i \quad (2 - 2)$$

Where:

- $i$  is the order of each term of the polynomial;
- $n$  is the degree of polynomial;
- $a_i$  is the fitting parameter.
- For region 3:

$$SF = Z \quad (2 - 3)$$

Where  $Z$  is the atomic number of the element.

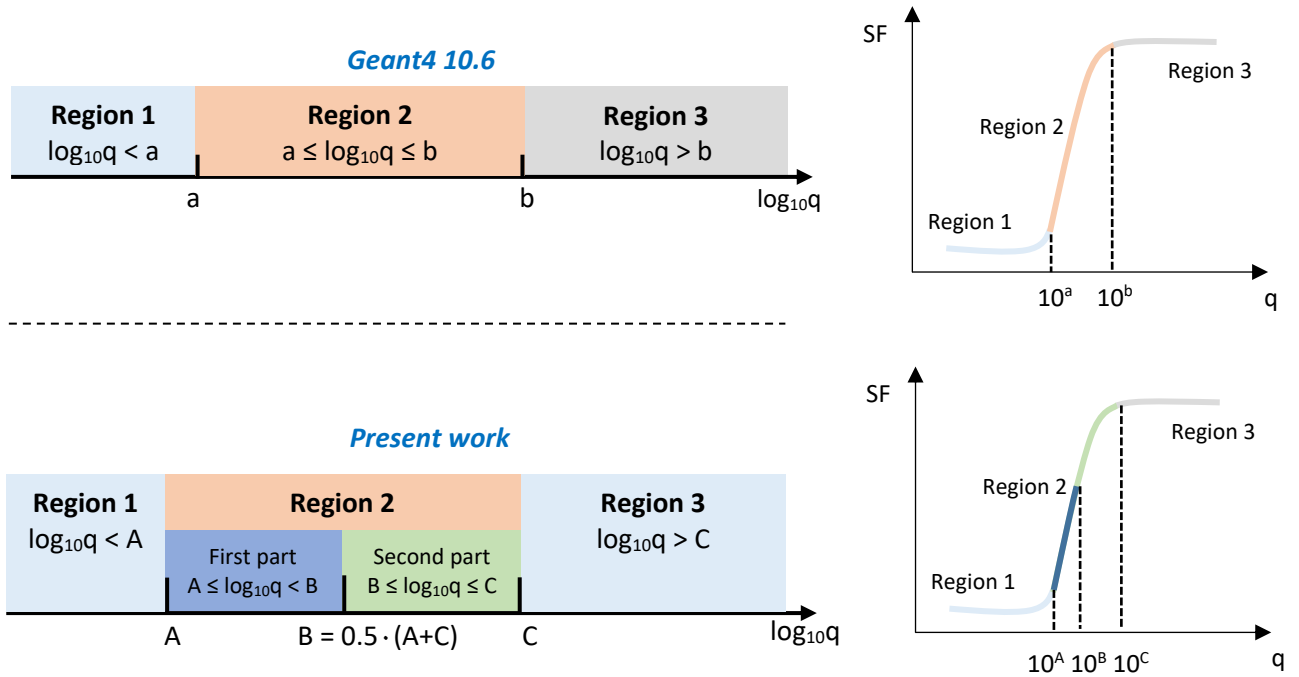


Figure 2 - 8. Regions and sub-regions for the fits of the scattering functions for the Compton effect. The top figure represents the fit regions for Geant4 10.6 based on EPDL97, the bottom for our update based on EPDL2017.

In Geant4 10.6, the degree of polynomial is  $n = 1$  for region 1,  $n = 3$  for region 2. Our aim is to improve the accuracy of these parameterizations. In our implementation, this is achieved in two steps:

- Modification of the regions: we took the same limits for the different regions as Geant4 10.6 and adjusted accordingly;
- Modification of the degree of the polynomial functions when necessary.

For these reasons, region 2 was divided into 2 parts with  $n = 4$  for each sub-region (Figure 2 - 8).

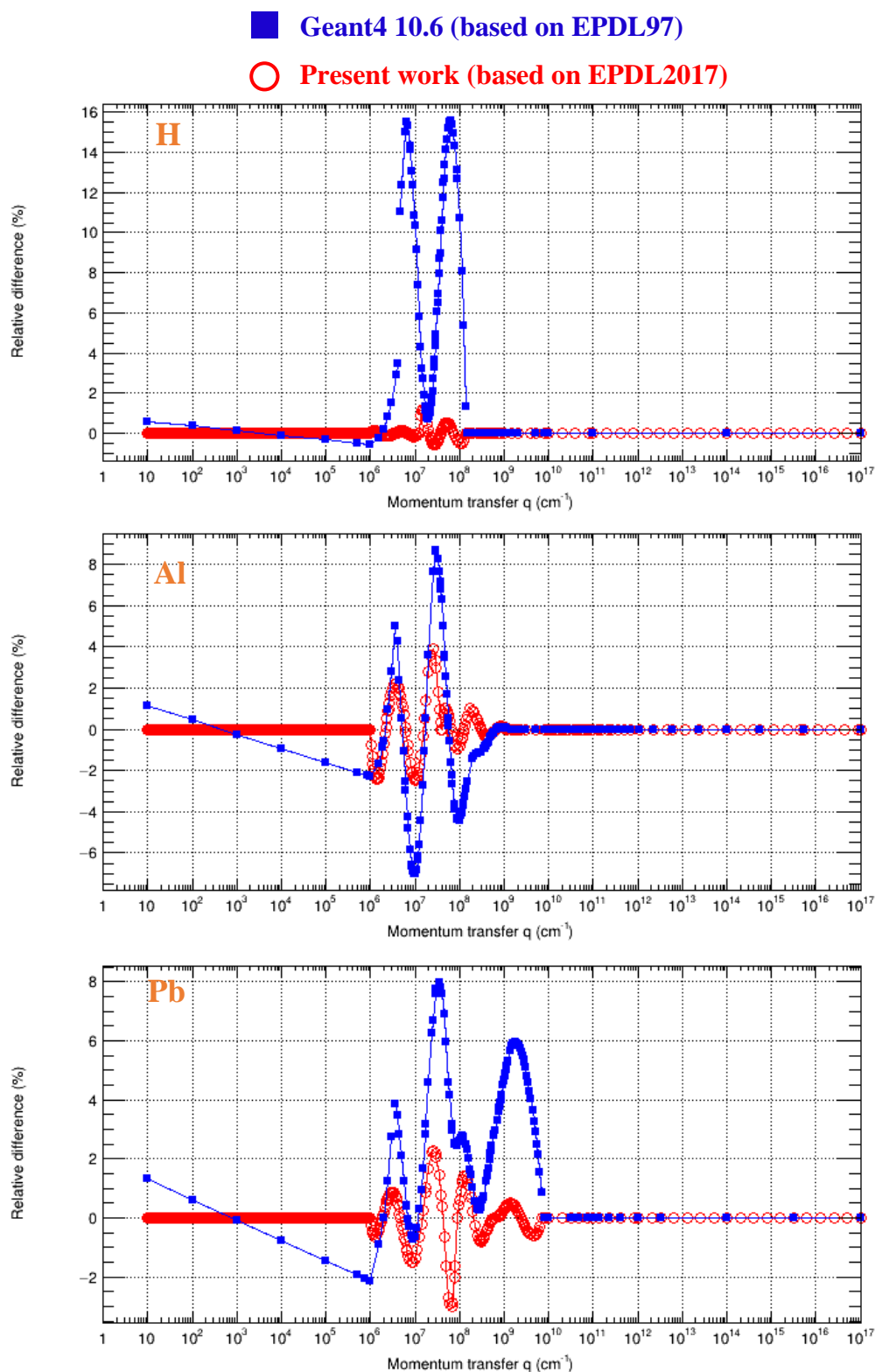


Figure 2 - 9. Relative difference in the fitted scattering function for the Compton effect as a function of momentum transfer, for the present work based on EPDL2017 and Geant4 10.6 based on EPDL97. The relative difference is calculated by equation (2-4). The lines are used only to guide the eye.

Besides, a special attention was paid to avoid discontinuity of relative difference values at the junction of two consecutive regions. The comparisons of fits are given in Figure 2 - 9. The relative difference (*RD*) in percentage of fitted values compared to tabulated data is calculated as follows:

$$RD (\%) = 100 \times \frac{\text{Fitted value} - \text{Tabulated value}}{\text{Tabulated value}} \quad (2 - 4)$$

To assess the accuracy of the parameterization, we compared the maximal relative difference between parameterized and tabulated *SF* as a function of *Z* as shown in Figure 2 - 10. We observed that the maximal relative difference amongst all elements is:

- About 0.0053% (*Z* = 32) in region 1 and 6.5% (*Z* = 38) in region 2 for the present work;
- Approximately -20% (*Z* = 2) and -42% (*Z* = 91) for Geant4 10.6.

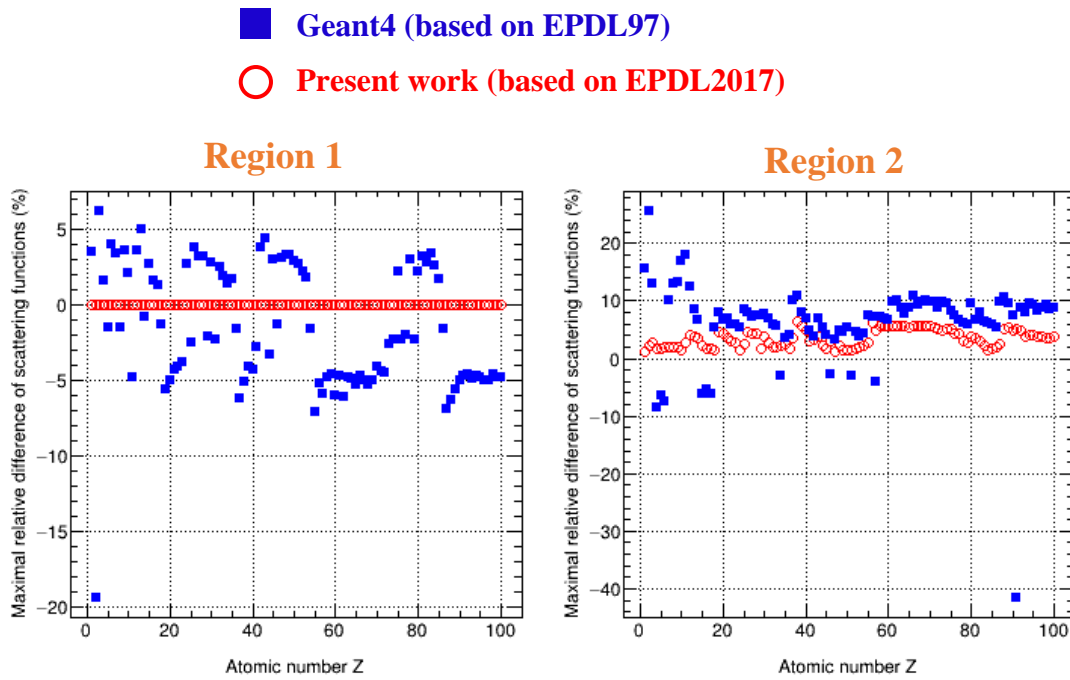


Figure 2 - 10. Maximal relative difference in the fitted scattering function for the Compton effect as a function of atomic number (*Z*: 1-100) in region 1 (left) and region 2 (right), for the present work based on EPDL2017 and Geant4 10.6 based on EPDL97.

However, due to the presence of outliers, it would be misleading if we directly compared these maximal values. For this reason, we tried to estimate an indicative value of the improvement of the precision of the fit (*IP*) on average for both region 1 and region 2. The *IP* is calculated as follows:

$$IP = \frac{1}{100} \sum_{i=1}^{100} \left| \frac{(R_{max})_i}{(r_{max})_i} \right| \quad (2 - 5)$$

Where:

- *i* is the atomic number of elements, *Z*: 1-100;

- $(R_{max})_i$  and  $(r_{max})_i$  are the maximal relative difference in percentage of the  $i$ -th element for Geant4 10.6 and present work respectively. The relative difference is expressed as equation (2-4).

Eventually, we found an  $IP$  about 1000 for region 1 and 2.8 for region 2. We have to point out that an  $IP$  of 1000 for region 1 does not mean that the previous fitting method was bad: In fact, the relative difference using previous fitting method was acceptable for two reasons:

- The maximal relative differences of fitted values compared to tabulated values were not too big, about 5-10% for most elements as shown in Figure 2 - 10;
- The values of the scattering function in region 1, which is a low  $q$  momentum transfer region, are much smaller, as shown in Figure 2 - 7, so the consequence on Geant4 simulation results would be negligible compared to the other fitting regions.

### 3.3. Photoelectric effect

#### 3.3.1. Physical process

The photoelectric effect is the ejection of an electron from an atom after a photon has been absorbed. It is the dominant process at low energy, up to a few hundred keV, for most elements. The electron kinetic energy is the difference between the incident photon energy and the binding energy of the electron. In order to model the ionised subshell, from which the electron is emitted, the cross-sections of each subshell are required in addition to total cross-sections.

#### 3.3.2. Description of data

##### a) Binding energies

One of the main modifications in EPDL2017 concerns the cross-sections, both total and subshells, which require an update. This modification results from a major change regarding the atomic binding energies [4]. These new binding energies result in the shift of the photoelectric edges and consequently lead to a modification of the photoelectric cross-sections. Figure 2 - 11 shows an example of the modification in binding energies for H, Al and Pb between EPDL2017 and EPDL97. The relative difference ( $RD$ ) in percentage for the modified values, *e.g.*, binding energies, is calculated as follows:

$$RD (\%) = \frac{EPDL2017 - EPDL97}{EPDL97} \times 100 \quad (2 - 6)$$

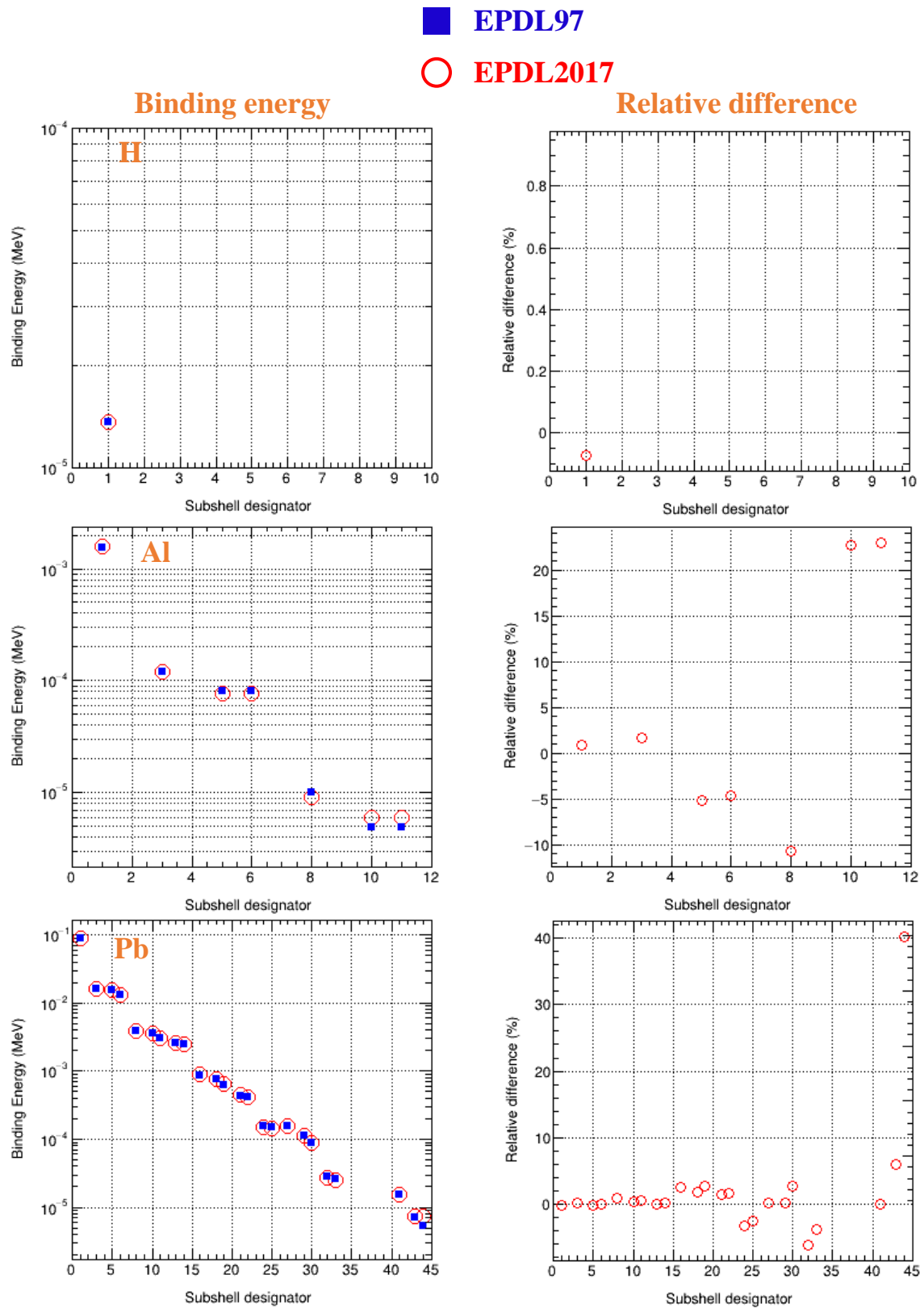


Figure 2 - 11. Binding energies (left) from EPDL2017 and EPDL97 according to subshell designator (Appendix A). Relative difference in binding energies of EPDL2017 (right) compared to EPDL97 (equation (2-6)).

We observed large relative differences in binding energies for outer subshells. However, these large differences do not have great impact, since the binding energies of the outer subshells are small, within a few eV. The maximal relative difference in binding energies was plotted as a function of  $Z$  for all elements (Figure 2 - 12). Large variations were observed, up to 71%, for  $Z = 71$ , due to the outer subshells. In order to compare the data in a more representative way, we also plotted the mean absolute relative difference ( $MD$ ) as a function of  $Z$  (Figure 2 - 12), calculated as follows:

$$MD = \frac{1}{n} \sum_{i=0}^{n-1} |r_i| \quad (2-7)$$

Where:

- $n$  is the number of subshells of an element;
- $r_i$  is the relative difference of the binding energy of the  $i$ -th subshell. The relative difference is expressed as equation (2-6).

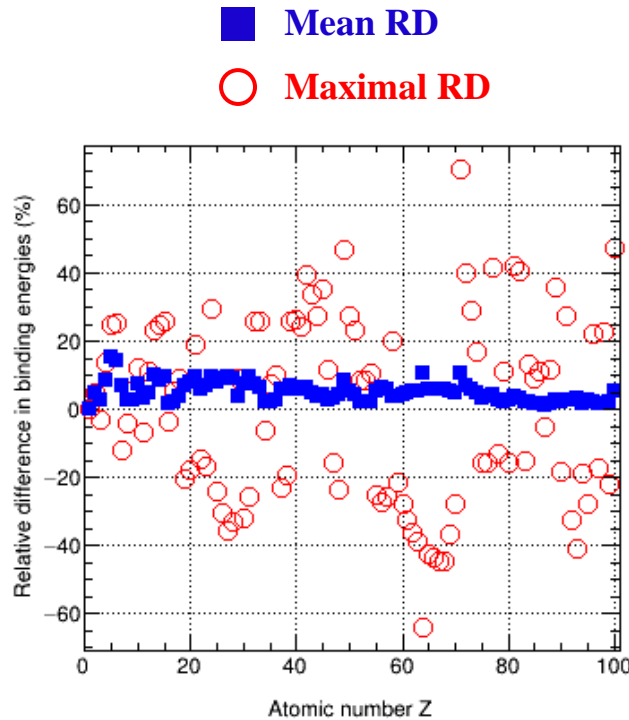


Figure 2 - 12. Maximal relative difference and mean absolute relative difference value in binding energies of EPDL2017 compared to EPDL97 as a function of atomic number ( $Z$ : 1-100). The maximal relative difference and mean absolute relative difference are calculated by equation (2-6) and (2-7) respectively.

### **b) Total cross-section**

The total cross-sections in EPDL2017 were adapted near the photoelectric edges, in order to adjust to the modifications of binding energies. It was stated [4] that the cross-section values were modified only within the edge regions, in order to keep the good agreement that had been already observed for EPDL97

with experimental data. The shifts were largest for high Z elements. It was concluded that EPDL2017 is in agreement with the XCOM and Scofield [9] data sets. However, when comparing to Penelope, a larger difference was observed at high energy, above a few hundred keV; the difference even reached 15 % for some elements, whereas it was 1-2% when compared to XCOM and Scofield [4]. An example of total cross-sections for H, Al and Pb between EPDL2017 and EPDL97 is displayed in Figure 2 - 13. Higher RD was observed at some specific energies due to the modification of binding energies. For instance, for Al, RD is larger than 700% at  $8.035 \times 10^{-5}$  MeV, which is near the binding energy of the L3 subshell, *i.e.*,  $8.073 \times 10^{-5}$  MeV for EPDL97 and  $7.700 \times 10^{-5}$  MeV for EPDL2017.

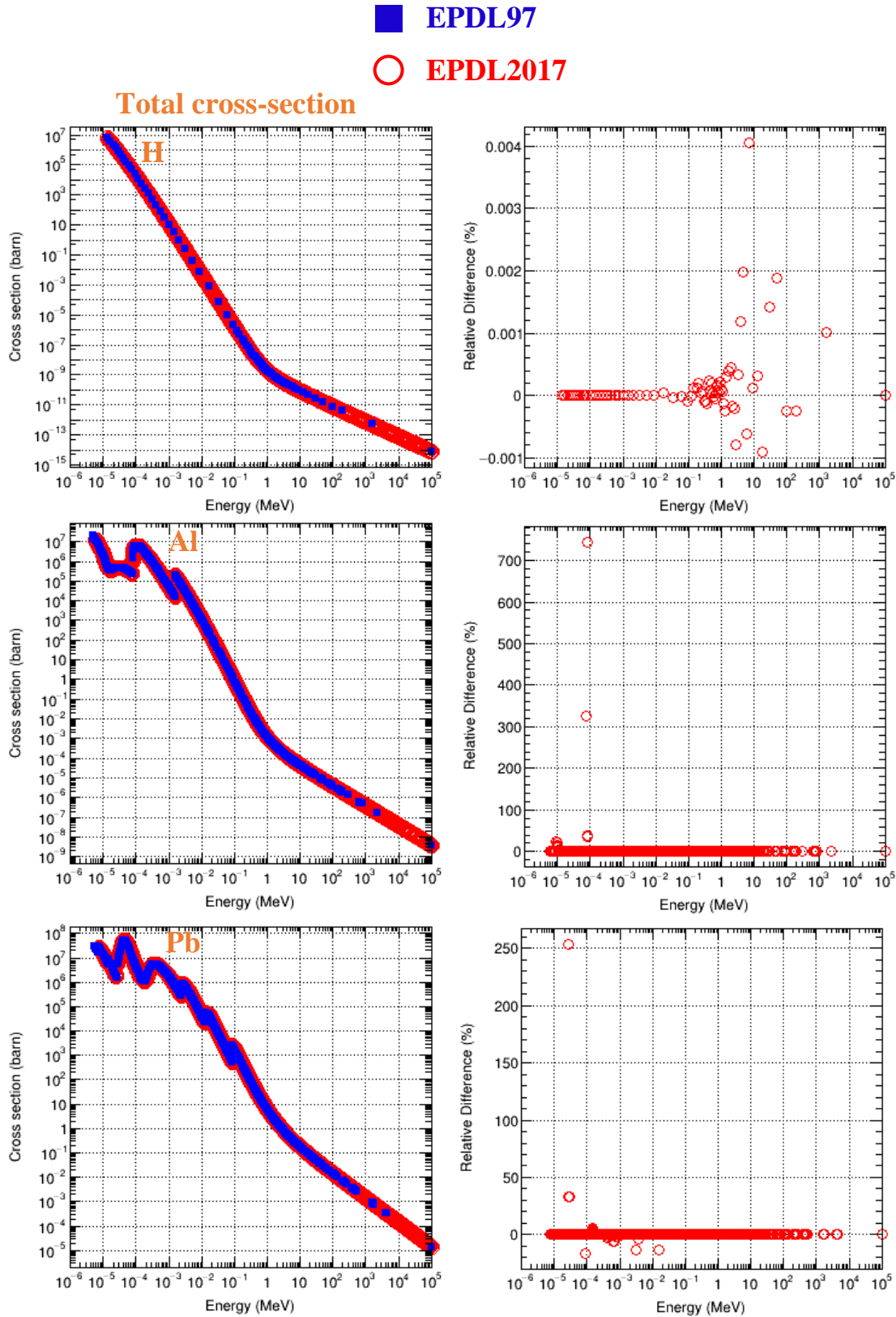


Figure 2 - 13. Total cross-sections (left) of the photoelectric effect as a function of energy for H, Al and Pb between EPDL2017 and EPDL97. Relative difference of EPDL2017 (right) compared to EPDL97 (equation (2-6)).



### 3.3.3. Implementation

#### a) Principle of the parameterization

The photoelectric effect is described by *G4LivermorePhotoElectricModel*. In Geant4 10.6, the cross-section is either described by a parameterization or directly tabulated, depending on the energy of the incident photon  $E$ . More precisely, the subshell cross-section is tabulated when energy is lower than a threshold, *i.e.*, the low energy limit  $E_a$ , as indicated in Figure 2 - 14. Above the threshold (low energy limit), the cross-section is parameterized.

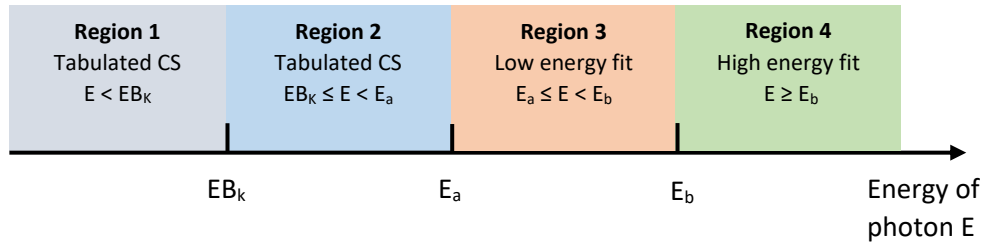


Figure 2 - 14. Regions for the calculation of cross-sections of the photoelectric effect:  $EB_K$  is the binding energy of the K-shell;  $E_a$  is the low energy limit;  $E_b$  is the high energy limit.

The parameterization is performed on the subshell cross-sections in two different energy intervals (“low energy fit” and “high energy fit”) (Figure 2 - 14), as follows:

$$\sigma_i(E) = \sum_{j=1}^6 \frac{a_{ij}}{E^j} \quad (2 - 8)$$

Where:

- $E$  is the energy of photon;
- $a_{ij}$  is the fitting parameter corresponding to the  $i$ -th subshell
- $j$ -th is the degree of the term of the polynomial.

Thus, the total cross-sections are obtained by the following equation:

$$\sigma_{tot}(E) = \sum_{i=0}^{n-1} \sigma_i(E) = \sum_{i=0}^{n-1} \sum_{j=1}^6 \frac{a_{ij}}{E^j} \quad (2 - 9)$$

Where  $n$  is the number of subshells.

#### b) Subshell cross-section

For our update with EPDL2017, we followed the same method of parameterization, but the fitting parameters  $a_{ij}$ , the thresholds and energy intervals were adjusted accordingly. Fitted K shell cross-sections of H, Al and Pb, using new fitting parameters, compared with tabulated values, are given in Figure 2 - 15 . The relative difference in percentage is calculated in the same way, following equation (2-4).

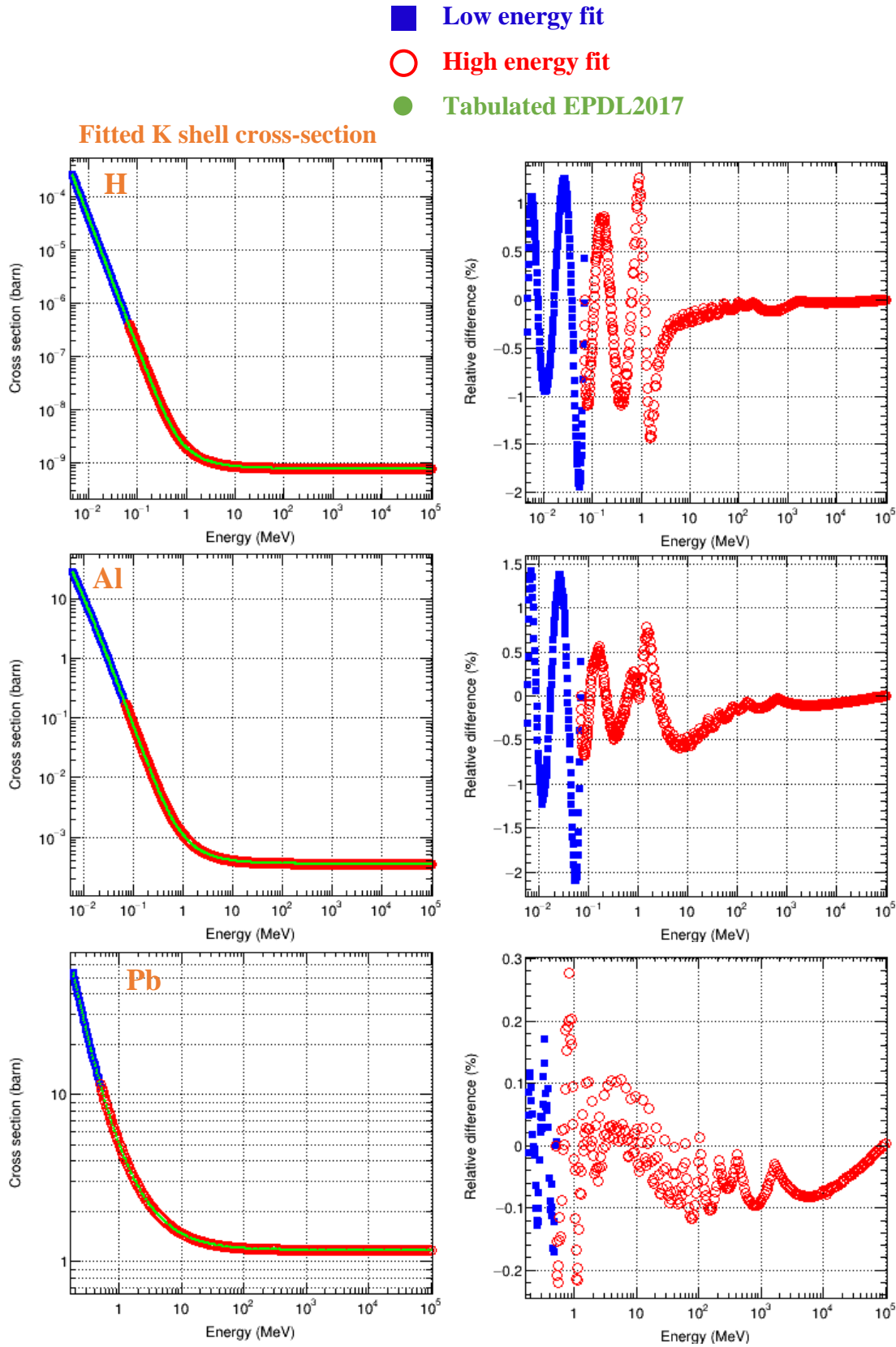


Figure 2 - 15. Fitted K shell cross-sections of the photoelectric effect (left) as a function of energy for H, Al and Pb using new fitting parameters, based on EPDL2017. Relative difference (right) compared to tabulated values (equation (2-4)).

In order to evaluate the performance of our new fits, we plotted the maximal relative difference amongst all the subshells, as a function of  $Z$ , in Figure 2 - 16.

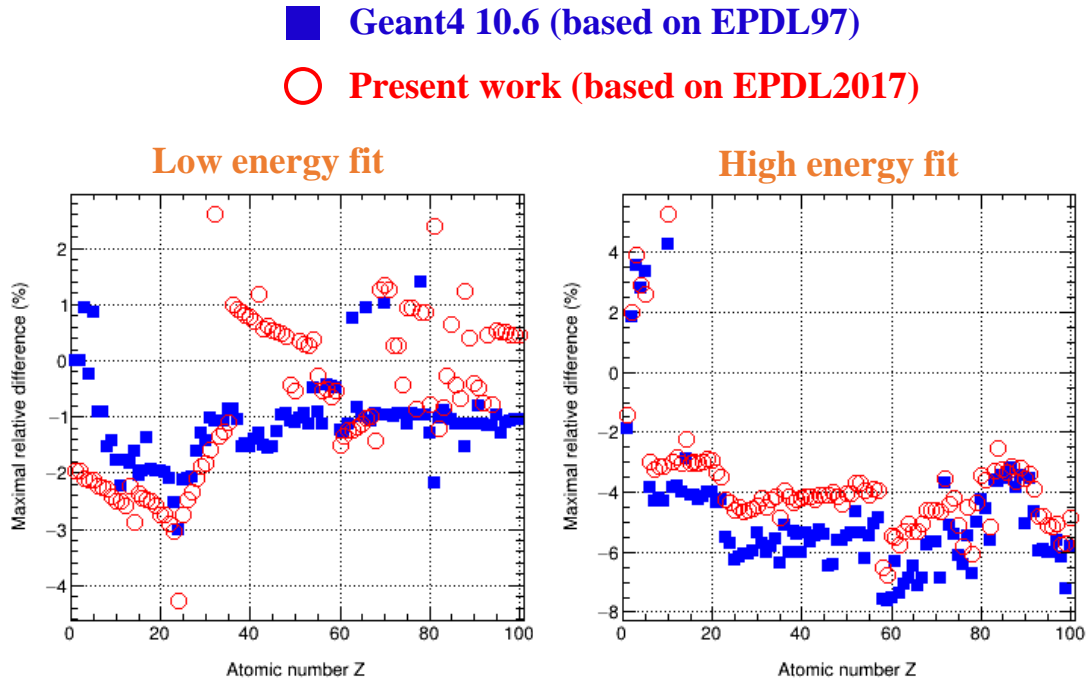


Figure 2 - 16. Maximal relative difference in low energy fit (left) and high energy fit (right) of subshell cross-sections of the photoelectric effect, as a function of atomic number ( $Z$ : 1-100), for the present work based on EPDL2017 and Geant4 10.6 based on EPDL97.

The relative difference is calculated by equation (2-4).

The values of maximal relative difference are of the same order of magnitude for the “low energy fit” and are slightly improved for the “high energy fit”. The highest values occur with the high energy fit for element  $Z = 59$ : -6.7% for the present work, compared to -7.6% for Geant4 10.6. These high values especially occur for the outer subshells. For this reason, and following a similar approach as in section 3.3.2, we calculated the mean absolute relative difference value ( $MD$ ) as a function of  $Z$  in order to show the quality of the fits from an overall perspective (Figure 2 - 17), according to the following formula:

$$MD = \frac{1}{nm} \sum_{i=0}^{n-1} \sum_{j=1}^m |r_{ij}| \quad (2 - 10)$$

Where:

- $n$  is the number of subshells;
- $m$  is the number of energy points;
- $r_{ij}$  is the relative difference at the  $j$ -th energy point of  $i$ -th subshell. The relative difference is expressed as equation (2-4).

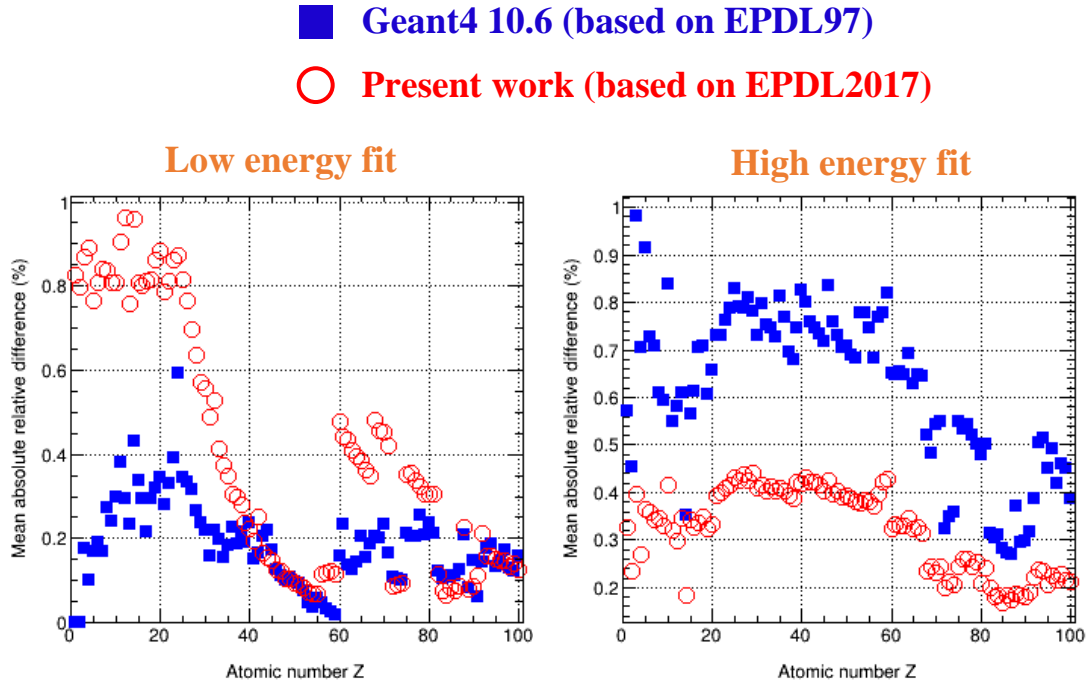


Figure 2 - 17. Mean absolute relative difference for the low energy fit (left) and the high energy fit (right) of subshell cross-sections of the photoelectric effect, as a function of atomic number ( $Z$ : 1-100), for the present work based on EPDL2017 and Geant4 10.6 based on EPDL97. The mean absolute relative difference is calculated by equation (2-10).

The highest values of  $MD$  for subshell cross-sections are up to 0.96% for element  $Z = 12$  (low energy fit) for the present work, compared to 0.98% for element  $Z = 3$  (high energy fit) for Geant4 10.6. From a technical point of view, it is difficult to make both fits without having to make a compromise. Especially, particular attention was paid to avoid cross-section jumps at the border between the low and high energy fits.

### **c) Total cross-section**

Finally, for total cross-sections, the maximal relative difference as a function of  $Z$  is displayed in Figure 2 - 18. The highest values of maximal relative difference are up to 4.2% for element  $Z = 10$  (high energy fit) for the present work, compared to 4.4% for element  $Z = 93$  (low energy fit) for Geant4 10.6. Based on these maximal relative differences, we tried to estimate an indicative value of the improvement of the precision of the fit ( $IP$ ) on average for both low and high energy fits, following equation (2-5). We obtained an  $IP$  of about 1.9 for the low energy fit and 1.3 for the high energy fit.

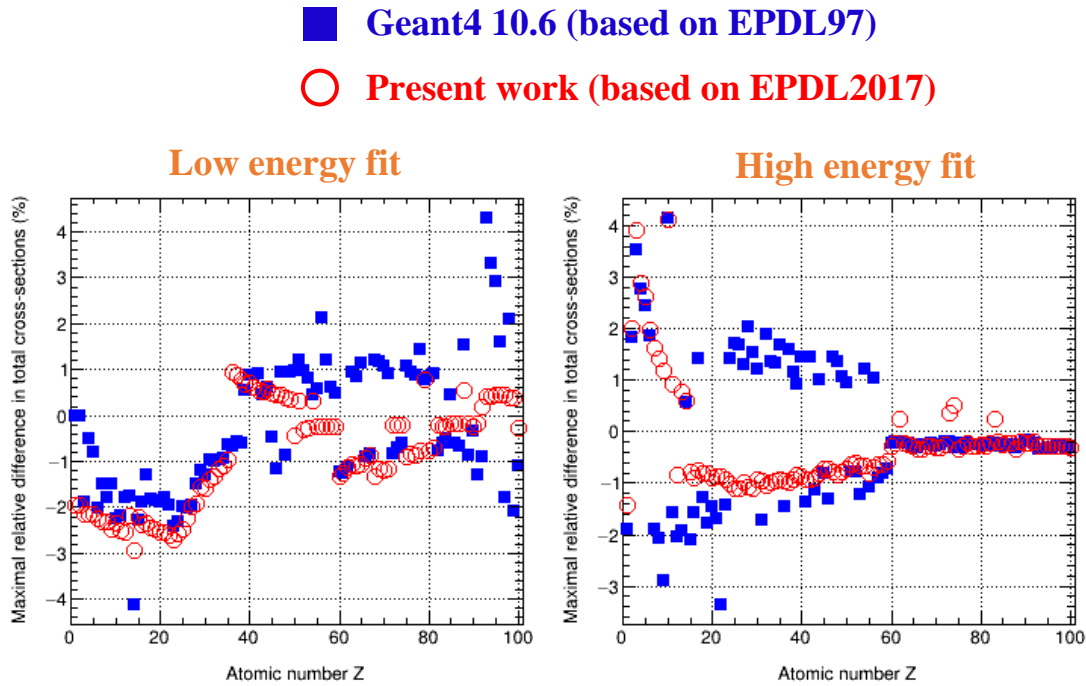


Figure 2 - 18. Maximal relative difference in total cross-sections of the photoelectric effect as a function of atomic number ( $Z$ : 1-100) for low (left) and high energy fit (right), for the present work based on EPDL2017 and Geant4 10.6 based on EPDL97.

The relative difference is calculated by equation (2-4).

## 3.4. Rayleigh scattering

### 3.4.1. Physical process

Rayleigh scattering is an elastic scattering of a photon off atomic electrons without change in its wavelength. In general, this process plays a significant role in the low energy range. The change in photon direction is described for each element using a form factor ( $FF$ ) that gives the angular distribution of the scattered photon [8, 10]. The form factor is a function of the momentum transfer  $q$ , which, as for Compton scattering, is defined in the same way as equation (2-1). At high momentum transfer, the form factor approaches zero and at low momentum transfer it approaches a constant value, which is the atomic number  $Z$  of the element.

### 3.4.2. Description of data

#### a) Cross-section

Rayleigh scattering cross-sections constitute another major change in EPDL2017. This is also due to the modification of binding energies already mentioned for the photoelectric effect. However, modifications for the cross-sections of the photoelectric effect were restricted to the vicinity of edges, whereas a complete update has been performed for the cross-sections of Rayleigh scattering. For this reason, it

should be noted that, unlike the data for other processes, the number of tabulated points for Rayleigh scattering cross-sections in EPDL2017 is lower than that in EPDL97 (Figure 2 - 19). Batic *et al.* [11] compared available experimental Rayleigh scattering cross-sections with EPDL97 for several elements; obvious discrepancies were observed, especially for  $Z = 18$ . Based on this, we compared Rayleigh scattering cross-section of EPDL2017 with some of the experimental data [11] for  $Z = 18$ , which showed that EPDL2017 values are much closer to experimental measurements than EPDL97. This comparison is detailed in the technical note<sup>1</sup> that describes the update of EPICS2017 for Rayleigh scattering process. It would be out of the scope of this work to make a review of the existing experimental data. However, it would be interesting in future studies to make a more systematic and precise comparison.

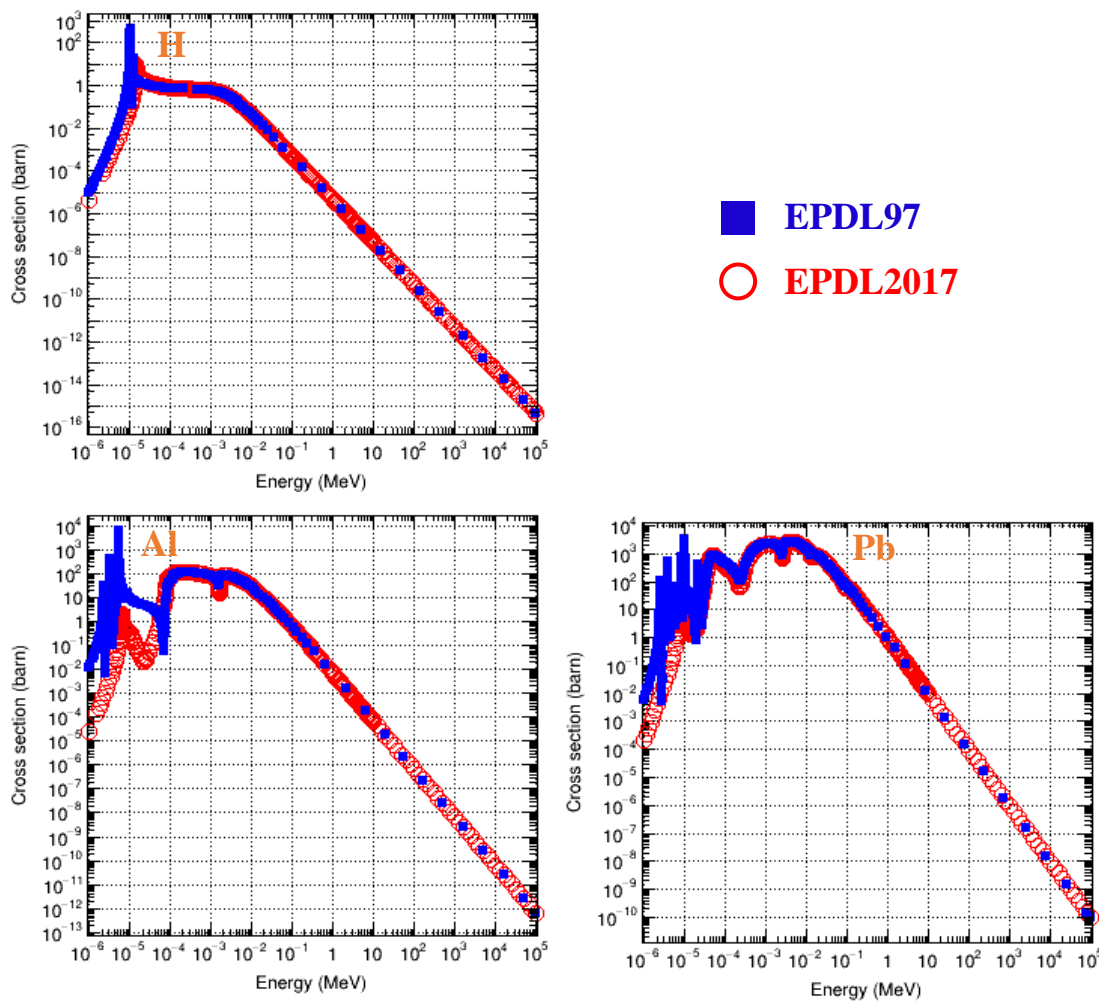


Figure 2 - 19. Rayleigh scattering cross-section as a function of energy for H, Al and Pb, between EPDL2017 and EPDL97.

<sup>1</sup> The technical note for Rayleigh scattering is available in the Geant4@IN2P3 website of *Documentation* section, via <http://geant4.in2p3.fr/styled-4/styled-8/>.

***b) Form factor***

Considering form factors, the only difference between EPDL2017 and EPDL97 occurs in the increase of tabulated points, as shown in Figure 2 - 20 for H, Al and Pb.

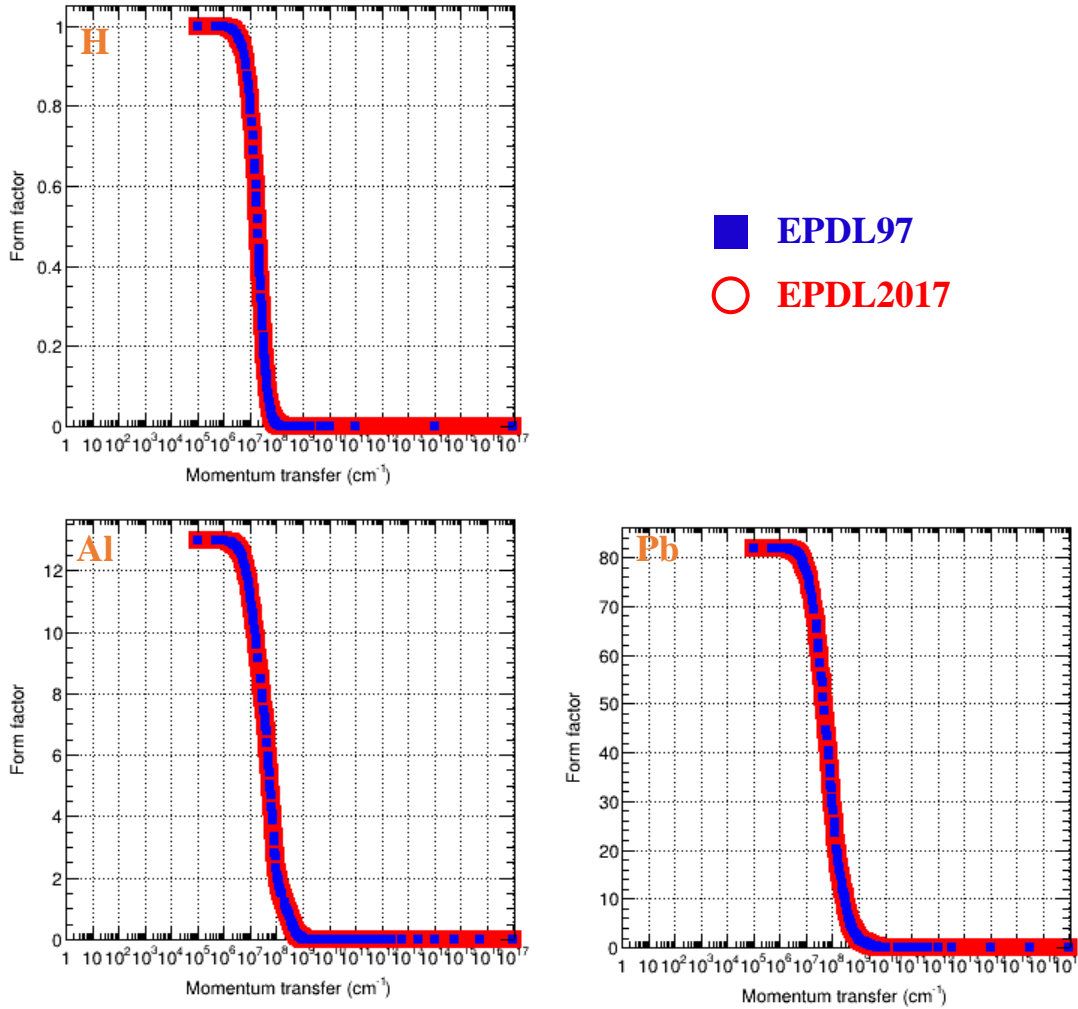


Figure 2 - 20. Rayleigh scattering form factor as a function of momentum transfer for H, Al and Pb between EPDL2017 and EPDL97.

**3.4.3. Implementation**

Rayleigh scattering is described by *G4LivermoreRayleighModel*.

***a) Cross-section***

The cross-section data based on EPDL2017 were updated in form of specific data files, which are read by *G4LivermoreRayleighModel*.

**b) Form factor**

In Geant4 10.6, the form factor  $FF$  is used for the calculation of the final state of the scattered photon after interaction. It is parameterized as a function of the momentum transfer  $q$ , as follows [8]:

$$FF^2(q) = \sum_{i=0}^2 \frac{a_i}{(1 + b_i q^2)^{N_i}} \quad (2 - 11)$$

Where  $a_i$ ,  $b_i$ ,  $N_i$  are fitting parameters.

New fitting parameters were updated based on EPDL2017 with respect to the same fitting function, to take into account the increase of data points. The fit was only performed at low  $q$  only when the  $FF$  is high enough, more precisely in the region where:  $FF^2 \geq 10^{-6} \cdot Z^2$ . Moreover, as  $FF$  quickly decreases down to zero at high momentum  $q$  region, the precision of fit was optimized so that the relative difference between fitted and tabulated data is smaller in the low  $q$  region (high  $FF$  values) than in the high  $q$  region. The relative difference ( $RD$ ) in percentage between fitted and tabulated  $FF^2$  is calculated as follows:

$$RD (\%) = 100 \times \frac{Fitted\ FF^2 - Tabulated\ FF^2}{Tabulated\ FF^2} \quad (2 - 12)$$

Figure 2 - 21 shows the relative difference of the fits for H, Al and Pb.



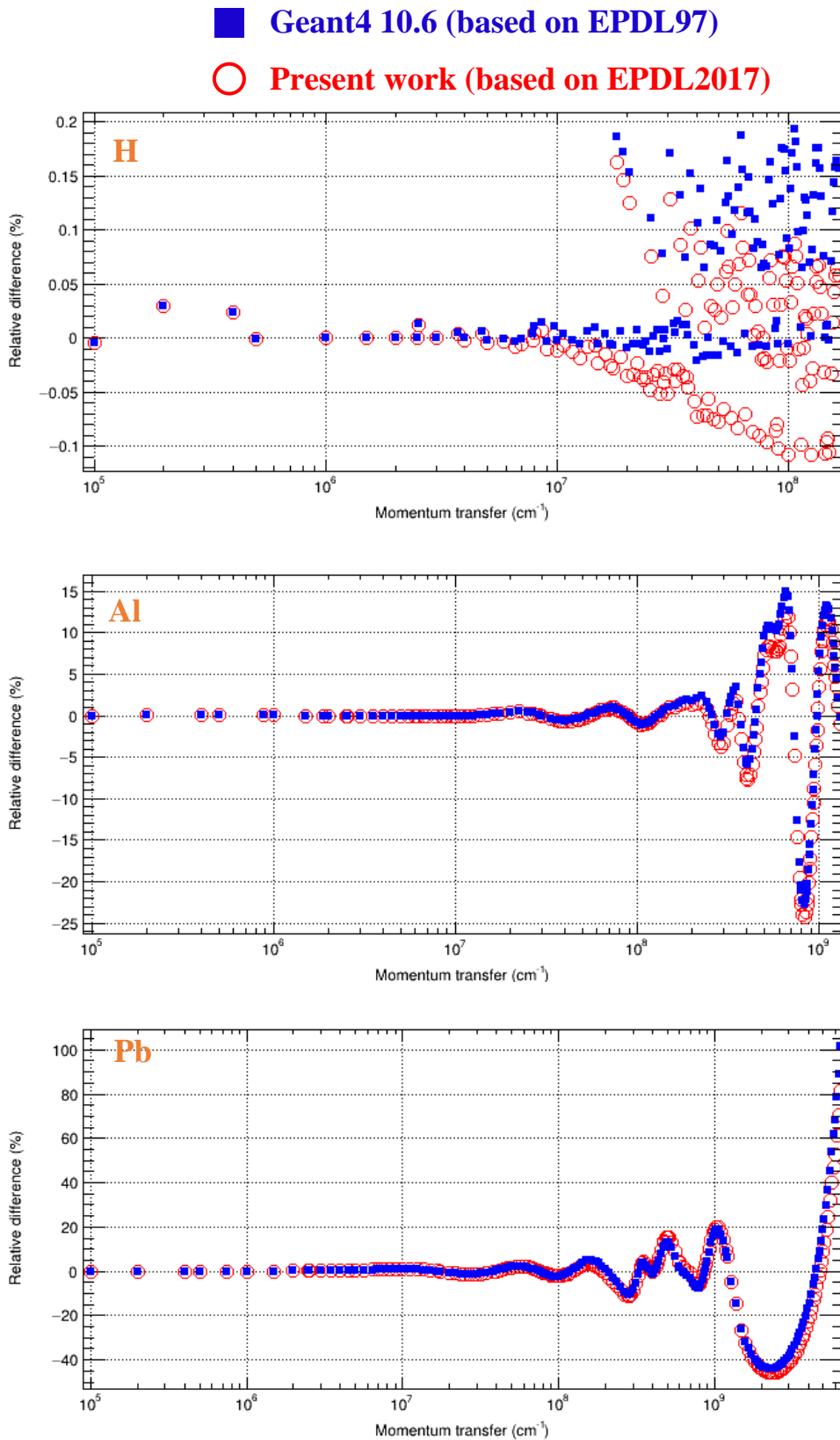


Figure 2 - 21. Relative difference in fitted square of form factors ( $FF^2$ ) of Rayleigh scattering as a function of momentum transfer, for the present work based on EPDL2017 and Geant4 10.6 based on EPDL97. The relative difference is calculated by equation (2-12).

It is conspicuous in these examples that the maximal relative difference between fitted and tabulated  $FF^2$  values varies depending on  $q$ : as already explained, the relative difference is much larger at high  $q$ , which actually has little impact because it corresponds to low  $FF^2$  values. For this reason, the maximal difference obtained for each element is not representative. Thus, we calculated the mean absolute relative difference value ( $MD$ ) for each element (Figure 2 - 22):

$$MD = \frac{1}{m} \sum_{j=1}^m |r_j| \quad (2 - 13)$$

Where:

- $m$  is the number of fitted points;
- $r_j$  is the relative difference at the  $j$ -th point. The relative difference is expressed as equation (2-12).

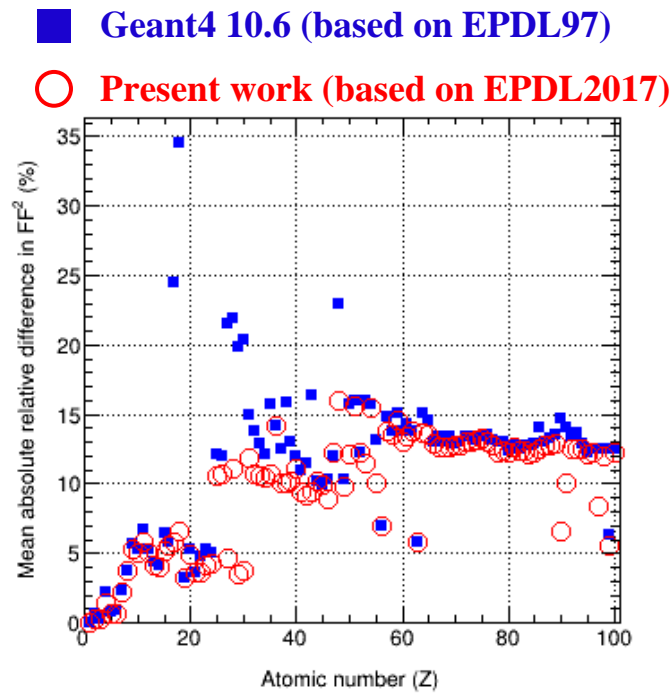


Figure 2 - 22. Mean absolute relative difference in fitted square of form factors ( $FF^2$ ) of Rayleigh scattering compared to tabulated data as a function of atomic number ( $Z$ : 1-100), for the present work based on EPDL2017 and Geant4 10.6 based on EPDL97.

The relative difference is calculated by equation (2-12).

We observed a slight improvement in the accuracy of the parameterization. The maximal value is about 16% ( $Z = 48$ ) for the present work, whereas 35% ( $Z = 18$ ) for Geant4 10.6. We also estimated an indicative value of the improvement of the precision of the fit ( $IP$ ) on average:

$$IP = \frac{1}{100} \sum_{i=1}^{100} \left| \frac{MD_i}{md_i} \right| \quad (2 - 14)$$

Where:

- $i$  is the atomic number of elements,  $Z$ : 1-100;
- $MD_i$  and  $md_i$  are the mean absolute relative difference in percentage of the  $i$ -th element for Geant4 10.6 and the present work respectively, calculated using equation (2-13).

We obtained an  $IP$  about 1.3, indicating a slight improvement regarding the parameterization.

## 4. Comparative study of Geant4 photon models with respect to the XCOM data library

### 4.1. Method

The comparative study described in this section concerns the comparison of the mass attenuation coefficient for selected elements and compounds with respect to the XCOM database from National Institute of Standards and Technology (NIST) (<https://www.nist.gov/pml/xcom-photon-cross-sections-database>). To sample a broad spectrum of materials, we selected the following elements and materials:

- Beryllium, carbon, aluminum, silicon, germanium, iron, silver, cesium, gold, lead, uranium;
- Water and ICRU compact bone [12].

We followed the procedure described by Amako *et al.* [13], which was also used by the G4-Med benchmarking system for medical physics [14]. We considered a monoenergetic photon beam (point source) with a number of incident photons  $N_0$ . The beam passed through a homogeneous slab, with a given thickness, density and composition, made of one of the selected elements or materials above. We took 50 energy values varying from 1 keV to 100 GeV. The choice of the tested energies corresponds to the available data provided by XCOM. In this study, we aimed to compare the mass attenuation coefficient for both total photon interaction  $\mu_m$  and each process  $(\mu_m)_p$  using the Livermore models in Geant4 10.6 (based on EPDL97) and the updated Livermore models in the present work.

The total mass attenuation coefficient  $\mu_m$  is calculated as follows:

$$\mu_m = \frac{1}{\rho d} \ln\left(\frac{N_0}{N}\right) \quad (2 - 15)$$

where:

- $\rho$  is the density ( $\text{g/cm}^3$ ) of the slab;
- $d$  is the thickness of the slab;
- $N_0$  is the number of incident photons;
- $N$  is the number of photons traversing the slab without interacting, *i.e.*, without any change in direction.  $N$  is obtained from the Geant4 simulation results.

The partial mass attenuation coefficient  $(\mu_m)_p$  is calculated using the following equation:

$$(\mu_m)_p = \frac{(\mu_l)_p}{\rho} \quad (2 - 16)$$

where  $(\mu_l)_p$  is the linear attenuation coefficient for a single process  $p$ . The value of  $(\mu_l)_p$  is obtained by the Geant4 inner method `ComputeCrossSectionPerVolume()`.

### 4.2. Simulation uncertainty

The total mass attenuation coefficient  $\mu_m$  is given by equation (2-15):

$$\mu_m = \frac{1}{\rho d} \ln \left( \frac{N_0}{N} \right)$$

so the statistical uncertainty  $\sigma_{\mu_m}$  due to simulation is expressed as:

$$\sigma_{\mu_m} = \sqrt{\left( \frac{d\mu_m}{dN} \right)^2 \sigma_N^2}$$

with  $\sigma_N$ , the uncertainty on the number of detected photons  $N$ :

$$\sigma_N = \sqrt{N}$$

Considering equation (2-15):

$$\frac{d\mu_m}{dN} = -\frac{1}{\rho d N}$$

Thus:

$$\begin{aligned} \sigma_{\mu_m} &= \sqrt{\left( \frac{1}{\rho d} \right)^2 \left( \frac{\sigma_N^2}{N^2} \right)} \\ \Leftrightarrow \sigma_{\mu_m} &= \sqrt{\left( \frac{1}{\rho d} \right)^2 \frac{1}{N}} \end{aligned} \quad (2-17)$$

Finally, the relative uncertainty  $\frac{\sigma_{\mu_m}}{\mu_m}$  is obtained as follows:

$$\frac{\sigma_{\mu_m}}{\mu_m} = \frac{\sqrt{\left( \frac{1}{\rho d} \right)^2 \frac{1}{N}}}{-\frac{1}{\rho d} \ln \left( \frac{N}{N_0} \right)} = \frac{1}{\ln \left( \frac{N_0}{N} \right)} \sqrt{\frac{1}{N}} \quad (2-18)$$

In order to minimize the statistical uncertainty, we chose to use a higher number of incident photons ( $10^6$  photons) compared to the previous study, performed by Amako *et al.* [13] ( $10^4$  photons). Moreover, the thickness  $d$  of the slab was adjusted so as to have a sufficient number of photons  $N$ , which did not interact with the slab. In this way, we ensured that the relative uncertainty on the attenuation coefficient  $\frac{\sigma_{\mu_m}}{\mu_m}$  was always less than 0.3%.

### 4.3. Results

The mass attenuation coefficients for total and each process were calculated with Geant4 simulations for water (Figure 2 - 23) and for all the other selected materials<sup>2</sup>. The relative difference (*RD*) in percentage was also calculated with respect to XCOM using the following equation:

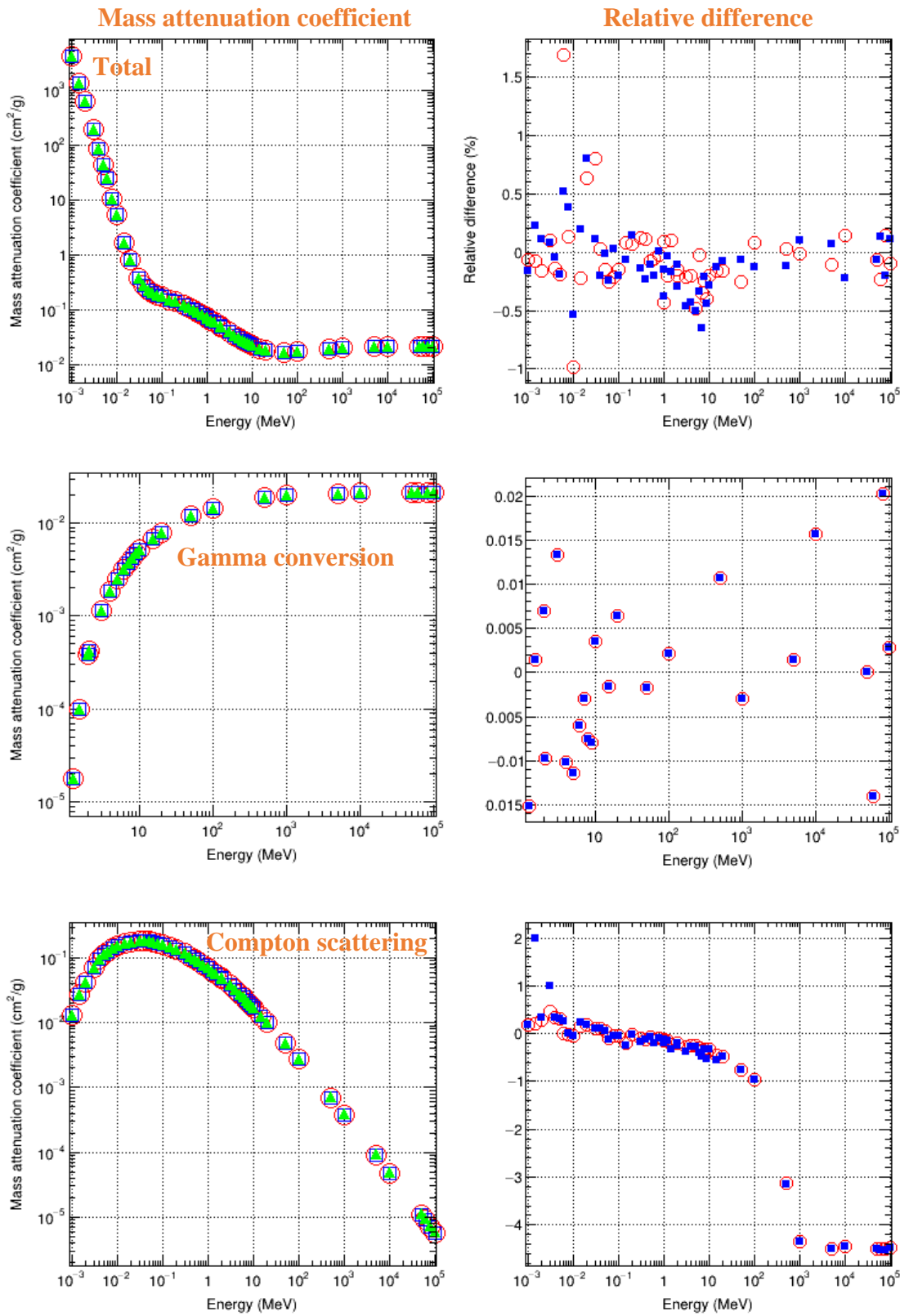
$$RD (\%) = \frac{Simulation - XCOM}{XCOM} \times 100 \quad (2 - 19)$$

Moreover, the maximal relative difference for all the selected materials is shown as a function of *Z* in Figure 2 - 24.

---

<sup>2</sup> The figures for other selected materials are available in the Geant4@IN2P3 website of *Documentation* section via <http://geant4.in2p3.fr/styled-4/styled-8/>.

- Geant4 10.6 (based on EPDL97)
- Present work (based on EPDL2017)
- ▲ XCOM



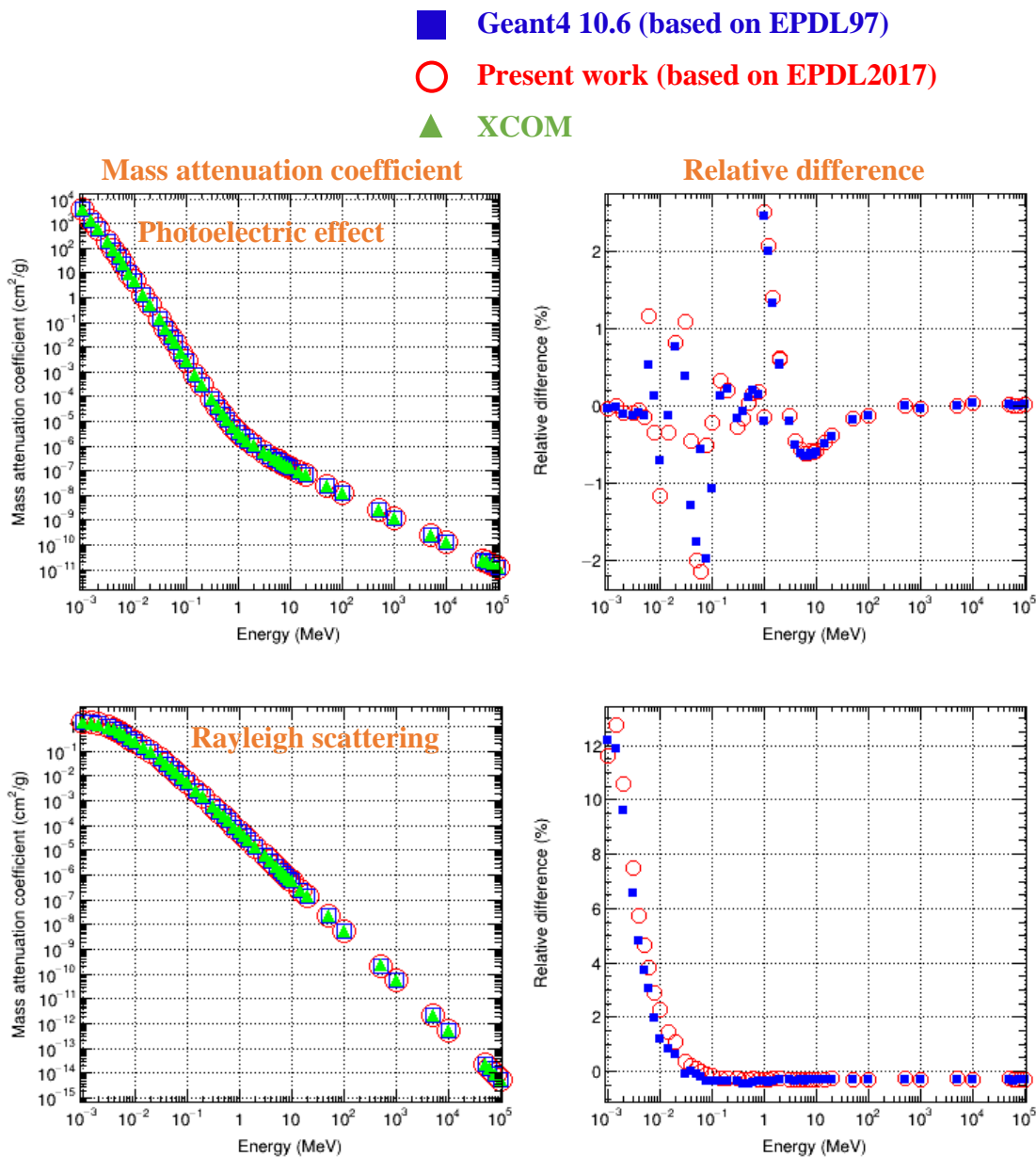


Figure 2 - 23. Mass attenuation coefficient for water as a function of energy (left) in three cases: i) the present work based on EPDL2017; ii) Geant4 10.6 based on EPDL97; iii) XCOM data. Relative difference (right) compared to the XCOM database, for total and each process (equation (2-19)).



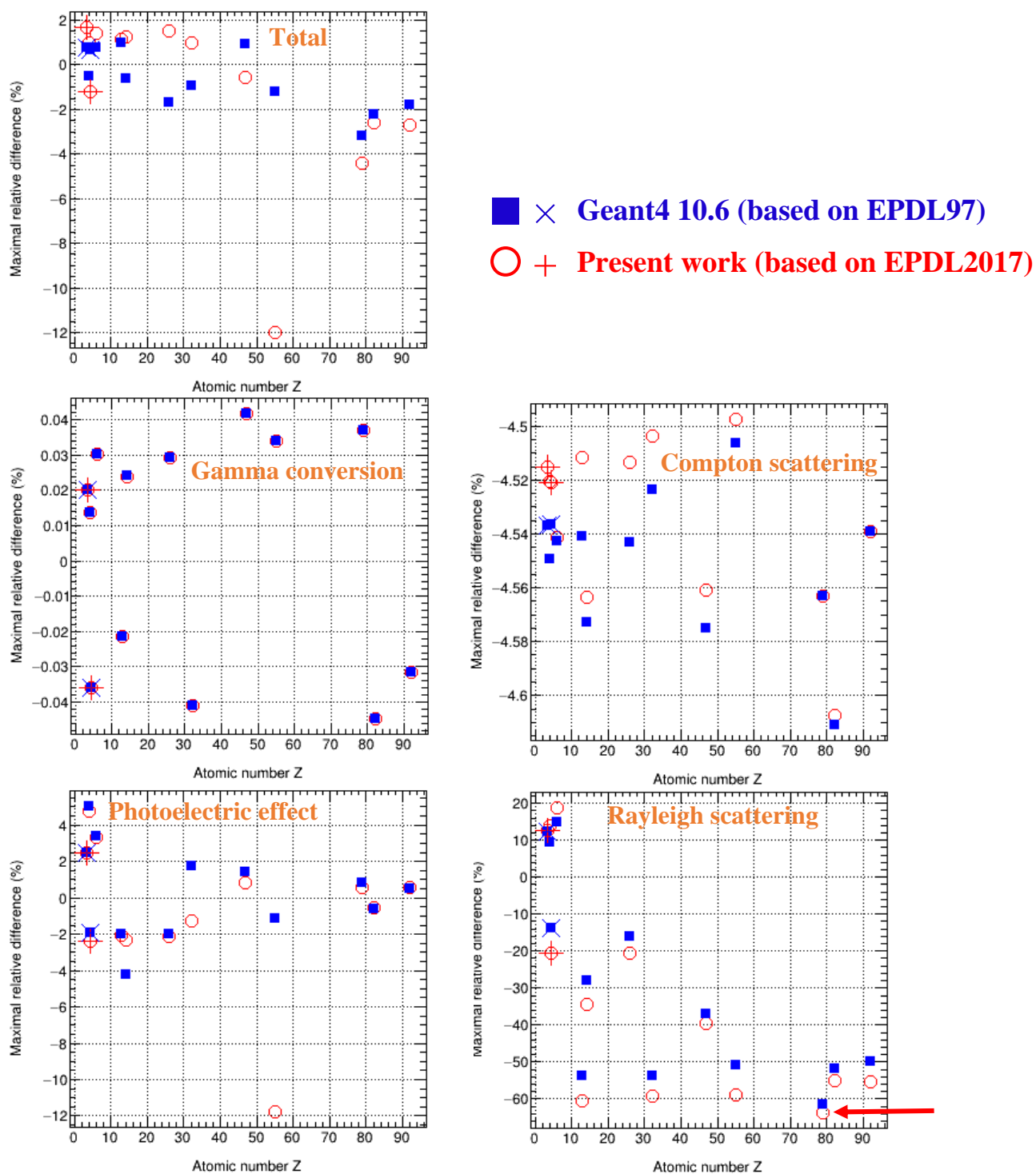


Figure 2 - 24. Maximal relative difference in mass attenuation coefficients as a function of atomic number, for the present work (○ selected chemical elements, + compound materials) and 10.6 (■ selected chemical elements, × for compound materials) compared to XCOM, for total and each process. The values for the selected compound materials are represented according to their effective atomic number: 3.3 for water and 4.4 for ICRU compact bone.

The relative difference is calculated by equation (2-19).

We observed that for the selected elements and compounds, the maximal relative difference for the present work is of the same order of magnitude as for Geant4 10.6 (based on EPDL97):

- For the total attenuation coefficient, the maximal relative difference is less than 4.5% in absolute value for both the present work and Geant4 10.6, except for a noticeable outlier observed for cesium, which is about -12% for the present work, in contrast with -1.2% for Geant4 10.6. This anomalous value results from the difference of cross-section of the *photoelectric effect* at 1 keV, which is exactly the binding energy of cesium, where an abrupt variation of the cross-section occurs (Figure 2 - 25).
- The maximal relative difference for other processes is similar between the present work and Geant4 10.6:
  - Less than 0.045% in absolute value for gamma conversion;
  - 4.7% in absolute value for Compton scattering;
  - 64% in absolute value for Rayleigh scattering (arrow for  $Z = 79$ ) - this large value will be discussed at the end of section 4.3.

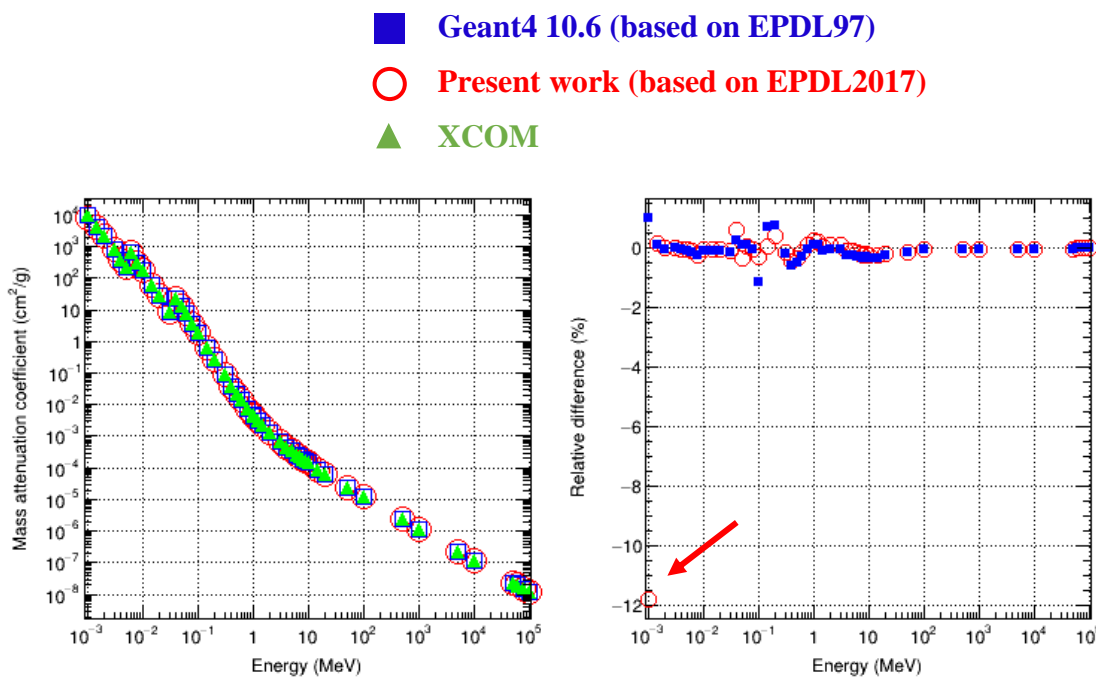


Figure 2 - 25. Mass attenuation coefficient of the photoelectric effect for cesium as a function of energy (left) in three cases: i) the present work based on EPDL2017; ii) Geant4 10.6 based on EPDL97; iii) XCOM data. Relative difference (right) compared to the XCOM database (equation (2-19)). The largest relative difference at 1 keV is clearly visible (arrow).

Since the maximal difference is not always representative due to outliers, we plotted the mean absolute relative difference ( $MD$ ) as a function of  $Z$  (Figure 2 - 26). The  $MD$  was calculated according to equation (2-13) with:

- $m$ , the number of tested energy points for a given material;
- $r_i$ , the relative difference of the  $i$ -th energy point, expressed as equation (2-19).

When compared to XCOM, the  $MD$  for the present work and Geant4 10.6 are similar:

- Less than 0.49% for total;
- 0.015% for gamma conversion;
- 1.3% for Compton scattering;
- 0.67% for photoelectric;
- 17% for Rayleigh scattering (arrow for  $Z=92$ ).

We can notice that for both the present work and Geant4 10.6, large differences were observed at low energies below 100 keV (Figure 2 - 23) for Rayleigh scattering when compared to XCOM, *e.g.*, 64% for maximal relative difference (for  $Z=79$ ), as noticed in Figure 2 - 24 (arrow in “Rayleigh scattering” - bottom right) and 17% for  $MD$  ( $Z=92$ ) in Figure 2 - 26 (arrow in “Rayleigh scattering” - bottom right). Nevertheless, the photoelectric effect dominates in the 100 eV - 100 keV energy range. Thus, the impact of Rayleigh scattering on the precision of the total cross-section is negligible compared to the photoelectric effect. This is visible in Figure 2 - 24 (“Total” - upper left), which confirms that the total mass attenuation coefficient remains very similar for the present work, Geant4 10.6 and XCOM.

4. Comparative study of Geant4 photon models with respect to the XCOM data library

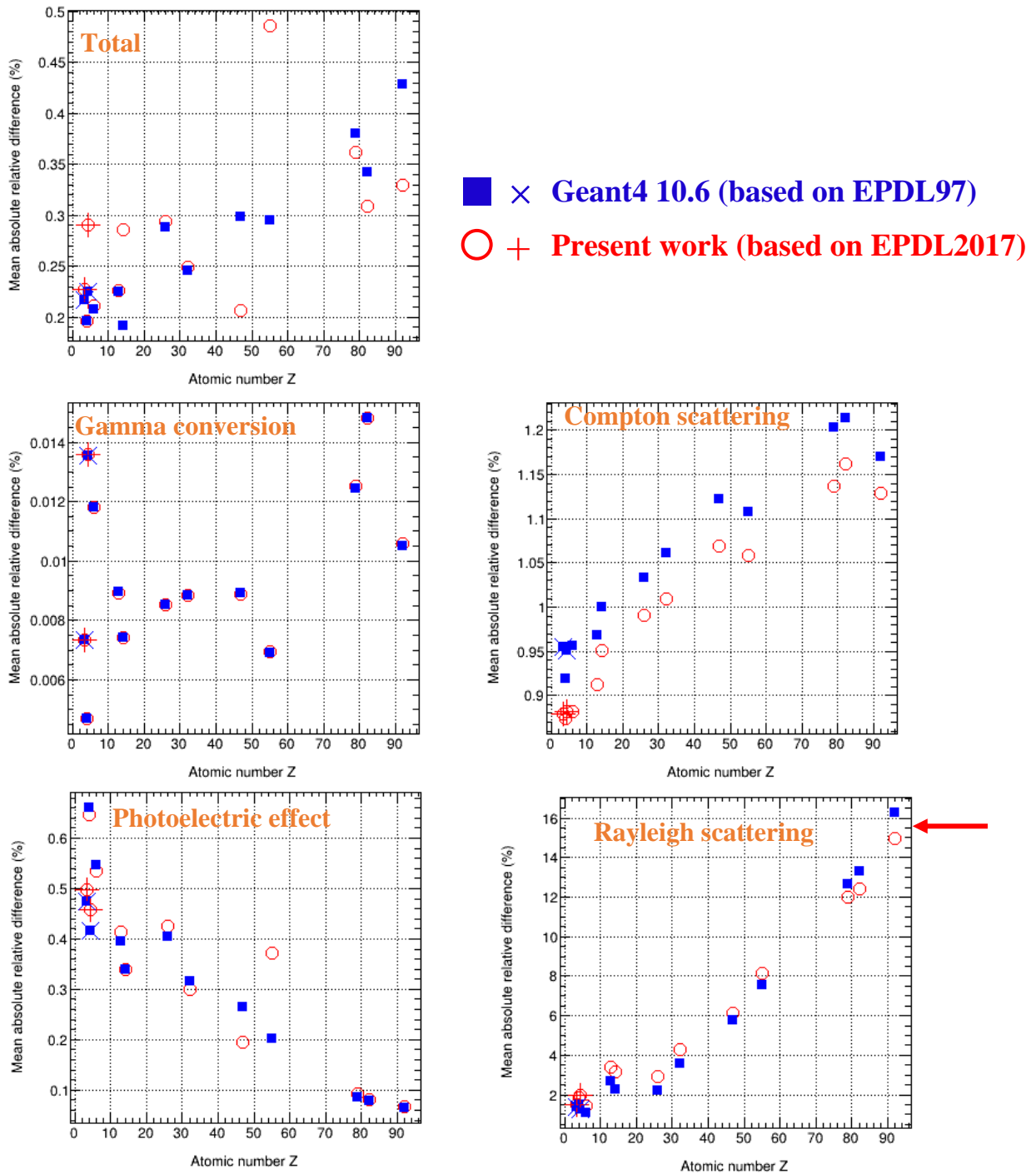


Figure 2 - 26. Mean absolute relative difference in mass attenuation coefficients as a function of atomic number, for the present work (○ selected chemical elements, + compound materials) and Geant4 10.6 (■ selected chemical elements, × compound materials), compared to XCOM, for total and each process. The values for the selected compound materials are represented according to their effective atomic number: 3.3 for water and 4.4 for ICRU compact bone.

## 4.4. Discussion

In the present study, we used the maximal and mean absolute relative difference to quantitatively compare our simulation results with the XCOM data, in order to evaluate our implemented models. However, from the literature, we noticed that many researchers used statistical analysis based on goodness of fit testing to assess the accuracy of their models, in terms of either total mass attenuation coefficient or partial interaction coefficient, with respect to a reference database [13, 15-18]. A  $\chi^2$  test was performed and a confidence level (p-value) was set at a defined value (generally 0.05 or 0.01). The calculation of  $\chi^2$  takes into account the data uncertainties [19], as follows:

$$\chi^2 = \sum_{i=1}^n \frac{(O_i - E_i)^2}{\sigma_i^2} \quad (2 - 20)$$

where:

- $n$  is the number of points;
- $O_i$  the  $i$ -th observed value, from simulation;
- $E_i$  the expected value (reference data);
- $\sigma_i$  the uncertainty on observed values.  $\sigma_i$  consists of the statistical simulation uncertainty, and systematic uncertainty on cross-section data, which is not known precisely on the whole energy range [4].

An appropriate estimation of uncertainty  $\sigma_i$  is important, as it greatly affects the  $\chi^2$  score and corresponding p-value. However, we noticed that in these previous studies in the literature, the calculation of  $\chi^2$  only considered the statistical uncertainty as  $\sigma_i$ , while the systematic uncertainty on cross-section data was not taken into account. The  $\chi^2$  test was nevertheless consistent, because their statistical uncertainty was a few percent, which was roughly of the same order of magnitude as the cross section data uncertainties.

In our case, as explained in section 4.2, our simulations were performed with a higher number of incident photons, which leads to a better statistical precision, less than 0.3%. It would not make sense if we calculated  $\chi^2$  using our statistical uncertainty as  $\sigma_i$ , because it is not representative of the real total uncertainty, which is now dominated by the systematic uncertainty of the cross-section data. Therefore, we did not take into account the  $\chi^2$  test to evaluate our implemented models in the present work, but rather used maximal and mean absolute relative difference.

A second point that we would like to address here is the CPU time variation between Geant4 10.6 and the new version with updated models. Since our new parameterizations are based on the same type of fitting functions as Geant4 10.6, the simulations made with updated models are expected to have a similar CPU time performance. This was verified by simulations with different elements and different incident photon energies.

## 5. Conclusion

In this work, we presented in detail the implementation of EPDL2017 database for Geant4 Livermore photon models, which have been included in December 2021, in Geant4 11.0 release. We updated the data relevant to four photon processes:

- The gamma conversion: cross-section;
- Compton scattering: cross-section and scattering function;
- The photoelectric effect: cross-section;
- Rayleigh scattering: cross-section and form factor.

The parameterizations used in Geant4 10.6 were updated in order to be suited to EPDL2017 data. The relative differences of the fitted values with respect to the tabulated values were quantitatively investigated for updated parameterizations, and then compared with those for the parameterizations in Geant4 10.6:

- For Compton effect, as explained in section 3.2, the precision of the updated parameterization of scattering function was improved compared to Geant4 10.6, by a factor of roughly 1000 for region 1 and 2.8 for region 2 (scattering functions were fitted in two intervals). As previously discussed, the factor of 1000 does not mean the parameterization in Geant4 10.6 was bad, as in region 1, the individual differences were relatively small (5-10%) and, moreover, this region corresponds to low values of scattering function.
- For the photoelectric effect, the precision of the updated parameterization was improved by a factor of 1.9 for low energy region and 1.3 for high energy region of total cross-sections (also fitted in two intervals);
- For Rayleigh scattering, the parameterization of form factor was improved by a factor of 1.3.

The rest of data were directly tabulated in Geant4. Geant4 reads the tabulated data and does its own interpolation to calculate the cross-section at a given energy point. The way Geant4 interpolates, depends on the nature of the data that Geant4 reads. Considering that EPDL2017 uses linear interpolation, thus it had to be also applied in Geant4 11.0 models, while Geant4 10.6 used logarithmic interpolation, which was specified in EPDL97.

As described in section 4, the updated models were tested through a comparative study regarding mass attenuation coefficients. The mass attenuation coefficients for total and each process were calculated with Geant4 10.6 and updated models, respectively, for selected elements and compounds. A good agreement with XCOM data was observed, except for Rayleigh scattering below 100 keV. However, in this energy range, the photoelectric effect dominates, so there was little impact on the precision of total mass attenuation coefficient. The mean absolute relative difference of total mass attenuation coefficients between simulation results (using both Geant4 10.6 and updated models) and XCOM, did not exceed

0.49%. This comparison thus confirmed the very good agreement between the simulation results obtained with our updated models and XCOM data.

The update of Livermore photon models using EPDL2017 is described in detailed in several technical notes (one for each process), available in the Geant4@IN2P3 website<sup>3</sup>.

---

<sup>3</sup> The technical notes for photons are available in the Geant4@IN2P3 website of *Documentation* section via <http://geant4.in2p3.fr/styled-4/styled-8/>.

## References

- [1] Cullen DE. EPICS2017: April 2019 status report. IAEA-NDS-228. 2019. <https://www-nds.iaea.org/epics/DOCUMENTS/2019-EPICS2017-Status.pdf>.
- [2] Cullen DE. A Survey of Atomic Binding Energies for use in EPICS2017. IAEA-NDS-224. 2018. <https://www-nds.iaea.org/publications/nds/iaea-nds-0224/>.
- [3] Cullen DE. A Survey of Electron Cross Section Data for use in EPICS2017. IAEA-NDS-226. 2017. <https://www-nds.iaea.org/publications/nds/iaea-nds-0226/>.
- [4] Cullen DE. A survey of photon cross section data for use in EPICS2017. IAEA-NDS-225. 2018. <https://www-nds.iaea.org/publications/nds/iaea-nds-0225/>.
- [5] Misaki A. The Landau - Pomeranchuk - Migdal (LPM) effect and its influence on electromagnetic cascade showers at extremely high energies. Nuclear Physics B - Proceedings Supplements. 1993;33(1):192-9. [https://doi.org/10.1016/0920-5632\(93\)90091-J](https://doi.org/10.1016/0920-5632(93)90091-J).
- [6] Ivanchenko V, Bagulya A, Bakr S, Bandieramonte M, Bernard D, Bordage M-C, et al. Geant4 electromagnetic physics progress. EPJ Web of Conferences. 2020;245. <https://doi.org/10.1051/epjconf/202024502009>.
- [7] Hubbell JH. Summary of existing information on the incoherent scattering of photons, particularly on the validity of the use of the incoherent scattering function. Radiat Phys Chem. 1997;50:113-24. [https://doi.org/10.1016/S0969-806X\(97\)00049-2](https://doi.org/10.1016/S0969-806X(97)00049-2).
- [8] Cullen DE. A simple model of photon transport. Nucl Instrum Methods Phys Res B. 1995;101(4):499-510. [https://doi.org/10.1016/0168-583X\(95\)00480-7](https://doi.org/10.1016/0168-583X(95)00480-7).
- [9] Scofield JH. Theoretical photoionization cross sections from 1 to 1500 keV. UCRL-51326. 1973. <https://doi.org/10.2172/4545040>.
- [10] Hubbell JH, Overbo I. Relativistic atomic form factors and photon coherent scattering cross sections. J Phys Chem Ref Data. 1979;8(1):69-106. <https://doi.org/10.1063/1.555593>.
- [11] Batic M, Hoff G, Pia MG, Saracco P. Photon Elastic Scattering Simulation: Validation and Improvements to Geant4. IEEE Trans Nucl Sci. 2012;59(4):1636-64. <https://doi.org/10.1109/tns.2012.2203609>.
- [12] Physical Aspects of Irradiation: Recommendations of the International Commission on Radiological Units and Measurements (ICRU) Report 10B 1962. U.S. Department of Commerce, National Institute of Standards and Technology; 1964. <https://nvlpubs.nist.gov/nistpubs/Legacy/hb/nbshandbook85.pdf>.
- [13] Amako K, Guatelli S, Ivanchenko VN, Maire M, Mascialino B, Murakami K, et al. Comparison of Geant4 electromagnetic physics models against the NIST reference data. IEEE Trans Nucl Sci. 2005;52(4):910-8. <https://doi.org/10.1109/tns.2005.852691>.
- [14] Arce P, Bolst D, Bordage MC, Brown JMC, Cirrone P, Cortés-Giraldo MA, et al. Report on G4-Med, a Geant4 benchmarking system for medical physics applications developed by the Geant4 Medical Simulation Benchmarking Group. Med Phys. 2021;48(1):19-56. <https://doi.org/10.1002/mp.14226>.



- [15] Cirrone GAP, Cuttone G, Di Rosa F, Pandola L, Romano F, Zhang Q. Validation of the Geant4 electromagnetic photon cross-sections for elements and compounds. Nucl Instrum Methods Phys Res A. 2010;618(1-3):315-22. <https://doi.org/10.1016/j.nima.2010.02.112>.
- [16] Weidenspointner G, Batic M, Hauf S, Hoff G, Kuster M, Pia MG, et al. Validation of Compton scattering Monte Carlo simulation models. 2013 IEEE Nuclear Science Symposium and Medical Imaging Conference (2013 NSS/MIC); 2013: IEEE. <https://doi.org/10.1109/NSSMIC.2013.6829500>.
- [17] Guatelli S, Mascialino B, Pia M, Piergentili M, Pandola L, Parlati S, et al. Precision validation of Geant4 electromagnetic physics. American Nuclear Society Topical Meeting in Monte Carlo; 2005. <https://www.ge.infn.it/geant4/papers/2005/mc2005/validation.pdf>.
- [18] Begalli M, Hoff G, Pia MG, Saracco PG. Validation of geant4 electron pair production by photons. 2013 IEEE Nuclear Science Symposium and Medical Imaging Conference; 2013. <https://doi.org/10.48550/arXiv.1311.5155>.
- [19] Cirrone GAP, Donadio S, Guatelli S, Mantero A, Mascialino B, Parlati S, et al. A goodness-of-fit statistical toolkit. IEEE Trans Nucl Sci. 2004;51(5):2056-63. <https://doi.org/10.1109/TNS.2004.836124>.

# Chapter 3: Updates in EEDL2017 and their impact on Livermore models

---

## 1. Introduction

Geant4 allows for the simulation of electron interactions in matter, including electron scattering, ionisation and bremsstrahlung processes. Livermore models, which are specifically designed for ionisation and bremsstrahlung processes, are based on the EEDL91 database. Therefore, the objective of this chapter is to identify the differences between the EEDL91 and EEDL2017 databases and assess their potential impact on Livermore models.

In this chapter, we will begin by presenting all the relevant physical quantities for electrons that are available in EEDL2017 and identify those that are directly or indirectly used in Livermore models. Subsequently, we will study the modifications of these physical quantities in EEDL2017 in comparison to EEDL91. As highlighted in chapter 2, a major modification in EPICS2017 is the change in binding energies. To ensure consistency in the data, these new binding energies were updated to the ionisation subshells, resulting in changes in subshell cross-sections and energy spectra. To assess the impact of this update on Livermore models and determine the necessity of implementing EEDL2017, we will specifically study the ionisation cross-sections and collision stopping power, which are fundamental physical quantities used in the modeling of the ionisation process.

## 2. Electron data in EEDL2017

In EPICS2017, the sub-library that describes the interaction of electrons with matter is the Evaluated Electron Data Library (EEDL2017). It provides complete information for particle transport covering elements with  $Z = 1-100$  and incident electron energies ranging from 10 eV to 100 GeV. We will firstly present the physical quantities available in the database and describe their format [1]. Subsequently, we will conduct a comparative study between EEDL2017 and EEDL91.

### 2.1. Physical quantities for electrons

The physical quantities available in the database are as follows:

#### i) Elastic transport

- Transport cross section (barn).

#### ii) Large angle elastic scattering

- Integrated large angle scattering cross section (barn);
- Average energy of the scattered electron (MeV);
- Average energy to the residual atom, *i.e.*, local deposition (MeV);
- Angular distribution of the scattered electron.

#### iii) Elastic scattering

- Integrated scattering cross section (barn).

#### iv) Ionisation

- Integrated **total** cross section (barn);
- Integrated **subshell** cross section (barn);
- Average energy of the scattered electron (MeV) by subshell;
- Average energy of the recoil electron (MeV) by subshell;
- Spectra of the recoil electron.

#### v) Bremsstrahlung

- Integrated cross section (barn);
- Average energy of the secondary electron and positron (MeV);
- Average energy of the secondary positron (MeV);
- Spectra of the secondary photon.

#### vi) Excitation

- Integrated cross section (barn);
- Average energy to the residual atom, *i.e.*, local deposition (MeV).

## 2.2. Format of data

### 2.2.1. Structure of data

Similar to EPDL2017 in EPICS2017, EEDL2017 contains a series of tables in **ASCII format**. Each table starts with **two header lines** that contain the parameters related to the physical data (Figure 3 - 1). These two header lines are followed by a series of two (or three)-column **physical data lines**, one data point per line. Each table is terminated by an end of table line which is blank except for a “1” placed in column 72 (column 72 is blank on all other lines in the table).

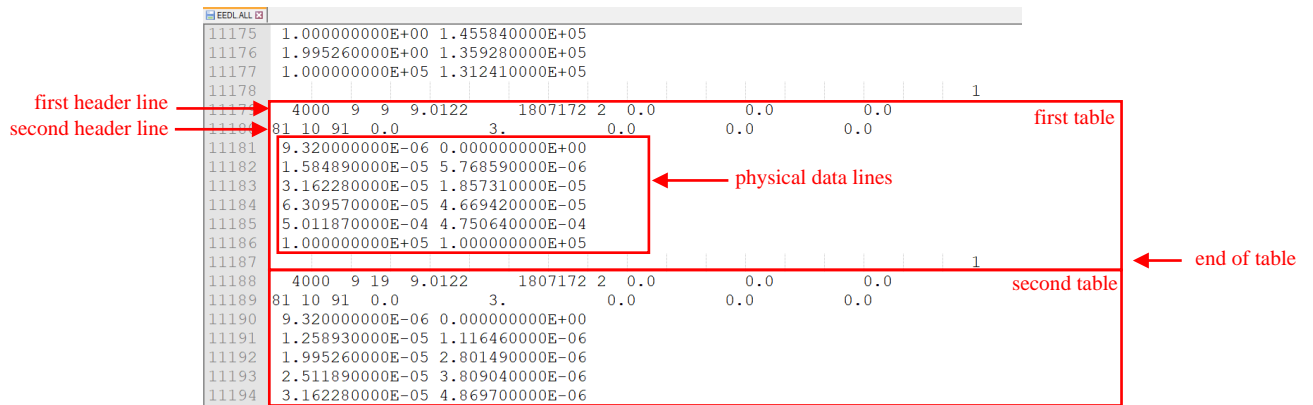


Figure 3 - 1. Example of two tables contained in EEDL2017. Header lines, end of table line and physical data lines are indicated (red arrows).

### 2.2.2. Information in the first header line

As an example, some detailed explanations are given in Figure 3 - 2 for the first header line, extracted from the first table presented in Figure 3 - 1.

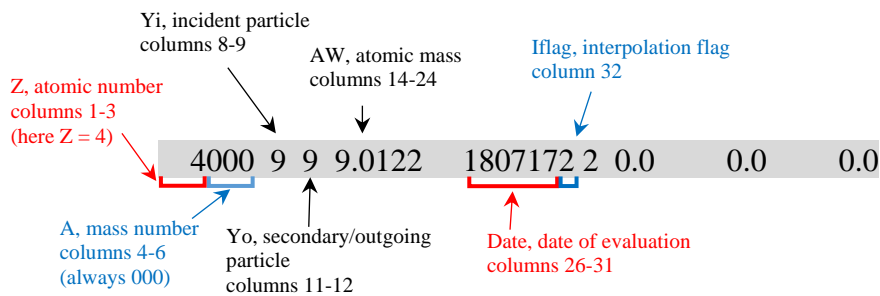


Figure 3 - 2. Information in the first header line of a table.

Additional information:

- For mass number, in all cases  $A = 0$  (for elemental data)
- For **incident particle (i index)**:
  - $Y_i = 9$ , electron
- For secondary/**outgoing particle (o index)**:

- $Y_0 = 0$ , no secondary/outgoing particle
- $Y_0 = 7$ , photon
- $Y_0 = 9$ , electron
- $Y_0 = 19$ , electron as recoil
- For date: YYMMDD
- For interpolation flag:
  - Iflag = 0, or 2, linear in x and y
  - Iflag = 3, logarithmic in x, linear in y
  - Iflag = 4, linear in x, logarithmic in y
  - Iflag = 5, logarithmic in x and y

### 2.2.3. Information in the second header line

Figure 3 - 3 illustrates the information contained in the second header line, extracted from the first table presented in Figure 3 - 1.

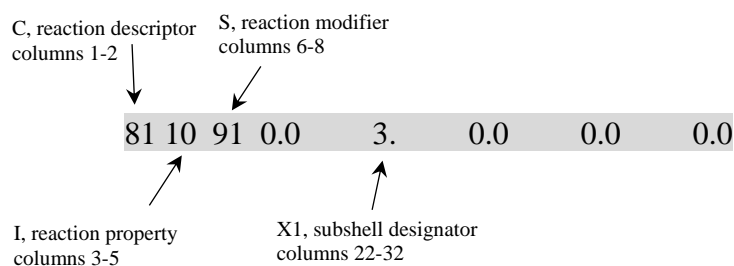


Figure 3 - 3. Information in the second line of a table.

Additional information:

- For reaction descriptor (it is equivalent to the notion “physical process” used in Geant4):
  - C = 7, elastic transport
  - C = 8, large angle elastic scattering
  - C = 10, elastic scattering
  - C = 81, ionisation
  - C = 82, bremsstrahlung
  - C = 83, excitation
- For reaction property:
  - I = 0, integrated cross section
  - I = 10, average energy of the secondary particle,  $Y_0$
  - I = 11, average energy to the residual atom
  - I = 21, spectra of recoil particle
  - I = 22, angular distribution
- For reaction modifier:
  - S = 0, no X1 field data required

- S = 91, X1 field data required
- For X1, value depends upon the value of S:
  - S = 0, X1 = 0
  - S = 91, X1 = subshell designator, as shown in Appendix A, Table A - 1.

#### **2.2.4. Physical data lines**

Following the two header lines, the two (or three)-column physical data lines are provided with 10 significant digits. The physical quantities tabulated in these data lines depend on the value of the reaction descriptor and property, which are indicated in the second header line (Figure 3 - 3).

### **2.3. Main changes**

As previously mentioned, a fundamental modification of EPICS2017 is the change in binding energies, which have been updated to electron data in EEDL2017. This update results in changes in related physical quantities, such as the ionisation and excitation cross-sections. On the opposite, some physical quantities, such as bremsstrahlung cross-sections, are not affected as they are independent of the binding energies. Regarding Livermore models, the physical quantities used for modelling electron processes are as follows:

- For ionisation process:
  - The total and subshell cross-sections;
  - The spectra of the recoil electron, which refers to the energy distribution of the emitted electron induced by ionisation.
- For excitation process: the cross-sections;
- For bremsstrahlung process: the cross-sections and energy spectra of the secondary photon.

Amongst those physical quantities, we have checked that the data for bremsstrahlung process remain unchanged in EEDL2017 compared to EEDL91. Therefore, in the following sections (2.4 and 2.5), we will focus on presenting the differences in ionisation and excitation cross-sections between EEDL2017 and EEDL91.

### **2.4. Comparative study of ionisation data**

The objective of this section is to demonstrate the differences in ionisation data between EEDL2017 and EEDL91 with respect to the following aspects

- Total ionisation cross-sections;
- Subshell cross-section;
- Energy spectra of recoil electron.

### 2.4.1. Subshell cross-section comparison

There are 1612 subshells in total for 100 elements ( $Z$ : 1-100). The modification of binding energies in EEDL2017 leads to an energy shift near the binding energy for each subshell [2]. An example is given here for iron, between EEDL2017 and EEDL91 (Figure 3 - 4). More specifically, the shift only occurs in the vicinity of the binding energy, as depicted in Figure 3 - 5, which shows a part of the tabulated data for this subshell. The shift in energy is visible: the subshell cross-section values keep unchanged (in blue), while only energies near the binding energy point are different (in red).

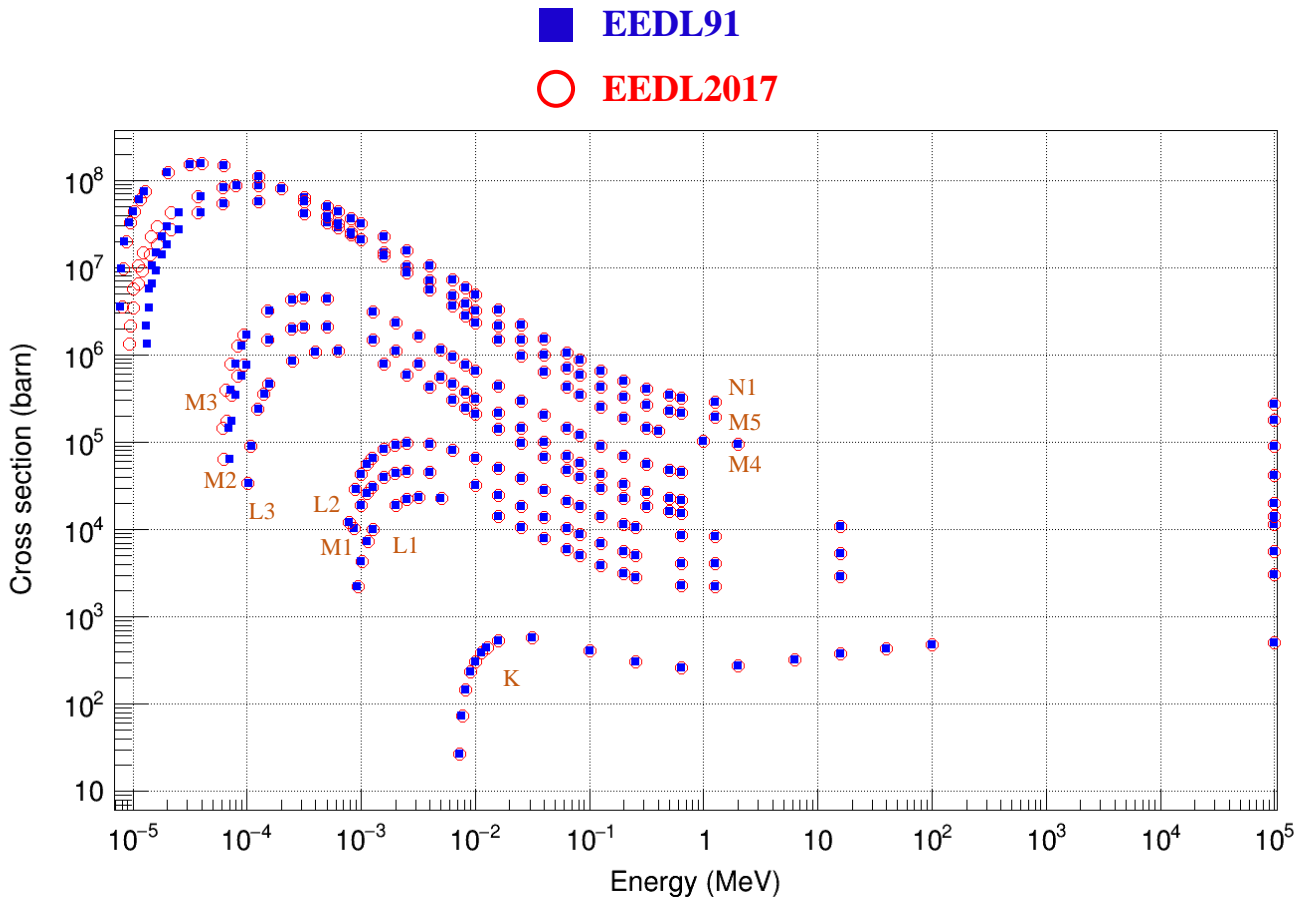


Figure 3 - 4. Subshell cross-sections comparison between EEDL2017 and EEDL91 for iron. The first tabulated point for each subshell corresponds to the binding energy (first point in Figure 3 - 5); the cross-section value at this point is 0, so this point is not plotted.

EEDL91		EEDL2017	
Energy (MeV)	Cross-section (barn)	Energy (MeV)	Cross-section (barn)
0.26000	9.000000+0	0.26000	55.847
0.81000	91.000000+0	0.81000	1807172
1.29100	0.00000+0	9.000000000E-06	0.000000000E+00
1.32774	1.32255+6	9.379763660E-06	1.322550000E+06
1.39203	3.49790+6	1.004429840E-05	3.497900000E+06
1.48846	6.48459+6	1.104104880E-05	6.484590000E+06
1.58489	9.18949+6	1.203779920E-05	9.189490000E+06
1.79008	1.42043+7	1.415874930E-05	1.420430000E+07
1.99526	1.85074+7	1.627959600E-05	1.850740000E+07
2.51189	2.72115+7	2.161975120E-05	2.721150000E+07
3.98107	4.26365+7	3.680595640E-05	4.263650000E+07
6.30957	5.37430+7	6.087453800E-05	5.374300000E+07
1.25893	5.65458+7	1.257850790E-04	5.654580000E+07
3.16228	4.20601+7	3.162280000E-04	4.206010000E+07
5.01187	3.28410+7	5.011870000E-04	3.284100000E+07
6.30957	2.85183+7	6.309570000E-04	2.851830000E+07
8.15479	2.40607+7	8.154790000E-04	2.406070000E+07
1.00000	2.08541+7	1.000000000E-03	2.085410000E+07
1.58489	1.47911+7	1.584890000E-03	1.479110000E+07
2.51189	1.02688+7	2.511890000E-03	1.026880000E+07

Figure 3 - 5. Beginning of the subshell cross-section data in EEDL91 and EEDL2017 for the M4 subshell of iron.

## 2.4.2. Total cross-section comparison

In EEDL91, the total ionisation cross-sections are not available, whereas they are included in EEDL2017. They are calculated by summing up the subshell cross-sections using the appropriate interpolation, *i.e.*, Log-Log interpolation for EEDL91 and Lin-Lin interpolation for EEDL2017. Figure 3 - 6 shows an example of total cross-sections for hydrogen (H), iron (Fe), and lead (Pb). The bottom graph displays the relative difference (*RD*), expressed as follows:

$$RD (\%) = 100 \times \frac{EEDL2017 - EEDL91}{EEDL91} \quad (3 - 1)$$

As expected, we observed large differences at low energies, which correspond to the energy shift observed for the outer subshells (section 2.4.1 of this chapter).



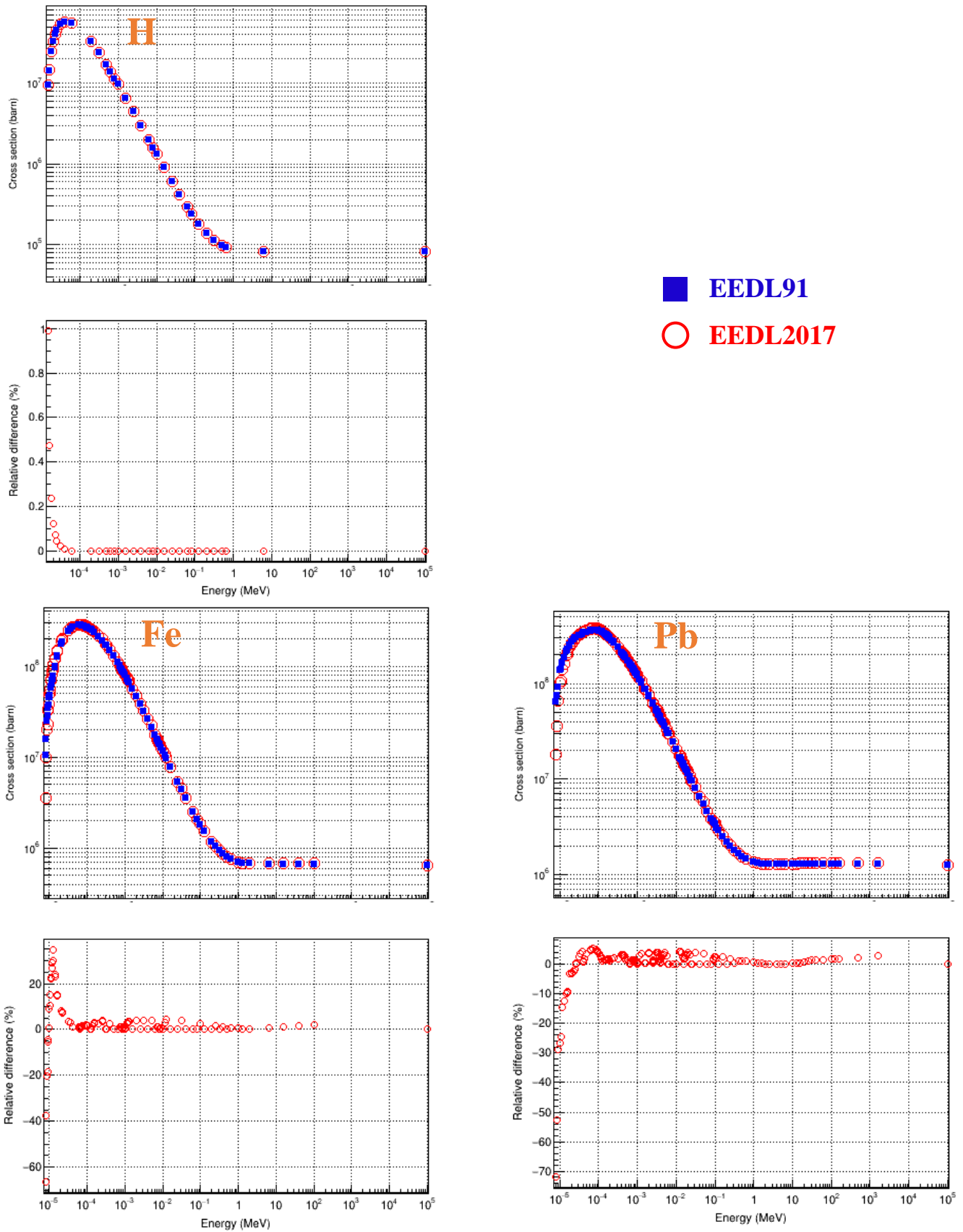


Figure 3 - 6. Comparison of total ionisation cross-section for H, Fe and Pb between EEDL2017 and EEDL91. The relative difference (RD) of EEDL2017 compared to EEDL91 is calculated according to equation (3-1). The energy scale is the same for both cross-sections and RD.

### 2.4.3. Energy spectrum comparison

In EEDL, the energy spectrum data of recoil electrons consists of three columns:

- The first column: energy of incident electron;
- The second column: energy of recoil electron;
- The third column: normalized probability of emission of a recoil electron.

Similar to the changes in subshell cross-sections, the modification of spectrum data only occurs in the vicinity of the binding energy. The energy shift resulting from the binding energy modification is visible for example in Figure 3 - 7 for the M4 subshell of iron: the values in second and third columns remain unchanged, while only the energies of the incident electron in the first column are modified. This type of modification applies to all elements (Z: 1-100) in EEDL2017.

	EEDL91			EEDL2017		
	Energy of incident electron (MeV)	Energy of recoil electron (MeV)	Normalized spectrum distribution	Energy of incident electron (MeV)	Energy of recoil electron (MeV)	Normalized spectrum distribution
Header lines	26000 9 19	0.00000+ 0	890224 2	26000 9 19 55.847	1807172 2 0.0	0.0
	81 21 91	0.00000+ 0	1.30000+ 1	81 21 91 0.0	13.	0.0 0.0
Binding energy	1.29100- 5	1.83683- 9	6.04907+ 7	9.000000000E-06	1.836830000E-09	6.049070000E+07
	1.29100- 5	1.83683- 8	6.04907+ 7	9.000000000E-06	1.836830000E-08	6.049070000E+07
	1.32774- 5	1.83683- 9	5.53588+ 6	1.327740000E-05	1.836830000E-09	5.535880000E+06
	1.32774- 5	1.83683- 7	5.46242+ 6	1.327740000E-05	1.836830000E-07	5.462420000E+06
	8.15479- 5	1.00000- 7	7.33647+ 4	8.154790000E-05	1.000000000E-07	7.336470000E+04
	8.15479- 5	3.54814- 7	6.84392+ 4	8.154790000E-05	3.548140000E-07	6.843920000E+04
	8.15479- 5	1.25893- 6	6.38444+ 4	8.154790000E-05	1.258930000E-06	6.384440000E+04
	8.15479- 5	2.81839- 6	5.23799+ 4	8.154790000E-05	2.818390000E-06	5.237990000E+04
	8.15479- 5	6.30957- 6	4.29741+ 4	8.154790000E-05	6.309570000E-06	4.297410000E+04
	8.15479- 5	9.99999- 6	3.37216+ 4	8.154790000E-05	9.999990000E-06	3.372160000E+04
	8.15479- 5	1.58489- 5	2.64612+ 4	8.154790000E-05	1.584890000E-05	2.646120000E+04
	8.15479- 5	2.33220- 5	1.88940+ 4	8.154790000E-05	2.332200000E-05	1.889400000E+04
	8.15479- 5	3.43189- 5	1.34909+ 4	8.154790000E-05	3.431890000E-05	1.349090000E+04
	1.99526- 3	1.00000- 7	4.59509+ 4	1.995260000E-03	1.000000000E-07	4.595090000E+04
	1.99526- 3	3.98107- 7	4.22997+ 4	1.995260000E-03	3.981070000E-07	4.229970000E+04
	1.99526- 3	1.58489- 6	3.89387+ 4	1.995260000E-03	1.584890000E-06	3.893870000E+04
	1.99526- 3	3.16227- 6	3.28611+ 4	1.995260000E-03	3.162270000E-06	3.286110000E+04
	1.99526- 3	6.30957- 6	2.77321+ 4	1.995260000E-03	6.309570000E-06	2.773210000E+04
	1.99526- 3	1.12202- 5	2.09447+ 4	1.995260000E-03	1.122020000E-05	2.094470000E+04
	1.99526- 3	1.99526- 5	1.58185+ 4	1.995260000E-03	1.995260000E-05	1.581850000E+04
	1.99526- 3	2.51189- 5	1.27690+ 4	1.995260000E-03	2.511890000E-05	1.276900000E+04
	1.99526- 3	3.16228- 5	1.03074+ 4	1.995260000E-03	3.162280000E-05	1.030740000E+04
	1.99526- 3	3.98107- 5	7.36407+ 3	1.995260000E-03	3.981070000E-05	7.364070000E+03

Figure 3 - 7. Beginning of energy spectrum data for ionisation process in EEDL2017 and EEDL91 for the M4 subshell of iron.

## 2.5. Comparison of excitation cross-sections

Excitation cross-sections remain unchanged in EEDL2017 for the majority of elements. However, some elements exhibit differences, which only occur at low energy (Figure 3 - 8).

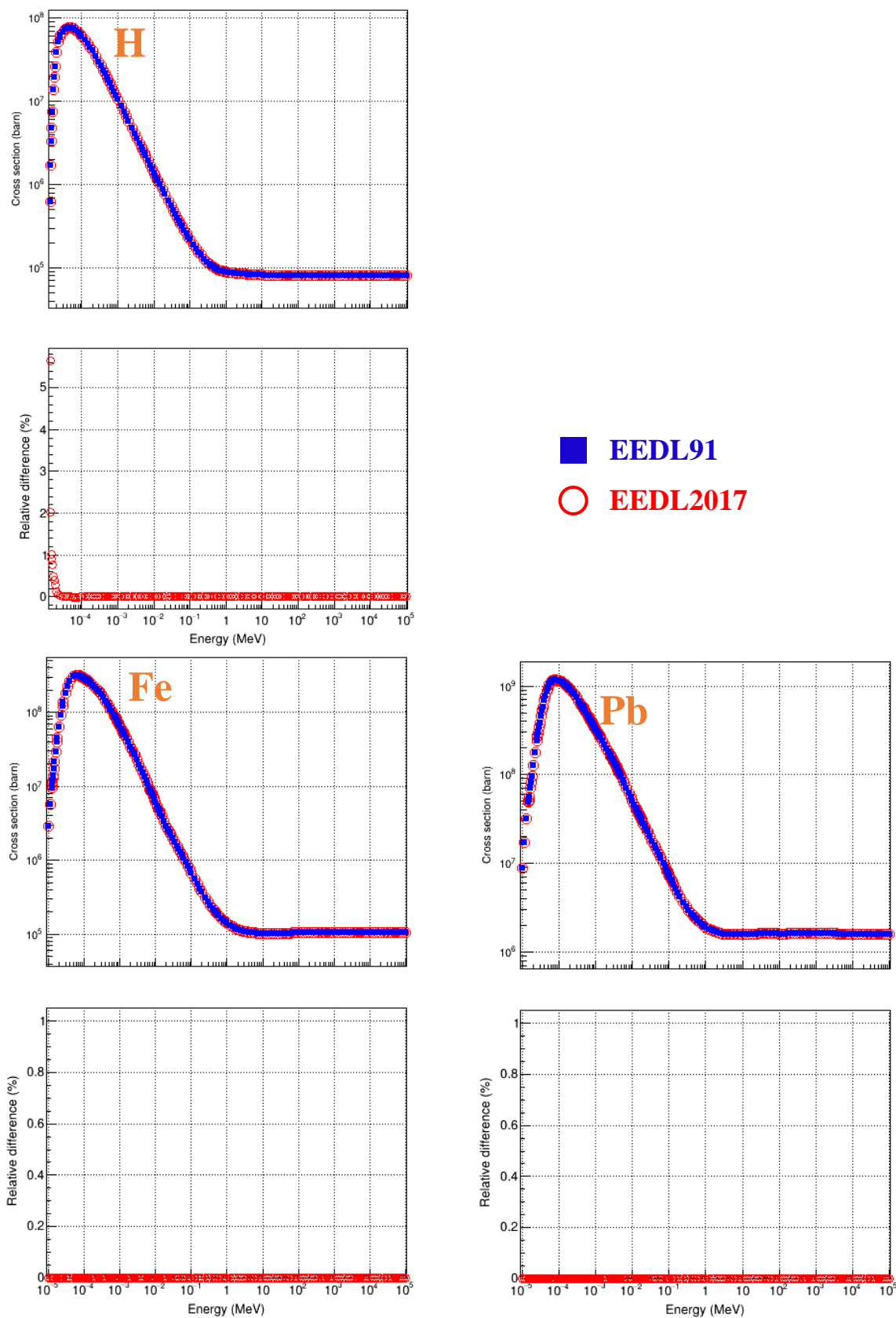


Figure 3 - 8. Comparison of excitation cross-section for H, Fe and Pb between EEDL2017 and EEDL91. The relative difference (RD) of EEDL2017 compared to EEDL91 is calculated according to equation (3-1). The energy scale is the same for both cross-sections and RD.

## 2.6. Discussion

In section 2.3, we listed all the physical quantities used for Livermore electron models. Based on the comparison between EEDL2017 and EEDL91, we have shown that not all these physical quantities are modified in EEDL2017. As explained in section 2.3, the data regarding bremsstrahlung are not modified. For this reason, Livermore bremsstrahlung model will not require any updates. However, ionisation and excitation cross-sections, as well as energy spectra induced by ionisation, exhibit differences at low energy, due to the modifications of binding energies. Consequently, it is important to evaluate the impact of those differences on the following physical values calculated by Livermore models, more specifically by the *G4LivermoreIonisationModel* class:

- Ionisation cross-section;
- Energy loss - related to ionisation, excitation cross-sections and recoil electron spectrum.

### 3. Livermore ionisation model

The objective of this section is to introduce the Livermore ionisation model and explain its calculation process of cross-section and stopping power.

#### 3.1. Ionisation process in Geant4

The ionisation process occurs when an incident electron interacts with orbital electrons, leading to the generation of a secondary electron. In the simulation, Geant4 imposes a parameter called production cut  $T_{cut}$  for secondary particles, which corresponds to the minimum energy of a secondary electron that can be generated by an interaction [3]. Indeed,  $T_{cut}$  is used to control the level of detail in the simulation, aiming to improve the computational efficiency by excluding low-energy secondary particles that may not significantly impact the final results.

In Geant4, the ionisation process is handled by the *G4eIonisation* class, which has discrete and continuous components [3, 4]:

- If the discrete interaction is invoked, a secondary electron with energy  $t$  above  $T_{cut}$  is explicitly generated. The probability of this interaction is determined by the *restricted* cross-section (section 3.2);
- In the continuous interaction, the mean energy loss per unit length, also known as the stopping power, is calculated by the *restricted* stopping power along the step (section 3.3).

The combination of continuous and discrete interactions in Geant4 enables accurate simulation of the behavior of electrons as they interact with matter. More precisely, the total energy loss  $\Delta E$  of incident electron during an interaction step due to ionisation is calculated as follows:

$$\Delta E = \Delta E_{continuous} + \Delta E_{discrete} \quad (3 - 2)$$

where:

- $\Delta E_{continuous}$  is the *restricted* energy loss calculated from continuous interaction, which is considered as energy deposited locally;
- $\Delta E_{discrete}$  is the energy loss during the discrete interaction, if invoked.

The ionisation process in the Livermore model is implemented through the *G4LivermoreIonisationModel* class. The accuracy of the model depends on the precise calculation of cross-section (section 3.2) and stopping power (section 3.3). Therefore, the decision to update the Livermore model (initially based on EEDL91) with EEDL2017 requires comparing the cross-sections and stopping powers obtained from Livermore ionisation model and EEDL2017.

### 3.2. Calculation of ionisation cross-section

When a discrete interaction is invoked, the secondary electron with energy *above*  $T_{cut}$  is explicitly simulated through a discrete interaction. The probability of this interaction is determined by the *restricted* cross-section  $\sigma(E, T_{cut})$ , which is calculated by Livermore ionisation model as follows [4, 5]:

$$\sigma(E, T_{cut}) = \int_{T_{cut}}^{T_{max}} \frac{d\sigma(E, t)}{dt} dt = \sum_{s=0}^{n-1} \left( \sigma_s(E) \frac{\int_{T_{cut}}^{T_{max}} \frac{d\sigma}{dt} dt}{\int_{0.1eV}^{T_{max}} \frac{d\sigma}{dt} dt} \right) \quad (3-3)$$

where:

- $t$  is the kinetic energy of secondary electron;
- $E$  is the energy of incident electron;
- $\frac{d\sigma}{dt}$  is the distribution of cross-sections as a function of the kinetic energy  $t$  of the secondary electron. *It is calculated through a parameterization of the energy spectrum data in EEDL;*
- $T_{max} = 0.5E$  is the maximum energy transferred to a secondary electron;
- $\sigma_s(E)$  is the subshell cross-section obtained from an interpolation of the tabulated cross-section data in EEDL, and 0.1 eV is the low energy limit of secondary electron in EEDL;
- $s$  is the considered subshell;
- $n$  is the total number of subshells.

During a Geant4 simulation, the *restricted* cross-section  $\sigma(E, T_{cut})$  for a given energy of incident electron  $E$  and production  $T_{cut}$  is obtained using the `ComputeCrossSectionPerAtom()` method implemented in `G4LivermoreIonisationModel`.

### 3.3. Calculation of continuous energy loss

Whatever the case, the discrete interaction being invoked or not, the continuous interaction is always simulated, in which the restricted energy loss below  $T_{cut}$ , is calculated. The *restricted* energy loss is obtained by multiplying the interaction step length by the *restricted* stopping power. In Livermore model, the *restricted* stopping power due to ionisation [4, 5] is expressed via the sum over all atomic subshells  $s$  and the integral over the energy  $t$  of secondary electron:

$$-\frac{dE(E, T_{cut})}{dx} = n_{at} \int_0^{T_{lim}} \frac{d\sigma(E, t)}{dt} t dt = n_{at} \sum_{s=0}^{n-1} \left( \sigma_s(E) \frac{\int_{0.1eV}^{T_{lim}} \frac{d\sigma}{dt} t dt}{\int_{0.1eV}^{T_{max}} \frac{d\sigma}{dt} dt} \right) \quad (3-4)$$

where:

- $E$  is the energy of incident electron;
- $T_{lim} = \min(T_{cut}, T_{max})$  is the maximal energy transferred during a continuous interaction;
- $n_{at}$  is the number of atoms per unit volume in the material.

Here the *restricted* cross-section  $\frac{d\sigma}{dt}$  is calculated using the same parameterization of the energy spectra as mentioned in section 3.2. The calculation of *restricted* stopping power at a given energy can be retrieved using the *ComputeDEDXPerVolume()* method in *G4LivermoreIonisationModel*. However, it should be noted that the value returned by *ComputeDEDXPerVolume()* is not the *restricted* stopping power only due to ionisation. Actually it is the *restricted collision stopping power*, which is the energy loss per unit length induced by *both ionisation and excitation*. Contrary to the ionisation process, the excitation is not explicitly modelled, but its contribution to the energy loss, which does not depend on  $T_{cut}$ , is directly included in the ionisation model.

## 4. Comparison of ionisation cross-section and stopping power between Livermore model and EEDL2017

The objective of this section is to compare the cross-sections and stopping powers calculated from the existing Livermore ionisation model with those corresponding to EEDL2017. More precisely, 73 energy points were chosen, ranging from 10 eV to 1 GeV, with 10 points evenly spaced in log scale for each energy interval: 10 eV - 100 eV; 100 eV - 1 keV; ...; 100 MeV - 1 GeV. The following methods in the *G4LivermoreIonisationModel* are used to obtain the cross-sections and stopping powers at these energies:

- *ComputeCrossSectionPerAtom()* to calculate the cross-section;
- *ComputeDEDXPerVolume()* to calculate the collision stopping power.

### 4.1. Cross-section

As described in equation (3-3), the *ComputeCrossSectionPerAtom()* calculates the cross-section of generating a secondary electron with energy *above*  $T_{cut}$ . For this reason, to obtain the total ionisation cross-section,  $T_{cut}$  should be 0. However, as the minimal energy of secondary electron considered in EEDL is 0.1 eV, in practice we took  $T_{cut} = 0.1$  eV instead of 0 for the calculation. We checked that the results, as expected, keep unchanged if we took values of  $T_{cut}$  below 0.1 eV. Figure 3 - 9 shows the ionisation cross-section comparisons for H, Fe and Pb taken as examples. The bottom graph shows the relative difference (*RD*) of EEDL91 and EEDL2017 cross-sections, compared to Livermore:

$$RD (\%) = 100 \times \frac{EEDL - Livermore}{Livermore} \quad (3 - 5)$$



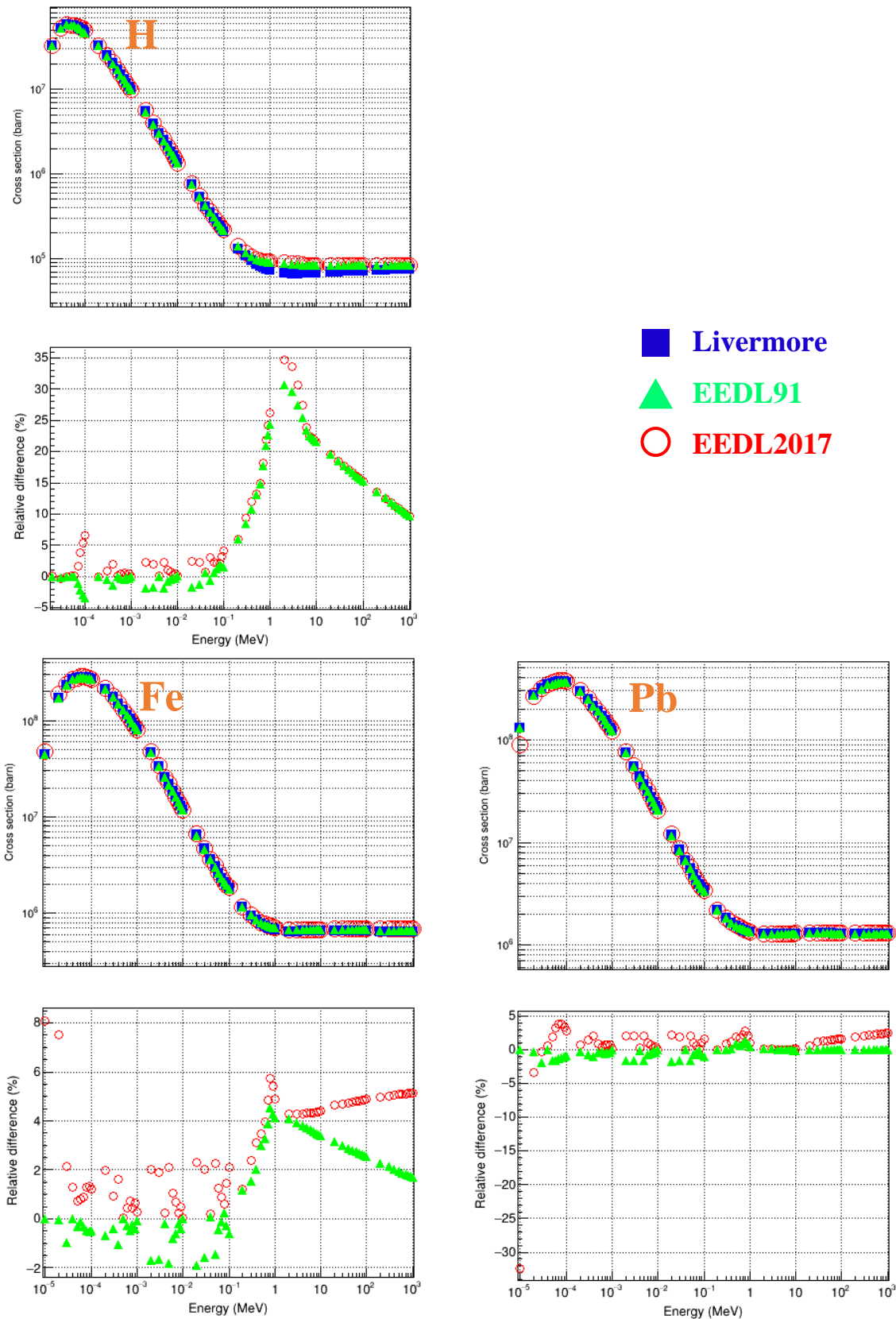


Figure 3 - 9. Ionisation cross-section of EEDL2017, EEDL91 and those calculated from the existing Livermore model, for H, Fe and Pb. The relative difference (RD) of EEDL2017 compared to EEDL91 is calculated according to equation (3-5). The energy scale is the same for both cross-sections and RD.

As explained in section 3.2, the calculation of cross-section by the existing Livermore ionisation model is via a parameterization based on EEDL91. We can see that the calculated cross-sections by Livermore model are also in agreement with EEDL2017. The corresponding relative difference values (red circles) are similar to those obtained with EEDL91 (green triangles), except in a very narrow region at low energy, which corresponds to the energy shift observed for the outer subshells, as shown in section 2.4.1. For this reason, we can conclude that updating the Livermore model is unnecessary regarding cross-sections.

## 4.2. Stopping power

### 4.2.1. EPICSHOW

EEDL2017 and EEDL91 do not contain stopping power data. However, Dr. Cullen has kindly and generously provided us with the EPICSHOW (Electron Photon Interactive Code - Show Data) program (Figure 3 - 10) ([https://inis.iaea.org/collection/NCLCollectionStore/\\_Public/30/022/30022812.pdf?r=1](https://inis.iaea.org/collection/NCLCollectionStore/_Public/30/022/30022812.pdf?r=1)), which can be used to compute and plot the stopping power corresponding to EEDL2017. It provides ionisation, bremsstrahlung, excitation and total stopping powers. To make a plot, we can simply choose the appropriate buttons: “Electrons”+ “Deposit” + “Blk/White”.

EPICSHOW (Version 2022-1)						Use MOUSE to Start	
Lin/Log X	Zoom X	Grid + 1	Legend	Photons	Major	Z + 1	2 X 2
Lin/Log Y	Show All	Grid - 1	Bigger	Electrons	Minor	Z + 10	Listing
Points	Ratio		Smaller	Positrons	Deposit	Z - 1	Pstscript
Blk/White	+ Energy	Mixture		Charged	Range	Z - 10	Same Plot
Freeze!!!	- Energy	barn-1/cm	ColorDump	Neutrons	Straggle	Same Z	Stop

```

Program EPICSHOW
  (Version 2022-1)
      by
  Dermott E. Cullen
  University of California, Retired
  =====(Present Address)=====
    1466 Hudson Way
    Livermore, CA 94550
    U.S.A.

  Tele: 925-443-1911
  E.Mail: redcullen1@comcast.net
  Website: redcullen1.net/HOMEPAGE.NEW/
  
```

Figure 3 - 10. Interface of EPICSHOW program.

An example of the stopping power of H obtained from EPICSHOW is given in Figure 3 - 11. EPICSHOW also produces data in text format, which we used to perform the comparison with the stopping powers calculated from Livermore model.

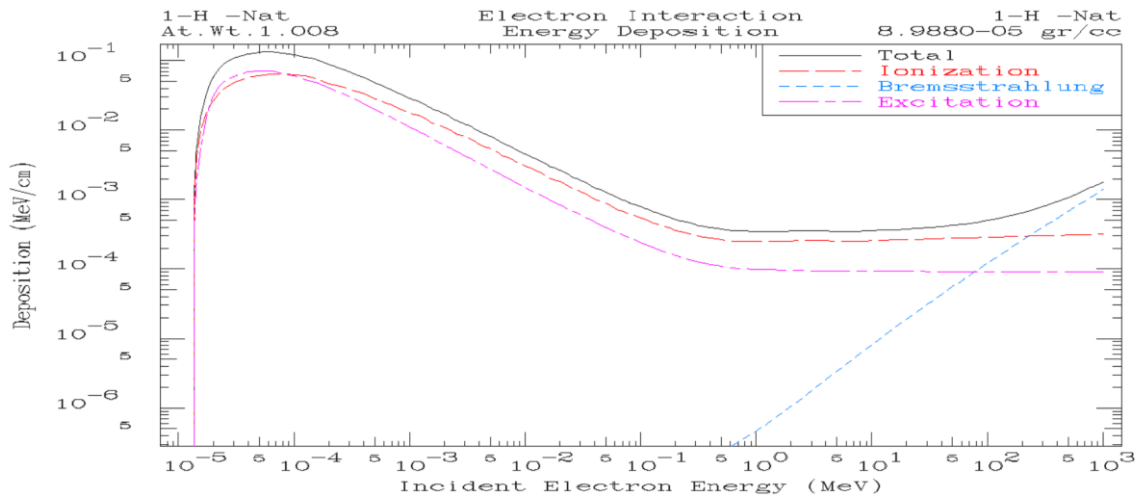


Figure 3 - 11. Stopping power of H calculated by EPICSHOW corresponding to EEDL2017 data.

#### 4.2.2. Collision stopping power

As explained in section 3.3, the *ComputeDEDXPerVolume()* method calculates the *restricted* collision stopping power induced by both ionisation and excitation. To obtain the total collision stopping power,  $T_{cut}$  should be larger than the highest transferred energy. In our comparison, the energy of incident electron ranges from  $E=10$  eV-1 GeV. So in this case,  $T_{max} = 0.5E = 0.5$  GeV. We took  $T_{cut}=10$  GeV, but we have checked that the results, as expected, keep unchanged if we took values of  $T_{cut}$  above 0.5 GeV. Figure 3 - 12 shows the comparison between the stopping power obtained from EEDL2017 (EPICSHOW) and from the existing Livermore model, based on EEDL91. The relative differences observed are generally within a few percent. As the collision stopping power is the sum of excitation and ionisation, it is important to study separately the contribution of each process.

4. Comparison of ionisation cross-section and stopping power between Livermore model and EEDL2017

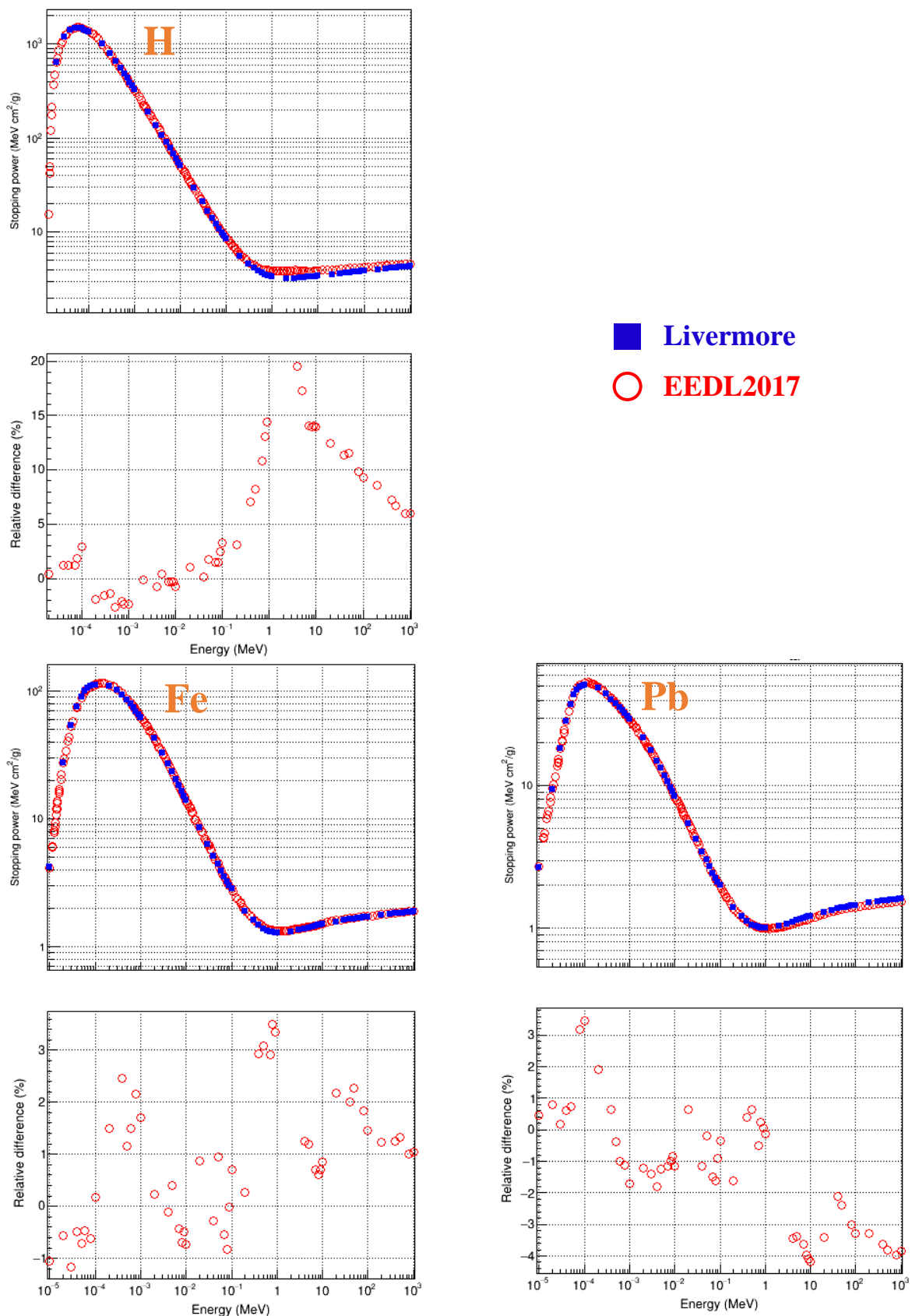


Figure 3 - 12. Collision stopping power (ionisation+excitation) calculated from the existing Livermore model and EEDL2017 for H, Fe and Pb. The relative difference is calculated according to equation (3-5). The energy scale is the same for both cross-sections and RD.

### 4.2.3. Excitation stopping power

As explained in section 3.3, the restricted ionisation stopping power is calculated according to equation (3-4). By setting  $T_{cut}=0.1$  eV, the contribution to the energy loss induced by ionisation becomes 0. In this case, the stopping power obtained by *ComputeDEDXPerVolume()* method is the energy loss solely due to excitation. The comparison between the excitation stopping power obtained from EEDL2017 (EPICSHOW) and from the existing Livermore model, based on EEDL91 is shown in Figure 3 - 13. The results are remarkably close, which is expected, because the excitation cross-sections in EEDL2017 are very similar to EEDL91, as shown in section 2.5.

4. Comparison of ionisation cross-section and stopping power between Livermore model and EEDL2017

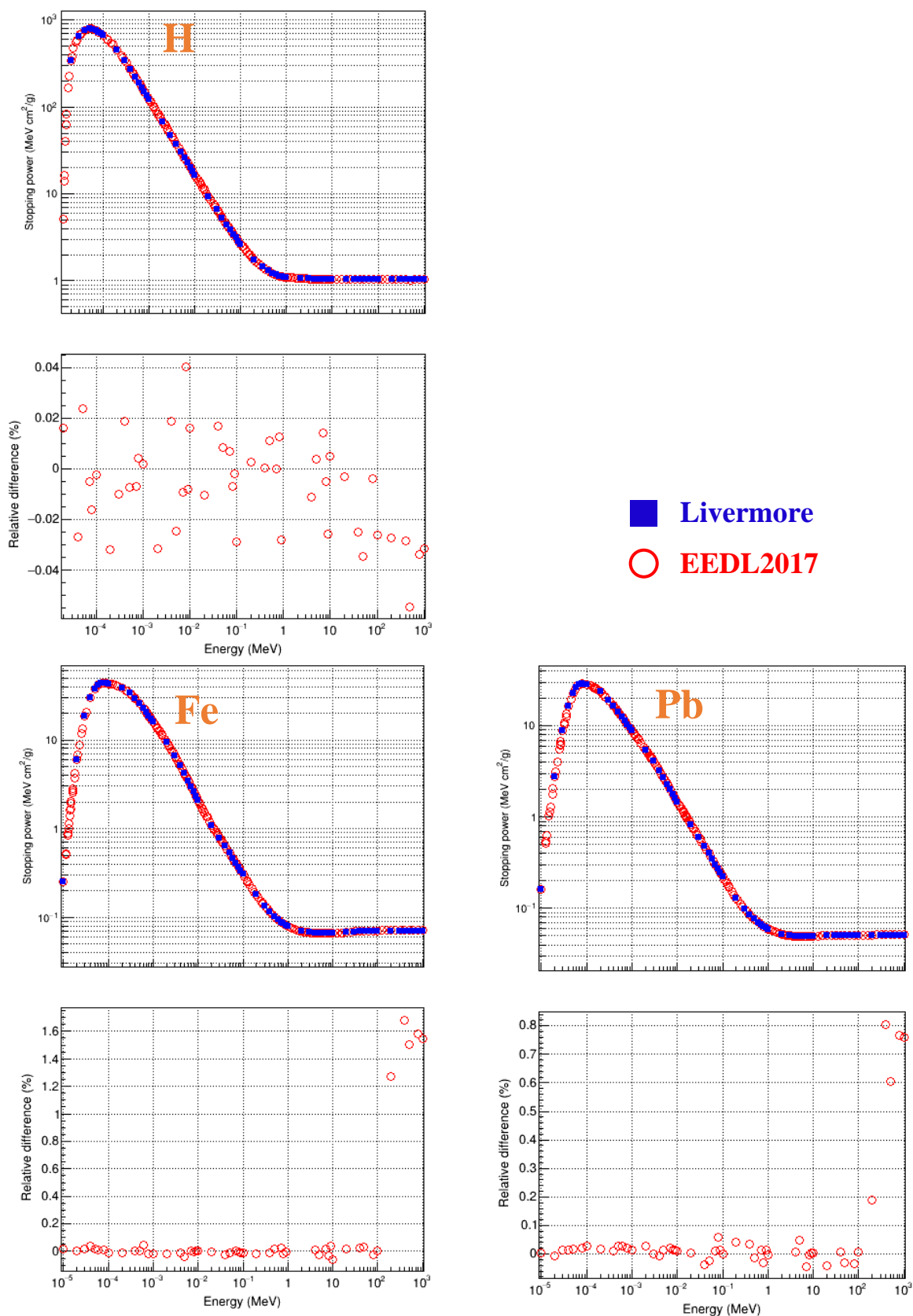


Figure 3 - 13. Excitation stopping power calculated from the existing Livermore model and EEDL2017 for H, Fe and Pb. The relative difference is calculated according to equation (3-5). The energy scale is the same for both cross-sections and RD.

#### 4.2.4. Ionisation stopping power

As explained above, we have obtained by using the *ComputeDEDXPerVolume()* method:

- The collision stopping power  $SP_{\text{Collision}}$  with  $T_{\text{cut}} = 10$  GeV (section 4.2.2);
- The excitation stopping power  $SP_{\text{Excitation}}$ , which is retrieved with  $T_{\text{cut}} = 0.1$  eV in order to exclude the contribution of energy loss due to ionisation (section 4.2.3).

So, the stopping power solely due to ionisation is then calculated as follows:

$$SP_{\text{Ionisation}} = SP_{\text{Collision}} - SP_{\text{Excitation}} \quad (3 - 6)$$

The comparison between the ionisation stopping power obtained from EEDL2017 (EPICSHOW) and from the existing Livermore model, based on EEDL91 is shown in Figure 3 - 14. The results are very similar to the case of collision stopping power, with relative differences within a few percent. This is expected due to two reasons:

- The ionisation plays a dominant role in continuous energy loss.
- The difference of excitation stopping power between Livermore and EEDL2017 is negligible.

We can notice that for H, the relative difference is higher compared to other elements. Actually, a comparison between the stopping power values calculated from the parameterization in Livermore model and those directly obtained from EEDL91 tabulated data shows a similar difference for H. This is described in a technical note<sup>4</sup>. Therefore, the higher relative difference observed in Figure 3 - 14 for H is only the consequence of the parameterization and not due to the update of EEDL2017. To confirm this, we also compared the stopping powers calculated from EEDL2017 and EEDL91. Indeed no significant difference was found. This comparison is also detailed in the technical note mentioned above. Thus, the parameterization for the calculation of stopping power, adopted in the Livermore ionisation model based on EEDL91, does not require a specific update for EEDL2017.

---

<sup>4</sup> The technical note for electrons is available in the Geant4@IN2P3 website of *Documentation* section via <http://geant4.in2p3.fr/styled-4/>.

4. Comparison of ionisation cross-section and stopping power between Livermore model and EEDL2017

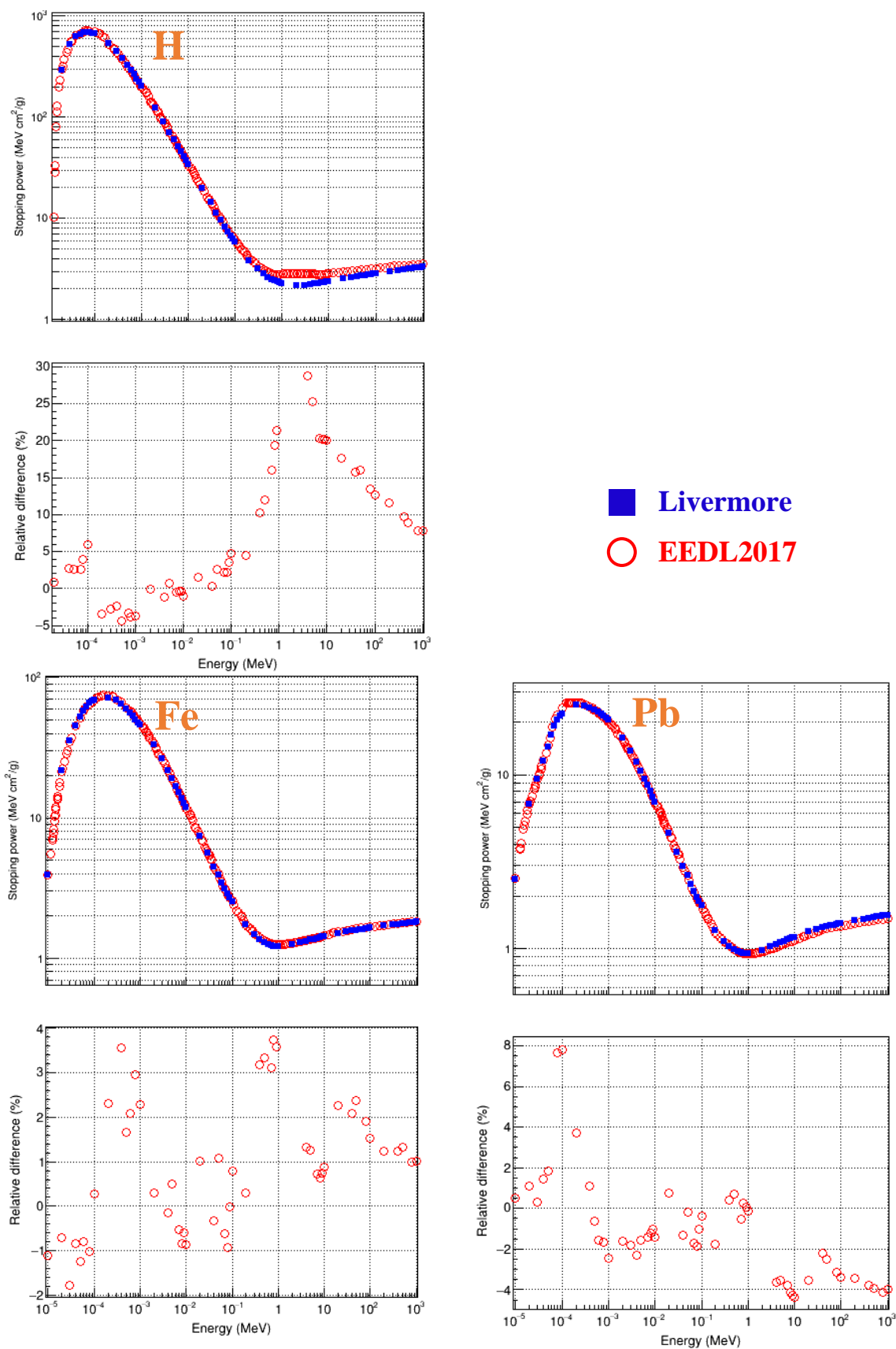


Figure 3 - 14. Ionisation stopping power calculated from the existing Livermore model and EEDL2017 for H, Fe and Pb. The relative difference is calculated according to equation (3-5). The energy scale is the same for both cross-sections and RD.



## 5. Conclusion

In this chapter, we firstly identified the physical quantities modified in EEDL2017 compared to EEDL91, which are related to the Livermore ionisation model: ionisation and excitation cross-sections as well as energy spectra of secondary electrons induced by ionisation. We noted that the physical quantities related to bremsstrahlung are not modified, so the Livermore bremsstrahlung model was not considered in the rest of study. The ionisation and excitation cross-sections exhibit differences only at low energy, due to the modifications of binding energies of outer subshells. As those changes may have an impact on Livermore ionisation model, we compared the calculated cross-sections and stopping powers obtained from the existing Livermore model, based on EEDL91, with those from EEDL2017, in order to determine whether updating the model with EEDL2017 is necessary. The cross-section and stopping power from EEDL2017 were found close to those calculated using the existing Livermore model. This is expected for two reasons:

- The calculation of cross-section and stopping power by the Livermore model is carried out through a parameterization based on EEDL91;
- The update of EEDL2017 compared to EEDL91 is not significant regarding the cross-section and stopping power.

To conclude, the parameterization for the calculation of both cross-section and stopping power, adopted in Livermore ionisation model based on EEDL91, does not require a specific update for EEDL2017. This was expected, quoting Dr Cullen [6]: “*Updating the binding energies is important so that the EPICS2017 data reproduce the well-known characteristic fluorescence X-rays, as shown in Deslattes paper [7], but based on the small shifts in the electron ionization data, shown below, we should not expect much of a change in the transport and slowing down of electrons*”. More information is available in a detailed study that we presented in a technical note in the Geant4@IN2P3 website (<http://geant4.in2p3.fr/styled-4/>).

## References

- [1] Perkins ST, Cullen DE. ENDL type formats for the LLNL Evaluated Atomic Data Library, EADL, for the Evaluated Electron Data Library, EEDL, and for the Evaluated Photon Data Library, EPDL. 1994. <https://doi.org/10.2172/10172308>.
- [2] Cullen DE. A Survey of Atomic Binding Energies for use in EPICS2017. IAEA-NDS-224. 2018. <https://www-nds.iaea.org/publications/nds/iaea-nds-0224/>.
- [3] Apostolakis J, Wright DH, collaboration G. An Overview of the Geant4 Toolkit. AIP Conf Proc. 2007;896(1):1-10. <https://doi.org/10.1063/1.2720452>.
- [4] Apostolakis J, Asai M, Bogdanov AG, Burkhardt H, Cosmo G, Elles S, et al. Geometry and physics of the Geant4 toolkit for high and medium energy applications. Radiat Phys Chem. 2009;78(10):859-73. <https://doi.org/10.1016/j.radphyschem.2009.04.026>.
- [5] Geant4 collaboration. Physics reference manual. 2020;9(0). <https://geant4-userdoc.web.cern.ch/UsersGuides/PhysicsReferenceManual/fo/PhysicsReferenceManual.pdf>.
- [6] Cullen DE. A Survey of Electron Cross Section Data for use in EPICS2017. IAEA-NDS-226. 2017. <https://www-nds.iaea.org/publications/nds/iaea-nds-0226/>.
- [7] Deslattes RD, Kessler EG, Indelicato P, de Billy L, Lindroth E, Anton J. X-ray transition energies: new approach to a comprehensive evaluation. Rev Mod Phys. 2003;75(1):35-99. <https://doi.org/10.1103/RevModPhys.75.35>.



# Chapter 4: Application to proton micro-tomography imaging

---

## 1. Introduction

In this chapter, we first describe the Geant4 application that we developed, called *stim\_pixe\_tomography*, which is dedicated to proton micro-tomography imaging, more precisely for STIM-T and PIXE-T simulations. The process of STIM-T and PIXE-T simulations is similar to experiments, as detailed in section 2. To perform a simulation, it is required to:

- Construct a numerical phantom with defined density and composition;
- Define the beam scan, for example the region of interest, the number of projections, slices, and pixels;
- Specify the proton beam information, such as the energy and number of protons, the positions and directions of the proton beam;
- Collect the simulation result data.

Secondly, we describe in section 3 the simulations that we performed using three numerical phantoms designed for different testing purposes, which will be described in section 3.1:

- A simple cube of uniform density and composition;
- The upper part of a *C. elegans* a worm;
- A typical Inertial Confinement Fusion (ICF) target.

The simulation results are used as input data for tomographic reconstruction codes. The obtained tomographic images are then compared with the original numerical phantom. In this way, we could assess the accuracy of calculated density values and the effectiveness of the NLXP and XA corrections implemented in the reconstruction codes (Figure 4 - 1).

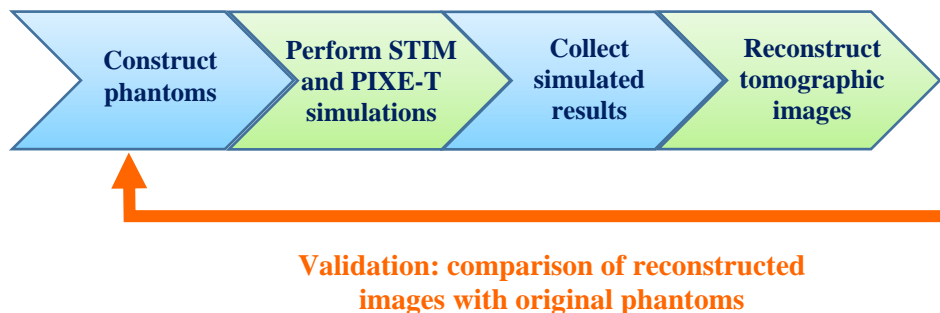


Figure 4 - 1. Schematic diagram of the simulation and validation processes.

In section 4, we give a general description of the reconstruction methods used to obtain the tomographic images. The results are presented and discussed in section 5.

## 2. Design of the *stim\_pixe\_tomography* application

### 2.1. Principle of proton micro-tomography

The principle of proton or more generally, ion, micro-tomography is similar to medical imaging. In the case of proton tomography, the object of interest is rotated relative to the proton beam and the detector. This is illustrated in Figure 4 - 2 (a) and (c), using an example object consisting of a rectangular prism and a cylinder. The beam is moved point by point to scan the area of interest. In this way, we obtain a two-dimensional projection of the object (Figure 4 - 2 (b), projection angle is  $0^\circ$ ). Once the scan is complete, the object is rotated by a certain angle, and the scan is performed again. For example, Figure 4 - 2 (d) shows a projection obtained at  $90^\circ$ . Based on all the projections, we can obtain a 3D image. This 3D image is actually composed of the superposition of tomographic slices reconstructed using a tomographic algorithm. Each slice can be extracted and analyzed separately, for example, Figure 4 - 2 (e) shows one of the tomographic slices.

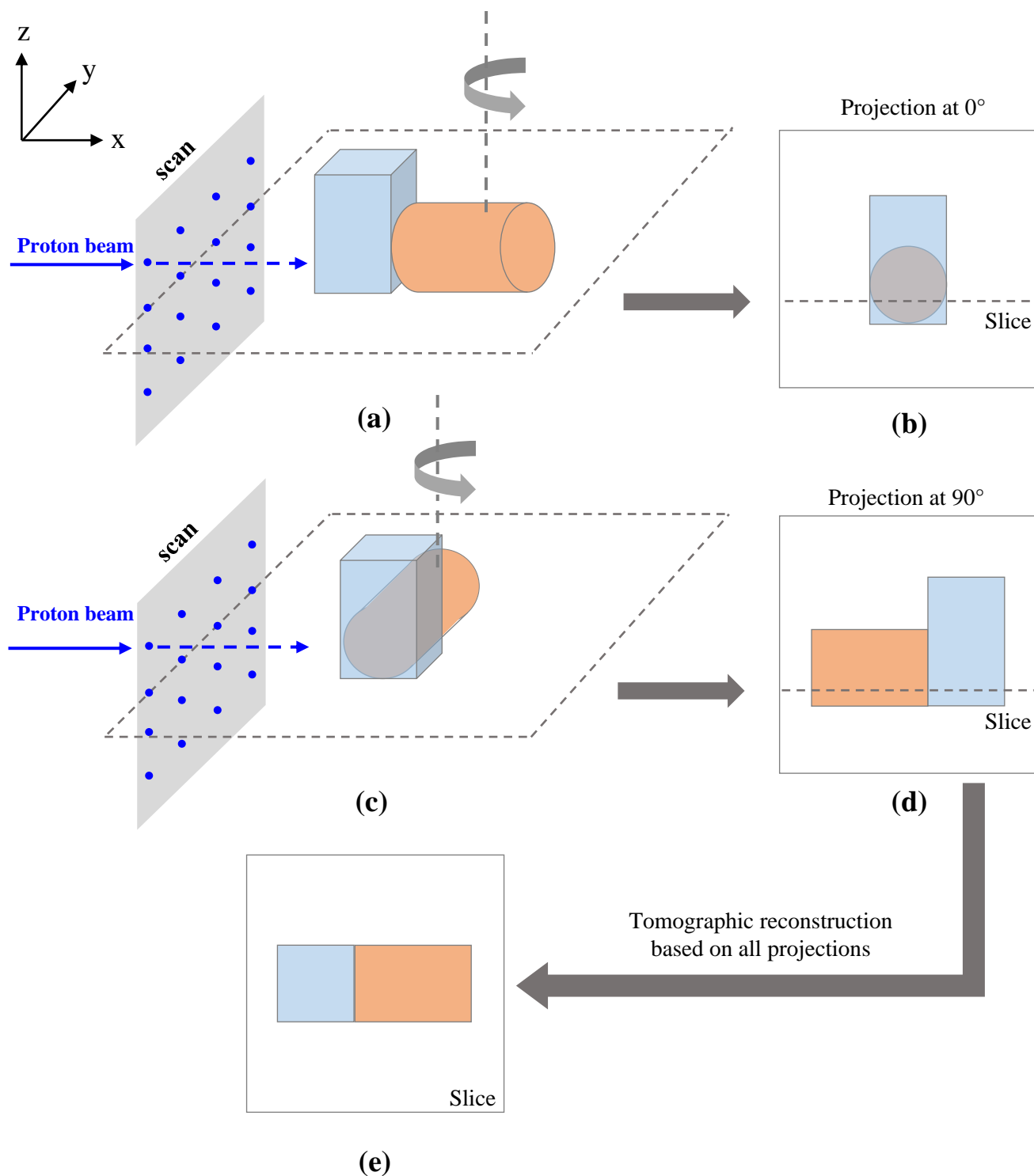


Figure 4 - 2. Principle of proton micro-tomography: schematic views for the projection at  $0^\circ$  (b) and at  $90^\circ$  (d). The blue points in (a) and (c) indicate the successive positions of the proton beam source. The plane with dotted line indicates the tomographic slice displayed in (e).

## 2.2. Principle of STIM-T and PIXE-T experiments

The purpose of the *stim\_pixe\_tomography* application is to simulate STIM-T and PIXE-T experiments. STIM-T aims to determine the distribution of the mass density (in  $\text{g}/\text{cm}^3$ ) of the analyzed sample, which is a microscopic object, a few tens or hundreds micrometers in size. PIXE-T reveals the spatial distribution of chemical elements (in  $\text{g}/\text{cm}^3$  or  $\mu\text{g}/\text{g}$  if normalized with STIM-T) within the analyzed volume. In the experiments, a proton beam of a few MeV scans the area of interest of the sample. As explained in section 2.1, when the scan is finished, the sample rotates to the next projection and the beam scan is performed again. In STIM-T experiments, the detector is placed in front of the proton source ( $0^\circ$  in Figure 4 - 3 (a)). The remaining energy of protons after passing through the sample is measured at each position. This energy is directly related to the thickness of the material for a given projection (Figure 4 - 4) and can be converted to the areal density in  $\text{g}/\text{cm}^2$ . Considering all the projections for the analyzed volume, the distribution of mass density ( $\text{g}/\text{cm}^3$ ) is calculated using a tomographic reconstruction algorithm.

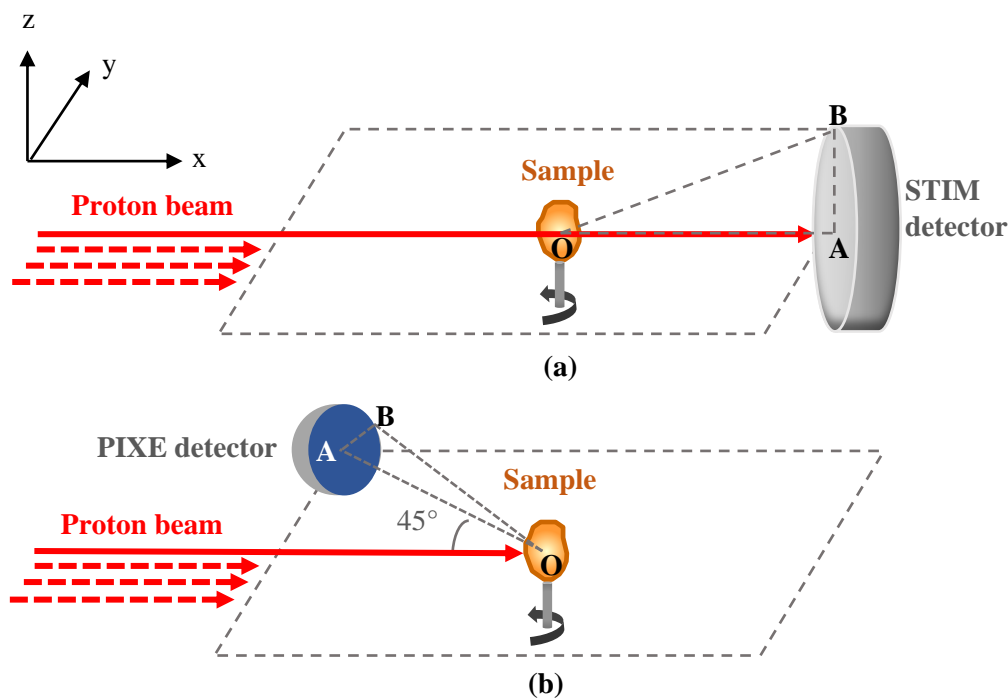


Figure 4 - 3. Experimental set-up for STIM-T (a) and PIXE-T (b).

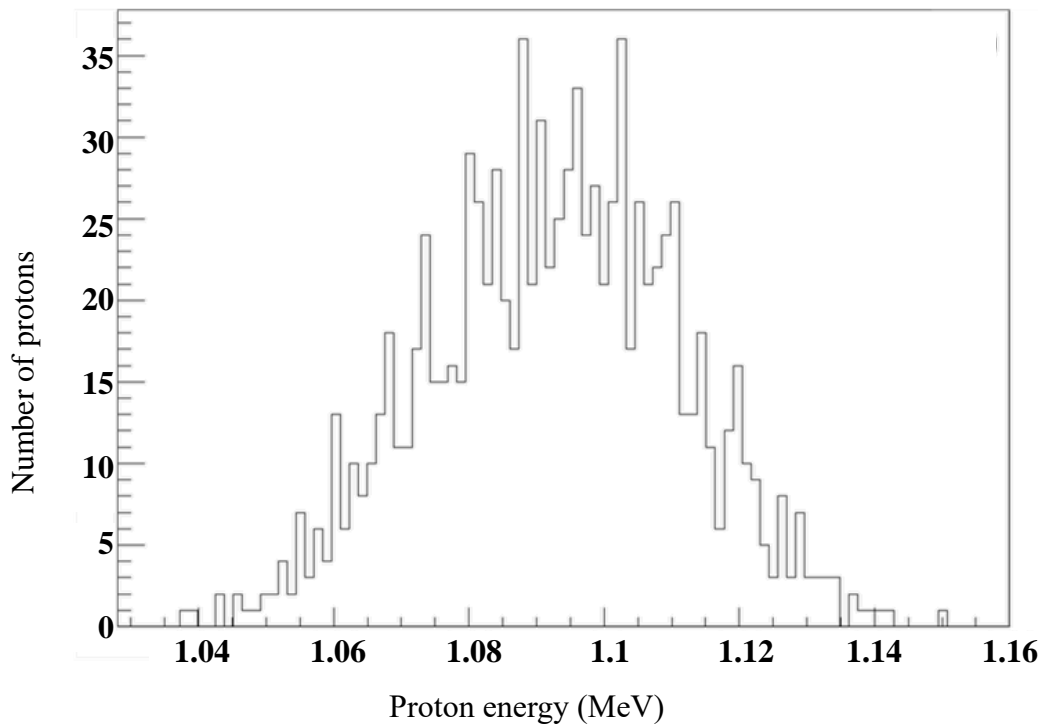


Figure 4 - 4. Example of a proton spectrum for a given position of the proton beam, obtained from a Geant4 STIM-T simulation on *C. elegans* phantom. The energy of incident protons is 1.5 MeV.

PIXE-T consists in detecting the energy of the X-rays emitted by the atoms following the ionisation by the incident protons (Figure 4 - 5). Since the emission of X-rays is isotropic, the detector could be in principle placed at any angle around the sample. In practice, the detector is usually placed at a backward angle, *e.g.*,  $135^\circ$  relative to the proton direction (Figure 4 - 3 (b)). The X-ray energies are characteristic for the respective elements (Figure 4 - 6), and the number of analyzed X-rays depends on the element content, more precisely, the areal density ( $\text{g}/\text{cm}^2$ ). Based on the areal density, the tomographic algorithm determines the distribution of these elemental mass density ( $\text{g}/\text{cm}^3$ ).

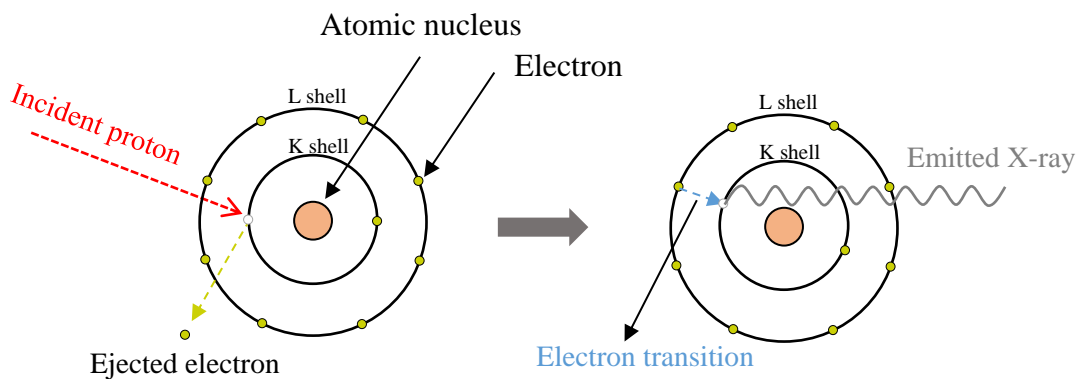


Figure 4 - 5. Principle of PIXE (Particle Induced X-ray Emission). The X-rays arise from the filling of inner-shell vacancies produced by the incident protons.



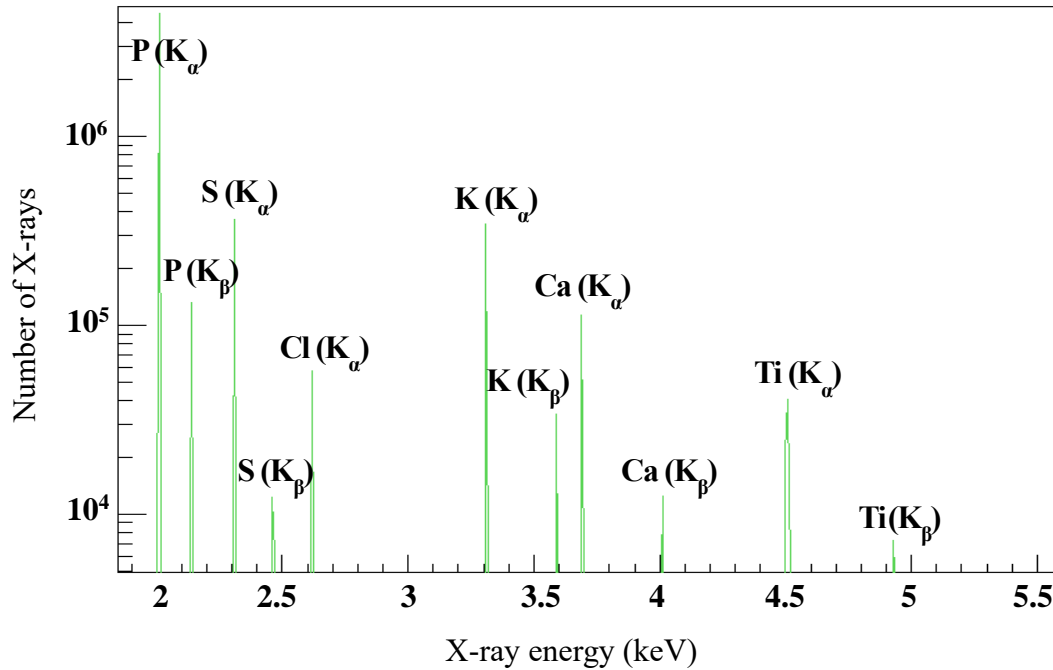


Figure 4 - 6. Example of an X-ray spectrum for a given position of the proton beam, obtained from a Geant4 PIXE-T simulation on *C. elegans* phantom. The chemical elements (P, S, Cl, K, Ca, Ti) are identified from the energy of the X-ray lines in the spectrum.

## 2.3. Description of STIM-T and PIXE-T simulations

### 2.3.1. General procedure: from simulation to image reconstruction

The development of *stim\_pixe\_tomography* is based on the *TestEm5* example, dedicated to studying the interaction of particles going through a single layer of uniform material. The *stim\_pixe\_tomography* is developed for 3D imaging purpose, more precisely for STIM-T and PIXE-T simulations. The simulation results are written into a binary file and then used for the image reconstruction.

To make a simulation, the following steps should be performed (Figure 4 - 7):

- Construction of numerical phantom: the phantoms used in our study will be described in section 3.1;
- Definition of the scan: consists in parameterizing the beam information, *e.g.*, the energy and number of protons, the proton beam positions and directions (sections 2.3.2 - 2.3.4);
- Collection of simulated data: transmitted protons are collected for STIM-T simulation, and emitted X-rays for PIXE-T (section 2.3.5);
- Selection of simulated data (section 2.4).

This last step answers a special need for PIXE-T simulations. One of our objectives is to verify whether the corrections of X-ray attenuation implemented in reconstruction process are accurate. As these corrections depend on the position and the solid angle of the detector, our tests require the collection of X-rays in different detection configurations. Due to the low concentrations of elements of interest in

biological samples and low X-ray production cross-sections, the duration of a PIXE-T simulation can be of the order of several weeks. For this reason, it would not be realistic to repeat it every time we change the position or solid angle of the detector. Thus, instead of including directly the detection process by a detector in the simulation, we chose to model it *after* the simulation. More precisely, during the simulation the particles of interest are collected in all directions ( $4\pi$  solid angle). After finishing the simulation, the detection process is modelled by making a selection of simulation output data considering the geometry of detection. This part will be detailed in section 2.4.

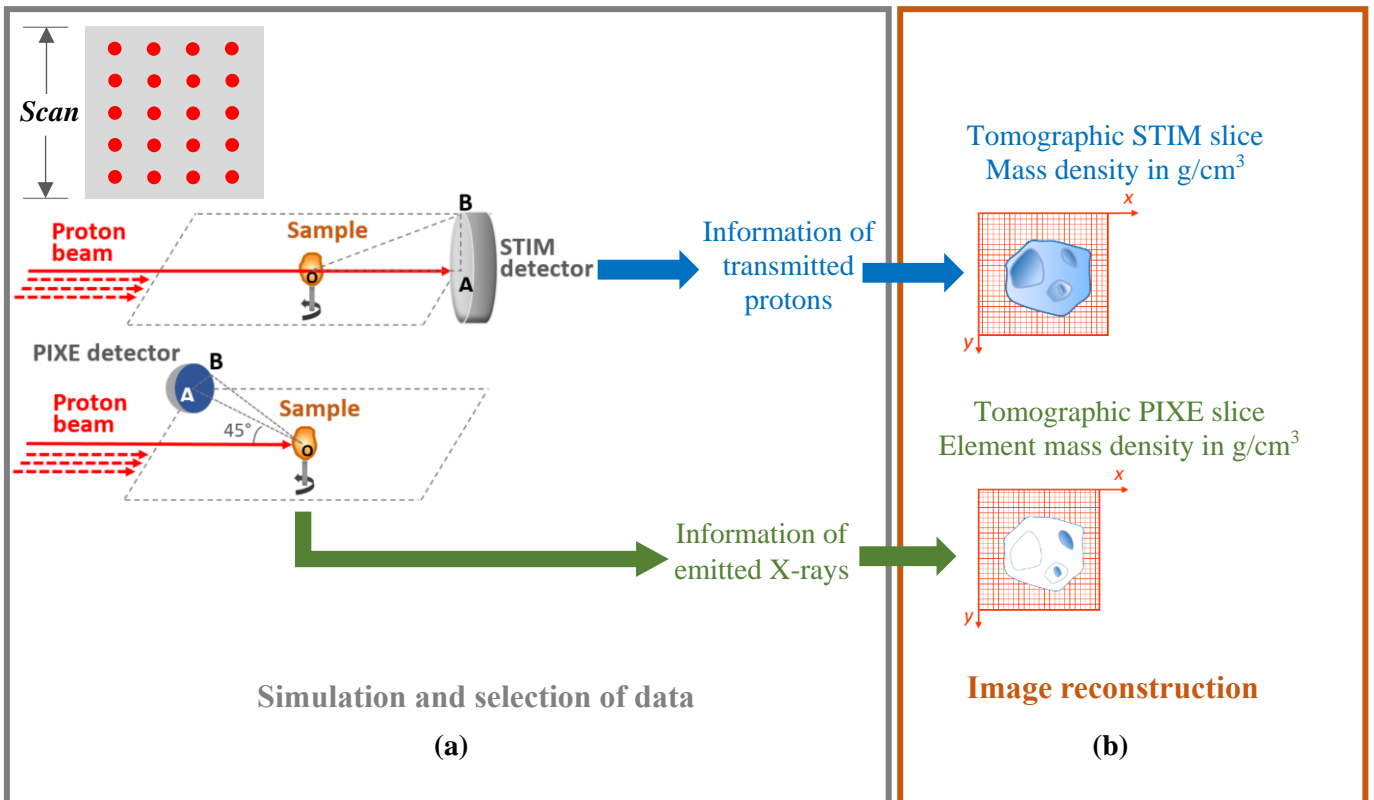


Figure 4 - 7. General procedure: from simulation to image reconstruction. A scan along a single horizontal line (a) results in one horizontal reconstructed tomographic slice (b).

### 2.3.2. Beam positions and directions at first projection

Figure 4 - 8 shows the layout of a STIM-T or PIXE-T simulation at first projection, *i.e.*, projection index = 0 corresponding to projection angle =  $0^\circ$  relative to the proton beam direction. The object is here represented by a sphere in the middle. The scan is shown as a green cube surrounding the object. The red points represent the positions of the beam scanning the sample, which are indexed relatively to the YZ coordinate system. It should be pointed out that in the simulation, contrary to experiments, the object is fixed, and the beam is moving and rotating by simply changing its position and direction, because the proton beam positions and directions are easier to be operated. At the first projection, the beam is directed along the positive x-axis. The tomographic slices are horizontal (in x-y

plane). The Y index indicates the position of the beam within the horizontal slice. The Z index indicates the position of the slice vertically.

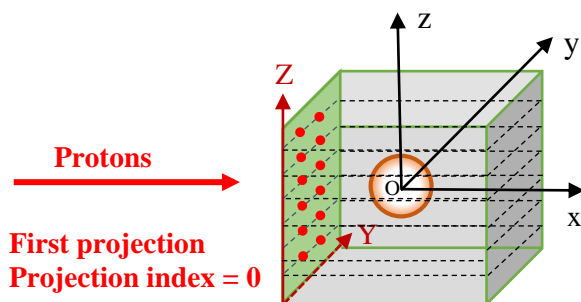


Figure 4 - 8. Layout of a STIM-T or PIXE-T simulation at first projection (projection index = 0).

Figure 4 - 9 shows an example of the successive positions of the source. This example assumes: number of pixels = 10 (horizontal scan), number of slices = 10 (vertical scan). The scan starts from the position index (Y=0, Z=0). The beam source horizontally moves from Y = 0 to 9. Then it switches to the next slice, until the last position (Y=9, Z=9). The number of pixels in the Y direction defines the final number of voxels in the reconstructed tomographic slice. Here, there are  $10 \times 10$  voxels for each reconstructed slice.

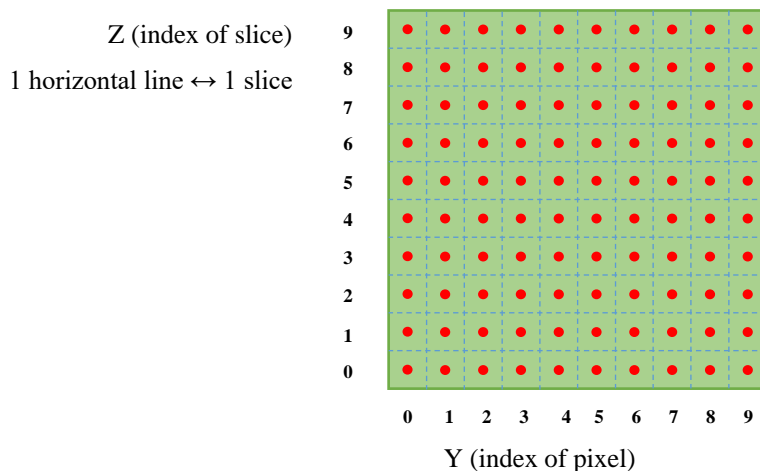


Figure 4 - 9. Positions of the beam for a scan composed of 10 slices of 10 pixels.

### 2.3.3. Rotation of the source

When the beam finishes the scan at the first projection, the beam rotates through a certain angle (step angle) counterclockwise. The scan described in section 2.3.2 is then repeated at this projection. Then the beam rotates again and the scan is performed again, and so on until the last projection. Figure 4 - 10 shows the rotation for projection i.

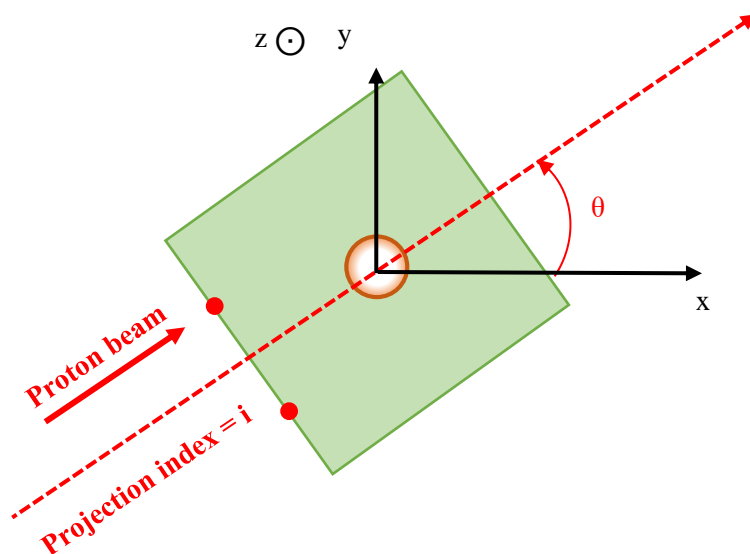


Figure 4 - 10. Rotation of the beam at projection index =  $i$ .  $\theta$  is the rotation angle of the beam at projection  $i$  with respect to the beam direction at first projection.

### 2.3.4. Parameterization of the scan

#### a) Scan parameters

The determination of scan parameters consists in calculating the beam positions and directions according to the scan size and projection angle. A tomography simulation usually involves  $\sim 10^6$  beam positions (e.g., 100 projections  $\times$  128 slices  $\times$  128 pixels =  $1.6384 \times 10^6$  positions), so it is important to automate the parameterization process. This is done via a C script *GPSPointLoop.C*, which generates automatically a macro file containing all necessary parameters to run a simulation, by using the following variables:

- **NumberOfProjections**: number of projections, for example 100;
- **NumberOfPixels**: number of pixels of the scan in horizontal direction, for example 128;
- **NumberOfSlices**: number of slices, usually 1 for PIXE-T and 128 for STIM-T;
- **TotalAngleSpan**: angle span for projections, in degrees, for example if **TotalAngleSpan** = 180 and **NumberOfProjections** = 100, in this case, the angle step is  $1.8^\circ$ , the first projection is at  $0^\circ$ , the last is at  $178.2^\circ$ ;
- **ScanSize**: total length of the scan in horizontal direction, in  $\mu\text{m}$ ; this value should be large enough to ensure that the phantom is contained within the scan at any angles/projections.  
The pixel width is equal to  $\text{ScanSize}/\text{NumberOfPixels}$ ;
- **ScanHeight**: total length of the scan in vertical direction, in  $\mu\text{m}$ .  
The pixel height is equal to  $\text{ScanHeight}/\text{NumberOfSlices}$ ;
- **NbParticles**: number of protons at each position of the beam source;

- **energy**: energy of the proton beam, in MeV;
- **typeParticle**: type of the particle, for example “proton”.

The beam positions and directions at different angles/projections are calculated according to their positions at the first projection (0°) and the rotation angle. The calculation is presented as follows.

**b) Calculation of beam positions**

We consider (Oxyz) a fix coordinate system, attached to the object, whereas the beam scan rotates from one projection to another. We consider a particular position of the beam source at position index j within the scan. At the first projection (angle 0), this position corresponds to P (x<sub>j</sub>, y<sub>j</sub>) (Figure 4 - 11), with:

$$\begin{cases} x_j = r \cos a \\ y_j = r \sin a \end{cases} \quad (4 - 1)$$

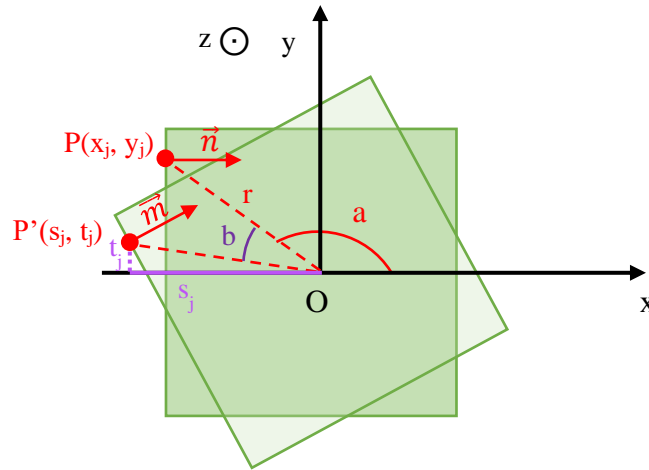


Figure 4 - 11. Rotation of a beam position from the first projection to projection i.

We consider projection i, for which the scan beam has rotated through an angle *b*. In this case, P(x<sub>j</sub>, y<sub>j</sub>) rotates to P'(s<sub>j</sub>, t<sub>j</sub>), with s<sub>j</sub> and t<sub>j</sub> mathematically defined as:

- s<sub>j</sub> is the orthogonal projection of P' on the x axis;
- t<sub>j</sub> is the orthogonal projection of P' on the y axis.

Thus:

$$\begin{cases} s_j = r \cos(a + b) = r \cos a \cos b - r \sin a \sin b \\ t_j = r \sin(a + b) = r \sin a \cos b + r \cos a \sin b \end{cases} \quad (4 - 2)$$

Substituting equation (4-1) into equation (4-2), we obtain:

$$\begin{cases} s_j = x_j \cos b - y_j \sin b \\ t_j = x_j \sin b + y_j \cos b \end{cases} \quad (4 - 3)$$

In this way, we obtain the position<sup>5</sup> of the beam source at projection i.

<sup>5</sup> Equation (4-3) can be obtained directly by considering that P' coordinates are the product of the rotation matrix of angle *b* by P coordinates.

### c) Calculation of beam directions

We consider  $\vec{n}$ , the beam direction at the first projection as represented in Figure 4 - 11 at the position  $P(x_j, y_j)$ . At this projection, the beam is directed along the positive x-axis. The directions used in Geant4 are direction cosines, so  $\vec{n} = (1, 0, 0)$ .

$\vec{n}$  rotates through an angle  $b$  to  $\vec{m}$  at projection  $i$ .

So, at projection  $i$ , the direction of the beam is given by  $\vec{m} = (m_x, m_y, m_z)$ , as represented in Figure 4 - 11 at the position  $P'(s_j, t_j)$ .

Thus:

$$\begin{cases} m_x = \cos b \\ m_y = \sin b \\ m_z = 0 \end{cases} \quad (4 - 4)$$

In this way, we obtain the direction of the beam source at projection  $i$ .

### **2.3.5. Collection of simulated data**

The reconstruction of tomographic images requires to collect the following information:

- The energy of particles of interest, *i.e.*, transmitted protons for STIM-T and emitted X-rays for PIXE-T;
- The projection index;
- The position of the proton beam, *i.e.*, the indices of the slice and the pixel for each collected particle of interest.

In addition, we need to determine whether the particle enters the detector after the simulation. For this, we should make a geometrical selection of particles, which requires knowing their position and/or momentum, this will be detailed in section 2.4. As mentioned in section 2.3.4, a tomography simulation usually involves  $\sim 10^6$  beam positions (*e.g.*, 100 projections  $\times$  128 slices  $\times$  128 pixels), and many events to collect. Thus, to address the problem of large data, we have tried different approaches. A common format for data analysis is recommended in Geant4 is ROOT (<https://root.cern.ch/>). So we first tried to save the simulation results as ROOT ntuples. However, in this case, it was required to create one ntuple for each position of the beam and to assemble them after the simulation was completed. We decided not to follow this cumbersome process and take a simpler way. Instead of using ROOT file format, we choose to save the data in a custom binary file in append mode. For this, we designed two custom *struct* variable types to store the information of collected particles in a compact way.

The first *struct* is called *ParticleInfo*. It stores the following information:

- Energy of the collected particle;
- Position and/or momentum of the collected particle.

The information of position and/or momentum of the collected particle is related to the way we determine whether the particle is detected, which will be described in section 2.4.

The second *struct* is called *RunInfo*. It stores the following information:

- Number of collected particles at a given beam position;
- Indices of the projection, slice and pixel at a given beam position.

In this way, the output binary file is about a few megabytes per projection.

In fact, it is worth mentioning that using ROOT file format has an advantage regarding multithreading: the ntuples produced on thread workers are progressively and automatically merged to the main ntuples on the master. However, in our case, to write all the information in one binary file, we merge the data produced thread workers with a specific procedure defined in the *Run::Merge()* method.

Another advantage of the binary file being written in append mode is that we can resume the simulation if any interruption happens during a simulation. Indeed, remedial measures are considered in case of interruptions, for example power failure. A specific C script was developed to identify where the interruption occurred in order to resume the simulation without need to restart it from the beginning.

The collection of particle information (energy, momentum and/or position) occurs at different stages of the particle trajectory, as shown in Figure 4 - 12. For STIM-T, the information of transmitted protons is collected after the protons get out of the phantom at the end of the particle track, *i.e.*, at exit. The collection is implemented in the *stim\_pixe\_tomography* application via the *TrackingAction::PostUserTrackingAction()* method. For PIXE-T, we collect not only the information of X-rays at exit point, but also at creation point thanks to the flexibility of Geant4, as described in section 2.3.6.

### 2.3.6. PIXE-T simulation under non-standard conditions

One of the objectives using Geant4 simulation is to evaluate the accuracy of the X-ray count attenuation corrections (NLXP and XA<sup>6</sup>) implemented in the image reconstruction process. For this, we performed PIXE-T simulations under standard conditions similar to experiments, as explained in the previous sections. In this case, we collected the information of X-rays after getting out of the phantom at the end of the particle track, *i.e.*, at exit as indicated in Figure 4 - 12. In order to study independently the effects of NLXP and XA corrections, we took advantage of the flexibility of Geant4, to perform simulations under non-standard conditions, which are impossible to realize in experiments:

- Geant4 allows us to collect X-rays in the object, at the position where they are emitted, *i.e.*, at the creation point. In this case, the XA effect is excluded;
- Geant4 allows us to artificially turn off the process of proton energy loss. In this way, the proton energy is kept at the initial energy along its track in the material. Therefore, the NLXP effect is excluded.

---

<sup>6</sup> See section 4.2 of chapter 1.

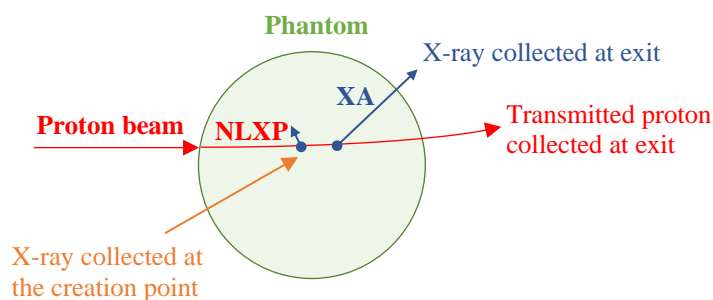


Figure 4 - 12. Presentation of different stages of the particle trajectory, where the collection of data is implemented: Transmitted proton at exit after getting out of the phantom, X-ray at exit after getting out of the phantom, X-ray at the creation point where it is generated.

In summary, we can make PIXE-T simulations under standard and non-standard conditions for each phantom and obtain four types of X-ray information:

- **Case 1:** X-rays collected at the creation point and the proton energy loss process is turned-off. In this case, NLXP and XA effects are both excluded;
- **Case 2:** X-rays collected at the exit of the object and the proton energy loss process is turned-off. In this case, only the NLXP effect is excluded;
- **Case 3:** X-rays collected at the creation point but the proton energy loss process is not turned-off. In this case, only the XA effect is excluded;
- **Case 4:** X-rays collected at the exit of the object and the proton energy loss process is not turned-off. In this case, both NLXP and XA corrections are required.

The collection of X-rays at the creation point and at exit are implemented in the code of the *stim\_pixe\_tomography* application via the *StackingAction::ClassifyNewTrack()* and *TrackingAction::PostUserTrackingAction()* methods respectively.

Turning off the proton energy loss process exceptionally requires modifying the source code of Geant4, because we need to re-set the proton energy at its initial value after each interaction step. More precisely, the method *G4Step::UpdateTrack* of the Geant4 source code *G4Step.icc* is modified, as shown in Appendix B, Figure B - 1.

### 2.3.7. Format of simulation output files

For STIM-T simulation, the output binary file is called *ProtonAtExit.dat*, in which the information of transmitted protons for all beam positions is saved. For PIXE-T, two binary files *GammaAtCreation.dat* and *GammaAtExit.dat* are generated at the end of the simulation, storing the information of X-rays at the creation point and at exit for all beam positions. For each beam position, the indices of projection, slice, and pixel as well as the number of particles are written in the format of the *RunInfo* struct in the



output file. Then, the energy, position and/or momentum of the collected particles are listed in a vector containing a series of *ParticleInfo* struct (Figure 4 - 13).

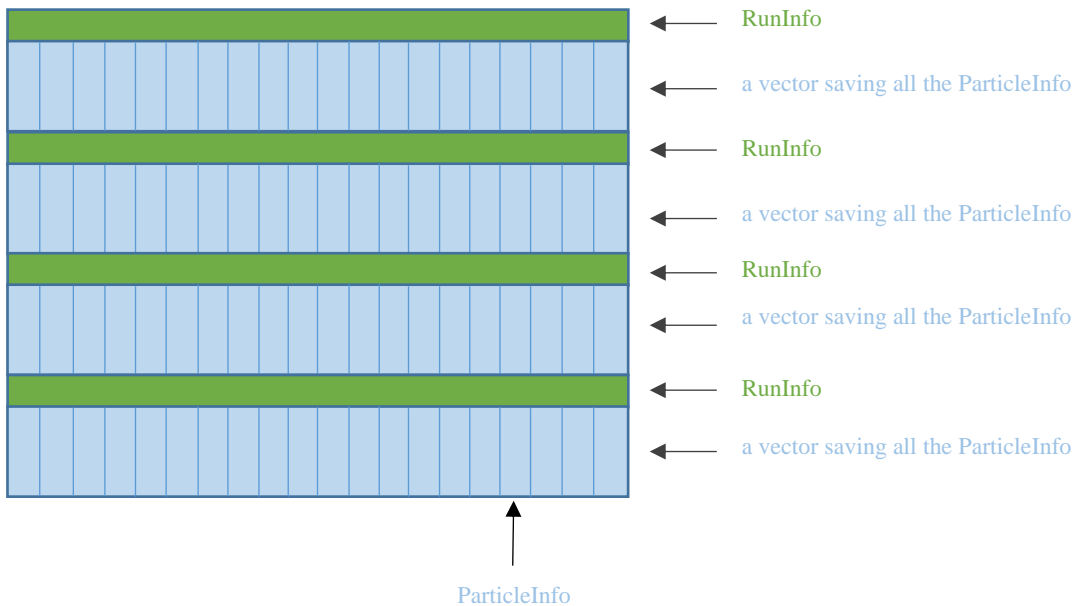


Figure 4 - 13. Structure of the output file for a STIM-T or PIXE-T simulation.

## 2.4. Selection of simulated data

### 2.4.1. Principle and assumptions

As explained in section 2.3.1, the selection of the particles entering the detector is performed *after* the simulation, in order to easily modify the position and/or solid angle of the detector without having to run a simulation again. The principle of the selection is based on the position of the detector according to the sample and the beam. It also depends on the shape and size of the entrance window, which is assumed circular in our case. In fact, we provide two methods of selection:

- Selection with particle momentum;
- Selection with particle position and momentum.

By default, the first option, *i.e.*, the selection with particle momentum is proposed. It is based on the assumption that the phantom size is negligible relative to the size and distance of the detector, which is usually the case for micro-tomography. If ever the assumption is not valid, the selection with particle position and momentum gives another option. Of course, this will significantly increase the size of simulated data. Indeed, the method of selection determines the definition of the *struct ParticleInfo*, which stores particle information as explained in section 2.3.5. For the selection using position and momentum, the position of the particle of interest is additionally saved in *ParticleInfo*. More details about the selections will be given in section 2.4.2 - 2.4.4.

The selection is performed by using a C script corresponding to the chosen selection method. After executing the script, the information of selected events is then written into a binary file, which is used

as an input file for tomographic reconstruction. The necessary information of selected events for image reconstruction consists of:

- Energy;
- Indices of the projection, slice and pixel of the current event.

### 2.4.2. Parameters of selection

The selections are performed using the following variables:

- $\alpha$ : angular position of the detector, *i.e.*, angle between the position of the detector and the direction of incident proton beam ( $\widehat{xOA}$  in Figure 4 - 14 for first projection and  $\widehat{x'O'A}$  in Figure 4 - 15);
- $l$ : distance between the scanned object and detector (OA in Figure 4 - 14);
- $r$ : radius of entrance window of the detector (AB in Figure 4 - 14);
- $\theta$ : half apex angle of detection,  $\theta = \widehat{AOB}$  in Figure 4 - 14 and Figure 4 - 15.

Figure 4 - 14 shows the positions of the X-ray detector and the object at first projection 0 for the selection in a PIXE-T simulation. Figure 4 - 15 shows the positions of the detector and the object at projection  $i$ . Whatever the projection is, the angle between the position of the detector and the direction of the incident protons remains fixed.

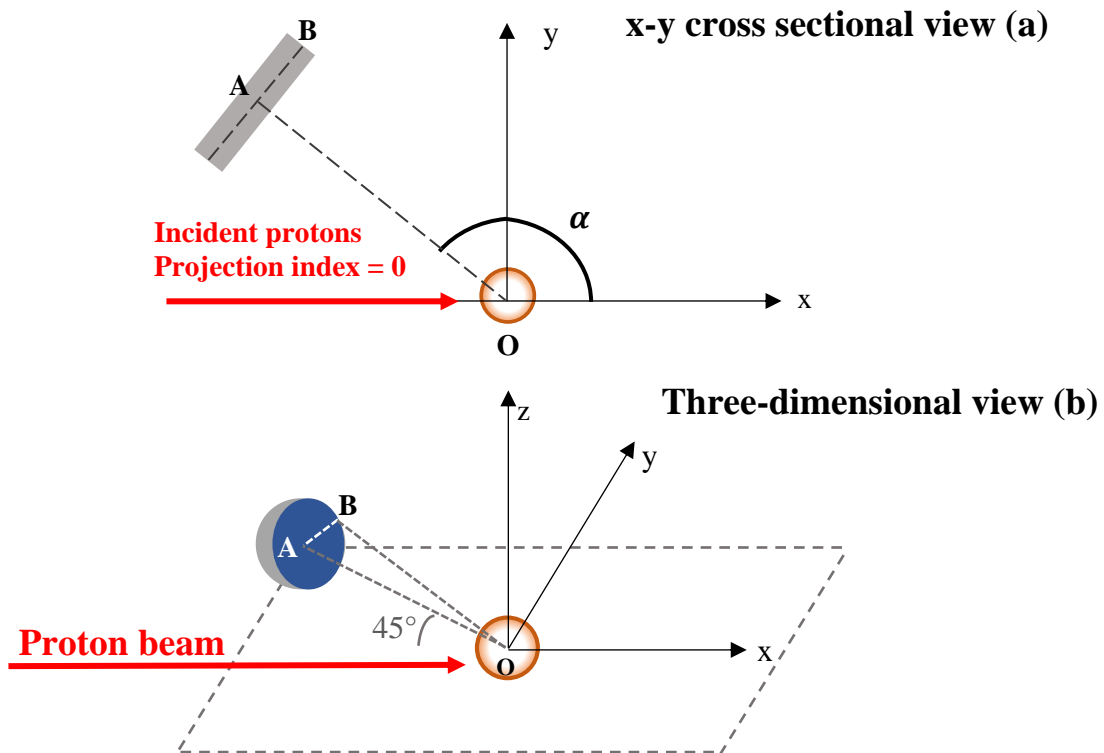


Figure 4 - 14. Schematic position of the detector at the first projection (projection index = 0) in a PIXE-T simulation. The  $\alpha$  angle is here arbitrarily equal to  $135^\circ$ .

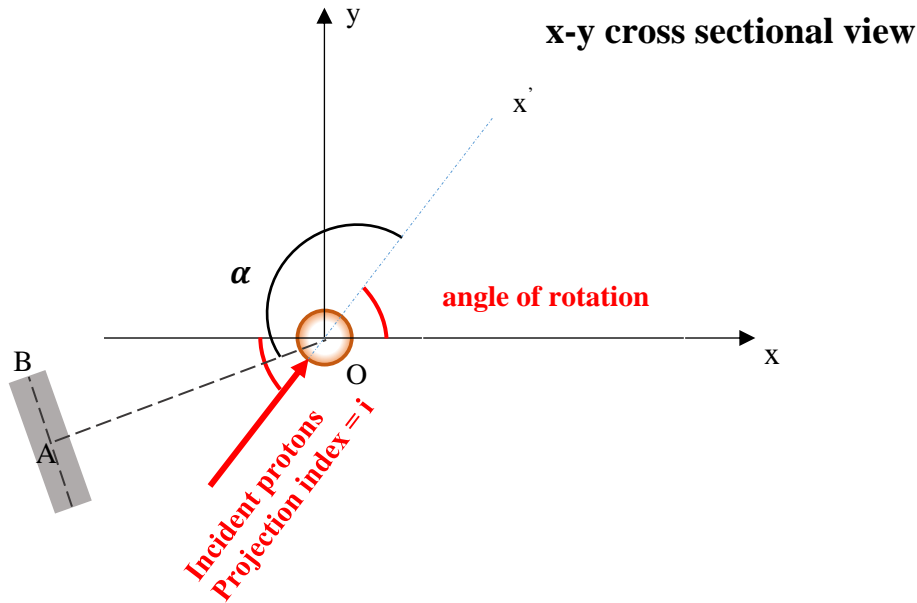


Figure 4 - 15. Schematic position of the detector at projection index =  $i$  in a PIXE-T simulation. The  $\alpha$  angle is here arbitrarily equal to  $135^\circ$ .

### 2.4.3. Selection with particle momentum

The approximate selection using particle momentum is based on the assumption that the phantom size is negligible relative to the size and distance of the detector. In this case, the selection only requires parameterizing the angular position  $\alpha$  of the detector and its half apex angle  $\theta$ . The X-ray is considered “detected” only if the angle between its momentum and  $\overrightarrow{OA}$  (Figure 4 - 14 (b)) is less than the half apex angle  $\theta$  ( $\widehat{AOB}$  in Figure 4 - 14 (b)).  $\theta$  depends on the radius and the distance of the detector:

$$\theta = \text{atan} \frac{r}{l}$$

In our simulations, we always adopted this approximate selection as the assumption is verified.

For STIM-T simulation, we selected the protons using values similar to experimental conditions:

- Angular position of the detector  $\alpha = 0^\circ$ ;
- Half apex angle  $\theta = 10.2^\circ$

For PIXE-T simulation, we selected the X-rays using:

- Angular position of the detector  $\alpha = 135^\circ$ ;
- Half apex angle  $\theta = 70^\circ$

$135^\circ$  is a typical experimental angular position for the detector. However,  $70^\circ$  is not consistent with experimental conditions. Here we chose this very large angle of  $70^\circ$  leading to a solid angle about 4.134 sr, because a large solid angle significantly reduces the PIXE-T simulation time since more events can be collected, so that less incident particles are required. It should be pointed out that such a half apex angle would not be possible in experiments, because the detector would block the oncoming beam.

### 2.4.4. Selection with particle position and momentum

The selection using particle position and momentum is a more precise method that should be used when the assumption of negligible phantom size is not valid. In this case, the selection requires parameterizing the angular position  $\alpha$ , the distance  $l$  and the radius  $r$  of the detector.

To describe this method, we define (Figure 4 - 16):

- Point C ( $x_0, y_0, z_0$ ): the position of the particle when being collected in the simulation, *i.e.*, either at the end of the track or at the point where the particle is generated, according to the user needs.
- $\vec{n}_0$  (a, b, c): the momentum of the particle;
- $\vec{n} = \vec{OA}$ : the vector orthogonal to the detector entrance window;
- Point P( $x_i, y_i, z_i$ ): the intersection point between the trajectory of the particle and the detector entrance window.

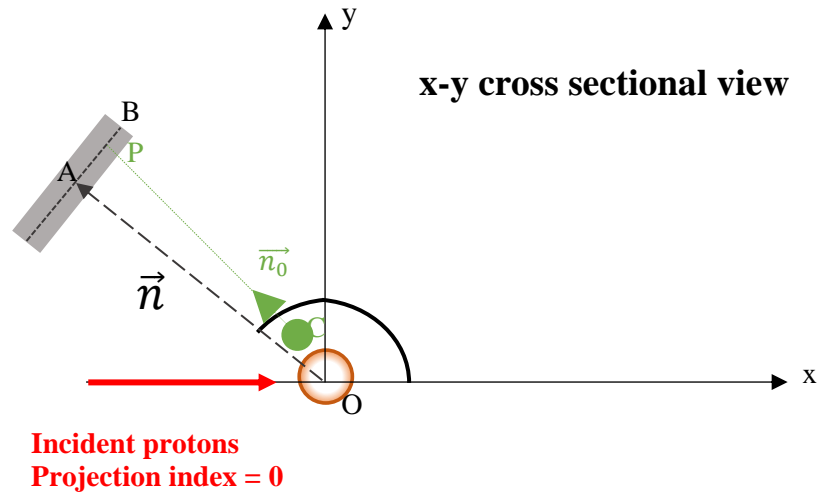


Figure 4 - 16. Detection of particle using precise selection.

According to the angular position of the detector, we have:

$$\vec{n} = (l \cos \alpha, l \sin \alpha, 0)$$

The position of the center point of the entrance window is also given by: A ( $l \cos \alpha, l \sin \alpha, 0$ ).

Knowing the point A and the vector  $\vec{n}$  orthogonal to the detector entrance window, the equation of the plane of the entrance window is established as follows:

$$l \cos \alpha (x - l \cos \alpha) + l \sin \alpha (y - l \sin \alpha) + 0(z - 0) = 0 \quad (4 - 5)$$

Knowing the point C ( $x_0, y_0, z_0$ ) and momentum  $\vec{n}_0$  (a, b, c), the trajectory of the particle is defined as follows:

$$\begin{cases} x = x_0 + at \\ y = y_0 + bt \\ z = z_0 + ct \end{cases} \quad (4 - 6)$$

where  $t$  is a constant.

Substituting equation (4-6) into equation (4-5), we obtain the intersection point P of the trajectory of the particle and the detector plane by calculating  $t$ :

$$t = \frac{(l \cos \alpha - x_0)l \cos \alpha + (l \sin \alpha - y_0)l \sin \alpha}{al \cos \alpha + bl \sin \alpha} = \frac{l^2 - x_0 l \cos \alpha - y_0 l \sin \alpha}{al \cos \alpha + bl \sin \alpha} \quad (4 - 7)$$

The condition  $al \cos \alpha + bl \sin \alpha = 0$  should be excluded, because it means the trajectory is parallel to the detector plane. In this case, the particle is not detected.

Thus, the intersection point P ( $x_i, y_i, z_i$ ) is:

$$\begin{cases} x_i = x_0 + at \\ y_i = y_0 + bt \\ z_i = z_0 + ct \end{cases} \quad (4 - 8)$$

We calculate the distance of point P to the center point of the entrance window point A, *i.e.*,  $PA$ :

$$PA = \sqrt{(l \cos \alpha - x_i)^2 + (l \sin \alpha - y_i)^2 + z_i^2} \quad (4 - 9)$$

The condition that determines if a particle is detected is:  $PA$  is less than the radius of the detector  $r$ .

## 3. Simulations

### 3.1. Numerical phantoms

#### 3.1.1. Cube

A homogeneous cube phantom was used to perform simple tests, for example to test the preservation of geometrical shapes and edges in the reconstructed images [1], and to study the effect of X-ray absorption [2]. For this, the cube phantom was designed with different sizes and compositions according to the needs. For example, two cubes were used:

- Cube 1:  $5 \times 5 \times 5 \mu\text{m}^3$ , as a thin sample, for which the effect of X-ray absorption is negligible;
- Cube 2:  $40 \times 40 \times 40 \mu\text{m}^3$ , as a thick sample, for which the effect of X-ray absorption is not negligible.

The composition of the cubes included phosphorus, because it is the most attenuated element in PIXE analysis for our application (lowest X-ray energy). According to the basic rules of Geant4, the construction of the phantom is implemented in the *DetectorConstruction.cc/hh* codes, particularly, in the *DetectorConstruction::Construct()* method.

#### 3.1.2. *C. elegans*

It is interesting to include *C. elegans* into Geant4 simulation for further use, because *C. elegans* is a widely used model in biology and especially for the research carried-out in the iRiBio team. Thus, we designed for the first time in Geant4 a phantom modelling the upper part of a *C. elegans* worm in our application. It was created using six ellipsoids to represent six specific regions (Figure 4 - 17):

- The cuticle, *i.e.*, the “skin” of the worm;
- The body containing the intestine and two cell nuclei;
- Two cell nuclei;
- The intestine;
- A Ti rich region inside the intestine.

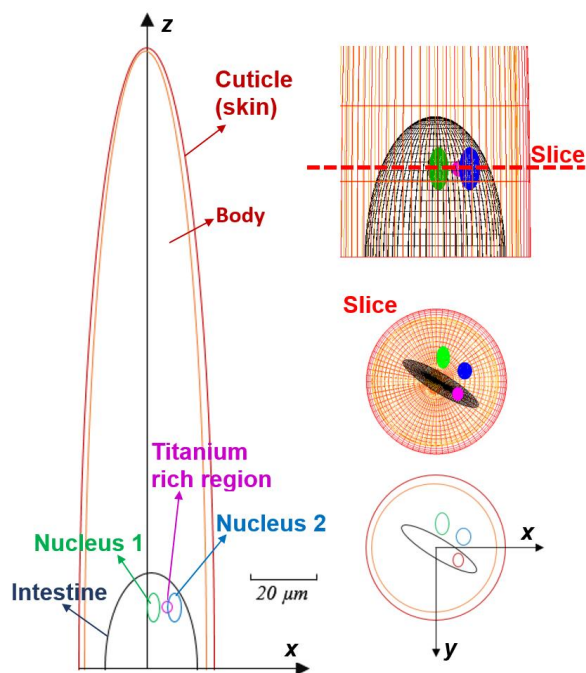


Figure 4 - 17. Schematic view of the *C. elegans* phantom implemented in Geant4, showing the six ellipsoids used to model the different parts of the worm (left and bottom right).

A slice (upper right) containing the cell nuclei and the Ti rich region was selected for PIXE-T simulations, as described in section 3.2.3.

The shape, size, density and element content of the phantom were obtained from STIM-T and PIXE-T experiments from freeze-dried specimens [3, 4]. The construction of the phantom was the main subject of my internship at CENBG/LP2I Bordeaux in 2017 [1]. The geometrical parameters of the ellipsoids are listed in Table 4 - 1.

Table 4 - 1. Geometrical parameters of the six ellipsoids used to model the shape of the *C. elegans* phantom.

Region	Ellipsoid number	Semi-axis in $x$ direction ( $\mu\text{m}$ )	Semi-axis in $y$ direction ( $\mu\text{m}$ )	Semi-axis in $z$ direction ( $\mu\text{m}$ )	Position of the center ( $\mu\text{m}$ )	Rotation around $z$ axis (degree)
Cuticle	1	20.6	21.4	188	(0; 0; 0)	0
Body	2	18.6	19.0	187	(-0.39; 0; 0)	0
Nucleus 1	3	1.95	3.23	4.32	(1.97; -7.09; 18.07)	0
Nucleus 2	4	2.08	2.46	4.32	(8.27; -3.15; 18.07)	0
Intestine	5	3.67	16.5	28.7	(1.25; 0.61; 0)	-59
Ti rich region	6	1.62	1.95	1.62	(6.25; 3.61; 18.07)	0

The composition of the different regions of the phantom is shown in Table 4 - 2 . The element content for P, S, Cl, K and Ti was obtained from PIXE-T experiments, giving the element mass density distribution in  $\text{g}/\text{cm}^3$ . These values were then converted to mass percentage. For this, we used the material mass density derived from STIM-T experiments (last column of Table 4 - 2). The rest of the material was considered as (dry) biological material. Its composition  $\text{C}_{10}\text{H}_{17}\text{O}_3\text{N}_2$  was derived from previous studies of cryofixed and lyophilized biological samples by RBS (Rutherford Backscattering Spectrometry) using classical (not tomographic) 2D ion beam analysis [5]. It should be noted that the complete composition of dehydrated *C. elegans* has not yet been determined experimentally. Although the experimental data may not be very precise, the aim of the study is not to determine the exact composition of *C. elegans*, but only to study the accuracy of the reconstruction process.

*Table 4 - 2. Element content of the six ellipsoids of the C. elegans phantom. The ellipsoids have a uniform mass density and composition (here expressed in percentage by mass, as defined in the Geant4 material composition).*

Region	P	S	Cl	K	Ca	Ti	$\text{C}_{10}\text{H}_{17}\text{O}_3\text{N}_2$	Total mass density ( $\text{mg}/\text{cm}^3$ )
<b>Cuticle</b>	0.47%	0.21%	0.05%	0.48%			98.79%	497
<b>Body</b>	0.72%						99.28%	408
<b>Nucleus 1</b>	0.57%				1.55%		97.88%	663
<b>Nucleus 2</b>	0.61%				1.44%		97.95%	603
<b>Intestine</b>		0.12%	0.02%	0.20%			99.66%	541
<b>Ti rich region</b>		0.10%	0.02%	0.18%		0.05%	99.64%	751

### 3.1.3. ICF target

In the framework of my PhD project, a collaboration with Fudan University on the application of Geant4 to tomographic imaging of inertial confinement fusion (ICF) targets was planned, following the STIM-T and PIXE-T experiments performed at Fudan University [6, 7]. The ICF target is a small spherical shell, a few hundred micrometers in diameter, made of a polymer of uniform composition and mass density, doped with high Z elements, such as Ge. In general, the dopant's distribution should be uniform as it is intended to avoid laser imprinting and limit hydrodynamic instabilities in ICF ignition. The objective of Fudan's experiments is to quantify the Ge content in ICF targets and check its uniformity. Their results were obtained using a reconstruction program developed at Fudan University, based on Filtered Back Projection (FBP) algorithm in MATLAB. However, the correction implemented in this program to compensate for X-ray loss does not take into account the solid angle of the detector, which is assumed



as a point. This assumption requires having a small solid angle for the detection in experiments, which leads to an increase of collection time. The experimental duration is approximately 20 hours in total [6]. In this collaboration, one aim is to validate if the reconstruction methods developed at LP2I Bordeaux for biological samples, which are able to take into account a large detection solid angle, are suited to ICF targets. This would be an advantage, because it could significantly reduce the duration of experiments. At present, two reconstruction software packages, TomoRebuild [2], and JPIXET [8, 9], are able to take into account large solid angles in the reconstruction process. Their performances have been compared in previous studies on experimental data of biological specimens [4, 10]. The mass densities obtained by the two packages were found similar. However, this was only a rough comparison of one package relative to the other, due to the lack of reference data. The Geant4 simulations of tomography experiments allow us to perform more accurate tests. The main purpose of our study on the ICF target is to test the ability of the different reconstruction methods implemented in TomoRebuild and JPIXET to produce accurate quantitative images of ICF targets using a large solid angle.

We designed a phantom of ICF target according to the samples analyzed at Fudan University [6]. The phantom is a spherical shell with outer radius 196  $\mu\text{m}$  and thickness 25  $\mu\text{m}$ . It is composed of a polymer of uniform composition (stoichiometric ratio C:H = 5:7) and mass density (1.08  $\text{g}/\text{cm}^3$ ), doped with Ge (5% in mass). The mass percentage of each element is indicated in Table 4 - 3.

*Table 4 - 3. Composition of the phantom of ICF target.*

<b>Element</b>	<b>Mass percentage (%)</b>
<b>C</b>	85.0
<b>H</b>	10.0
<b>Ge</b>	5.0

## 3.2. Scan parameters

### 3.2.1. Problematic

The number of incident protons is a crucial point as the simulations can last several days, especially the PIXE-T simulation. Indeed, PIXE-T requires much more incident protons than STIM-T because of the low X-ray production cross-sections. A PIXE-T experiment usually requires  $10^8$  to  $10^9$  protons for each beam position [11]. If the same conditions were applied in the simulation, it would be unrealistic in terms of duration. In order to minimize the simulation duration while maintaining a good quality of image, we reduced the number of protons to  $\sim 10^6$  protons. In this case, to compensate for the reduction of generated X-rays, we took a very large solid angle (half apex angle of the detector) for the selection of the X-rays, as explained in section 2.4.3.

### 3.2.2. Cube

3D STIM-T simulations were performed by scanning 64 or 128 slices, as in experiments. Due to the long duration of PIXE-T simulations, only one slice of interest was scanned in PIXE-T simulations. The typical scan parameters are showed in the Table 4 - 4. For STIM-T, we also performed simulation tests to study the effect of different numbers of protons on the values of reconstructed mass density (see section 5.1.1).

Table 4 - 4. Scan parameters for the STIM-T and PIXE-T simulation of the cube.

	STIM-T	PIXE-T
<b>Proton energy (MeV)</b>	1.5	1.5
<b>Nb of protons</b>	100	10 <sup>6</sup>
<b>Nb of projections</b>	100	100
<b>Nb of slices</b>	64	1 (central slice)
<b>Nb of pixels</b>	128	128
<b>Angular span</b>	180°	180°
<b>Scan width (μm)</b>	9 for cube 1	9 for cube 1
	72 for cube 2	72 for cube 2
<b>Scan height (μm)</b>	9 for cube 1	N/A*
	72 for cube 2	N/A*

\*N/A: Not Applicable, because only one slice is scanned in PIXE-T simulation.

### 3.2.3. *C. elegans*

The scan parameters used for *C. elegans* are presented in the Table 4 - 5.

Table 4 - 5. Scan parameters for STIM-T and PIXE-T simulations of *C. elegans*.

	STIM-T	PIXE-T
<b>Proton energy (MeV)</b>	1.5	1.5
<b>Nb of protons</b>	100	10 <sup>6</sup>
<b>Nb of projections</b>	100	100
<b>Nb of slices</b>	128	1
<b>Nb of pixels</b>	128	128
<b>Angular span</b>	180°	180°
<b>Scan width (μm)</b>	76.5	76.5
<b>Scan height (μm)</b>	201	N/A*

\*N/A: Not Applicable, because only one slice is scanned in PIXE-T simulation.

For PIXE-T simulations, only one slice was scanned, chosen in the region containing the cell nuclei and the Ti rich region (Figure 4 - 17). For STIM-T, we also performed simulation tests to study the effect of different numbers of protons on values of reconstructed mass density (section 5.1.3) as well as the reconstructed image quality (section 5.1.4).

### 3.2.4. ICF target

The scan parameters used for the ICF target are presented in Table 4 - 6, according to the experimental conditions at Fudan University [6].

Table 4 - 6. Scan parameters for STIM-T and PIXE-T simulations of the ICF target.

	STIM-T	PIXE-T
<b>Proton energy (MeV)</b>	4	4
<b>Nb of protons</b>	100	$2 \times 10^6$
<b>Nb of projections</b>	100	100
<b>Nb of slices</b>	128	1
<b>Nb of pixels</b>	128	128
<b>Angular span</b>	180°	180°
<b>Scan width (<math>\mu\text{m}</math>)</b>	500	500
<b>Scan height (<math>\mu\text{m}</math>)</b>	500	N/A*

\*N/A: Not Applicable, because only one slice is scanned in PIXE-T simulation.

## 3.3. Physics models and optimization of duration

The physics models used in our simulations were chosen according to previous studies for steady beam PIXE analysis, based on the Geant4 *TestEm5* example [12]:

- *G4EmLivermorePhysics* electromagnetic physics class, as it takes into account atomic shells and is well suited for the simulation of X-ray emission processes in the proton energy range of a few MeV;
- Bearden database for a better accuracy on the energy of emitted X-rays [13].

The maximal interaction step length was set to ensure at least 10 effective steps along the particle transportation. As already mentioned, in order to minimize computing time, the simulation code was designed for multithreading. In addition, a low energy production cut of 900 eV was applied for the generation of secondary particles including X-rays. Thus, the X-rays were not generated if their energy was below 900 eV. This threshold corresponds to the typical lowest energy limit of most X-ray detectors used in PIXE experiments. Indeed, X-ray absorption by the entrance window of the detector becomes too high for detecting X-ray at lower energies. It was also checked that, as expected, this energy cutoff did not affect the production of X-rays of interest, nor the residual energy of protons. This threshold was

shown to significantly reduce the simulation time [14]. For example, for *C. elegans*, under these conditions using a multicore computer with 100 threads, 2.7 GHz, 768 Gb RAM, it took about 1.3 days with the cutoff for a PIXE-T simulation of 100 projections $\times$ 1 slice $\times$ 128 pixels with  $10^6$  protons per shot, whereas it took about 11 days without the cutoff. In a similar way, the duration of the simulation was also reduced by a factor of  $\sim 10$  for a STIM-T simulation of 100 projections $\times$ 128 slice $\times$ 128 pixels with 100 protons per shot: about 43 min with the energy cutoff, compared to 7 h without [2].

### 3.4. Parameters used for the selection of simulated data

As explained in section 2.3.1, the detection of particles of interest is modelled by making a selection of simulation output data *after* finishing the simulation. In our case, the size of the phantoms is negligible compared to the size of the entrance window of the detector. So, it is relevant to use the approximate selection with momentum, as described in section 2.4.3. The parameters used for the selection are explained in section 2.4.3 and summarized in Table 4 - 7.

*Table 4 - 7. Selection parameters used for STIM-T and PIXE-T simulations. The selection with particle momentum is applied here.*

Simulation type	Selection parameters (Detector geometry)	Angle value
STIM-T	Angular position $\alpha$	$0^\circ$
	Half apex angle $\theta$	$10.2^\circ$
PIXE-T	Angular position $\alpha$	$135^\circ$ (and $315^\circ$ in addition for <i>C. elegans</i> )
	Half apex angle $\theta$	$70^\circ$

## 4. Reconstruction of tomographic images

### 4.1. Reconstruction methods

The tomographic images were reconstructed using the TomoRebuild program, developed at CENBG/LP2I Bordeaux. The reconstruction methods implemented in TomoRebuild are based on algorithms initially designed for medical imaging [10]. TomoRebuild provides NLXP and XA corrections for PIXE-T reconstruction, taking into account a large X-ray detection solid angle. The calculation of the corrections is based on the knowledge of the 3D distribution of mass density obtained from STIM-T. The STIM-T reconstruction assumes a global uniform composition in major chemical elements, which is suited to a wide variety of specimens such as biological samples, *e.g.*, *C. elegans*, or ICF targets. This assumption allows STIM-T reconstruction to be performed, independently from PIXE-T. Based on the 3D STIM-T image, the NLXP and XA corrections for each X-ray emitting element are then computed at each projection angle. They are stored in correction matrices that are incorporated during the iterative process of PIXE-T reconstruction. In this way, each chemical element of interest is reconstructed separately from one another: one image is produced for each analyzed element. TomoRebuild is developed in C++ with several reconstruction algorithms implemented. In our study, we used the following methods:

- Filtered Back Projection (FBP), based on the exact analytical solution of the continuous description of the tomography problem. FBP is often preferred as a simple and fast method suited for not too noisy data, especially transmission tomography, *i.e.*, in our case STIM-T data;
- Maximum Likelihood Expectation Maximization (MLEM), an iterative method based on a discrete formulation of the tomography problem. MLEM is often used for PIXE-T as a robust algorithm even with noisy and/or incomplete data. The optimal iteration number can be determined by different methods of image analysis. In our study, we use Normalized Average Absolute Deviation (NAAD) and Normalized Root Mean Squared Deviation (NRMSD) calculations, as explained in section 4.2.

The reconstruction time does not constitute a severe limitation. It takes 1 minute on a very basic PC 3.4 GHz, 8 Go RAM to reconstruct a full 3D STIM-T image of  $128 \times 128 \times 128$  voxels using FBP, and 25 minutes using MLEM. For PIXE-T, the implementation of NLXP and XA corrections in large solid angle requires using an iterative reconstruction method, *i.e.*, MLEM in our case. The most time-consuming step is the calculation of the XA correction matrix, because the large detection solid angle is modelled by finely discretizing the entrance window of the detector [2]. In these conditions, it takes about 2 minutes to reconstruct one PIXE-T slice of  $128 \times 128$  voxels.

## 4.2. Reconstructed image analysis

The reconstructed images presented here were displayed using the Amira graphic software package (<https://www.fei.com/software/amira-3d-for-life-sciences>), which is particularly suitable for 3D rendering, and the public domain software ImageJ, developed at the National Institutes of Health (<https://imagej.nih.gov/ij>). The quality of the reconstructed images was evaluated by comparison to the original phantom, considered as a reference, at two levels: global and local.

The global discrepancy was assessed using two different calculations: the Normalized Average Absolute Deviation (NAAD) and the Normalized Root Mean Squared Deviation (NRMSD) [1], defined as follows:

$$NAAD = \frac{\sum_{i=0}^{N-1} |I_{ref}(i) - I(i)|}{\sum_{i=0}^{N-1} |I_{ref}(i)|}$$

$$NRMSD = \sqrt{\frac{\sum_{i=0}^{N-1} (I_{ref}(i) - I(i))^2}{\sum_{i=0}^{N-1} (I_{ref}(i))^2}}$$

where:

- $N$  is the number of pixels,  $N = 128 \times 128$ ;
- $i$  is the pixel index going from 0 to  $N-1$ ;
- $I(i)$  is the density value of pixel of the reconstructed image;
- $I_{ref}(i)$  is the density value of pixel  $i$  of the voxelized original phantom. The construction of the voxelized original phantom is described in section 4.3.

NAAD and NRMSD calculations were used for two purposes:

- The determination of the optimal number of iterations for PIXE-T reconstruction using MLEM, which was 32 iterations in our study [1];
- The determination of the optimal number of incident protons for STIM-T simulations, as presented in section 5.1.4.

At the local level, we evaluated the quality of reconstruction by comparing the reconstructed densities to the reference values of the phantoms, in different regions of interest (ROI). In addition, line profiles were also studied for the cube phantom to study the edge sharpness, as presented in section 5.1.2.

## 4.3. Construction of voxelized phantoms

The comparison of the reconstructed images to the original phantom requires having voxelized phantoms with the same size and the same number of voxels, for example to calculate:

- The NAAD and NRMSD values, as mentioned above;
- The difference images, which are useful to reveal small differences between reconstructed and original images, as shown in section 5.2.8.

We explain here how we proceed to construct the voxelized phantom for the ICF target (Figure 4 - 18).

In fact, two voxelized phantoms were designed:

- The first one to compare with STIM-T reconstructed images;
- The second one to compare with PIXE-T reconstructed images.

The only difference between the two voxelized phantoms lies in the density values set at each voxel:

- For STIM-T, we considered the mass density of the ICF target material,  $1.08 \text{ g/cm}^3$ ;
- For PIXE-T, we considered the mass density of Ge,  $0.054 \text{ g/cm}^3$ .

The construction of voxelized phantoms was carried-out using Python scripts. The voxel size was defined by dividing the scan size (here  $500 \mu\text{m}$  in both y and z directions) by the number of pixels of the scan. One difficulty is to handle the density distribution for the voxels at the border of the object, to make sure the density decreases gradually from the object to the vacuum background. Indeed, the object is a spherical shell, so its border is not parallel to the grid of voxels. Therefore, we first built a phantom of the same geometry, but with a resolution higher by a factor of 8, *i.e.*,  $1024 \times 1024 \times 1024$  voxels. Then, the density of each voxel of the final  $128 \times 128 \times 128$  voxels phantom was obtained by taking the mean of the  $8 \times 8 \times 8$  neighboring voxels of the high-resolution phantom. The *C. elegans* voxelized phantom was obtained in the same way (Figure 4 - 18).

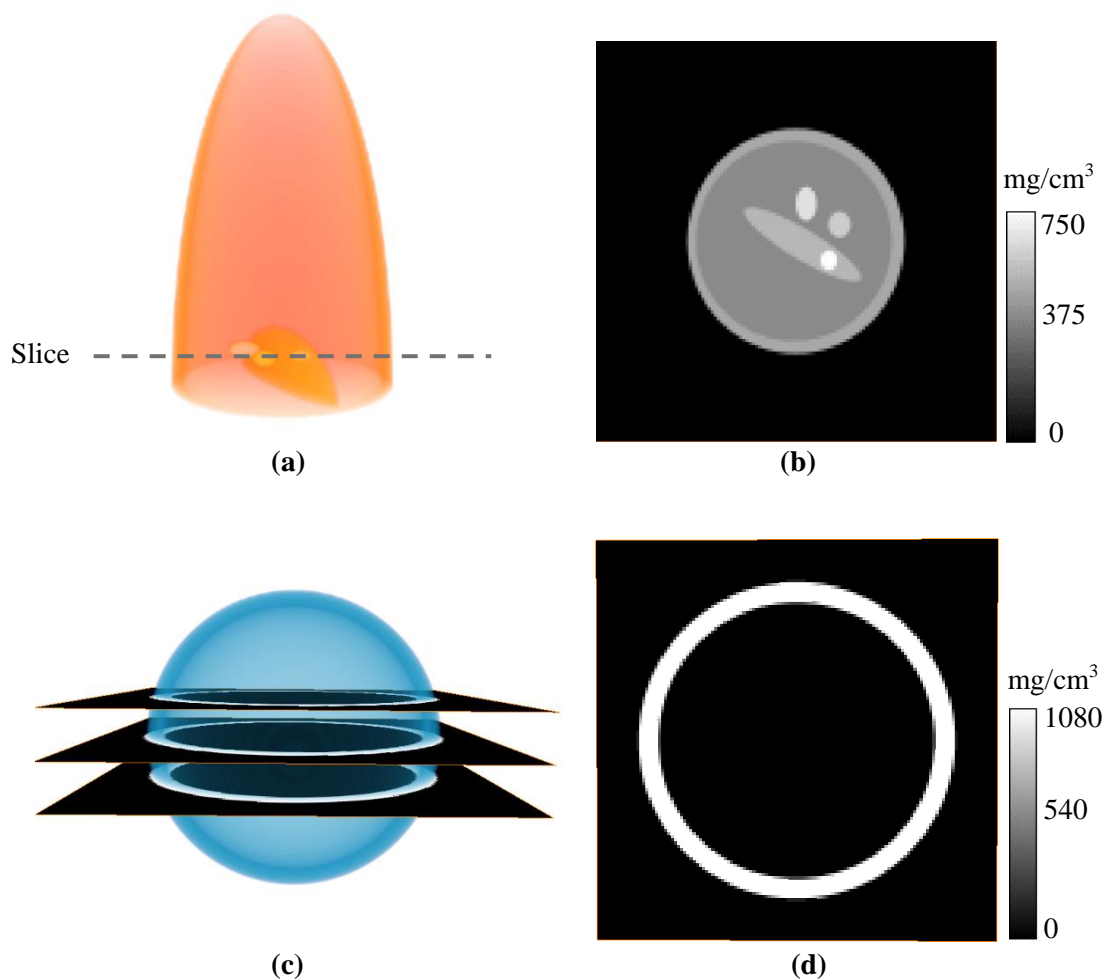


Figure 4 - 18. Voxelizephantoms of *C. elegans* (a) and the ICF target (c) for STIM-T image analysis.

Extracted slices: slice of interest of *C. elegans* (b) as shown in Figure 4 - 17;

central slice of ICF target (d).



## 5. Results

### 5.1. STIM-T analysis

#### 5.1.1. Mass density of cube

STIM-T simulations of 100 projections $\times$ 64 slices $\times$ 128 pixels were performed on the cube phantom of 5  $\mu\text{m}$ . The tomographic images were reconstructed using both FBP and MLEM methods (Figure 4 - 19). The image analysis was performed on the central slice of the cube (Figure 4 - 19 (a)). Non-physical negative density values were observed outside the cube by using FBP method (Figure 4 - 19 (b)), which are inherent to this reconstruction method. A low-density threshold may be used to remove this background. The resulting image (Figure 4 - 19 (c)) is then very similar to the image using MLEM (Figure 4 - 19 (d)), in which, the density values are intrinsically constrained to be positive.

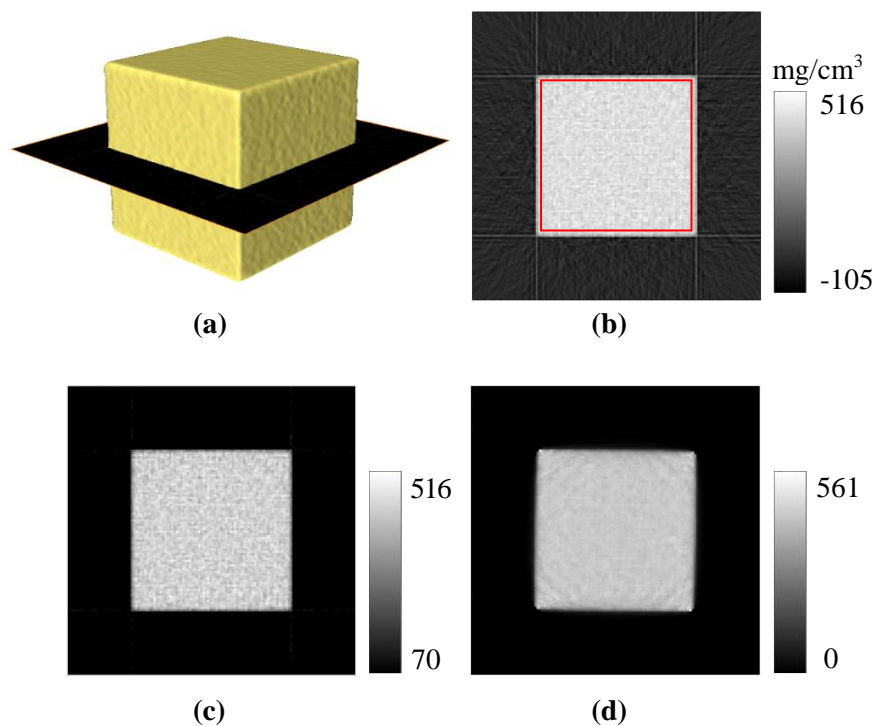


Figure 4 - 19. Reconstruction of the STIM-T simulated data for the cube phantom of 5  $\mu\text{m}$ , using 1000 protons per shot. The 3D image (a) was displayed using an isosurface value close to zero, corresponding to the boundary between the outer surface of the cube and surrounding vacuum. The central slice is displayed, as obtained by FBP without (b) and with (c) low density threshold, and by MLEM (d). For the slices, a linear grey scale was used. The ROI (red line) used for mean mass density calculation is displayed in (b).

The mean mass density was calculated in a ROI avoiding the sides of the cube (Figure 4 - 19 (b)), in order to discard partial volume effects that could alter the calculation (Table 4 - 8). The relative difference (RD) was calculated as follows, taking the original phantom as a reference:

$$RD (\%) = 100 * \frac{\text{Reconstructed value} - \text{reference value}}{\text{reference value}} \quad (4 - 10)$$

The calculated densities were found in good agreement with the reference value. The RD were below 2% for both 100 and 1000 protons per shot, using FBP or MLEM methods.

Table 4 - 8. Mean mass density of the cube phantom of 5 $\mu\text{m}$  in the ROI displayed in Figure 4 - 19 (b), using FBP and MLEM methods. The STIM-T simulations results were obtained using 100 or 1000 protons per shot. The given uncertainty corresponds to the standard deviation in the ROI.

Reconstruction method	100 protons		1000 protons		Reference (mg/cm <sup>3</sup> )
	Mean mass density (mg/cm <sup>3</sup> )	Relative difference (%)	Mean mass density (mg/cm <sup>3</sup> )	Relative difference (%)	
FBP	435 $\pm$ 42	1.1	435 $\pm$ 24	1.1	440
MLEM	438 $\pm$ 21	0.37	438 $\pm$ 15	0.41	

### 5.1.2. Line profiles for cube

The quality of the images reconstructed using FBP and MLEM was also evaluated using line profiles across the cube (Figure 4 - 20). As mentioned in section 5.1.1, negative values were observed outside the phantom using FBP, whereas the densities were exactly at zero using MLEM. However, better definition of the edges (arrows in Figure 4 - 20) was given by FBP. The partial volume effects affected only one pixel at the border of the cube using FBP, while this transition region extended on  $\pm 2$  pixels for MLEM.

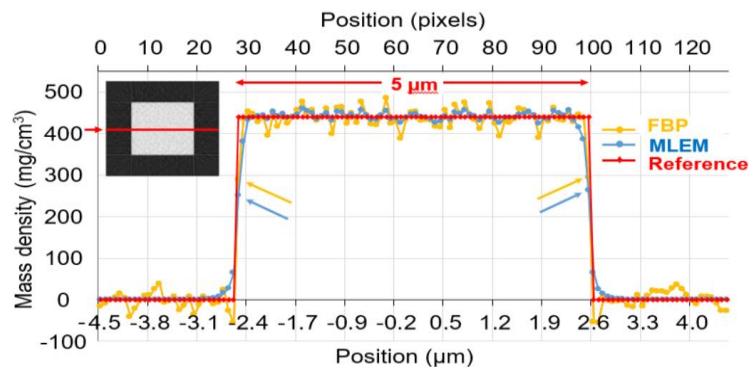
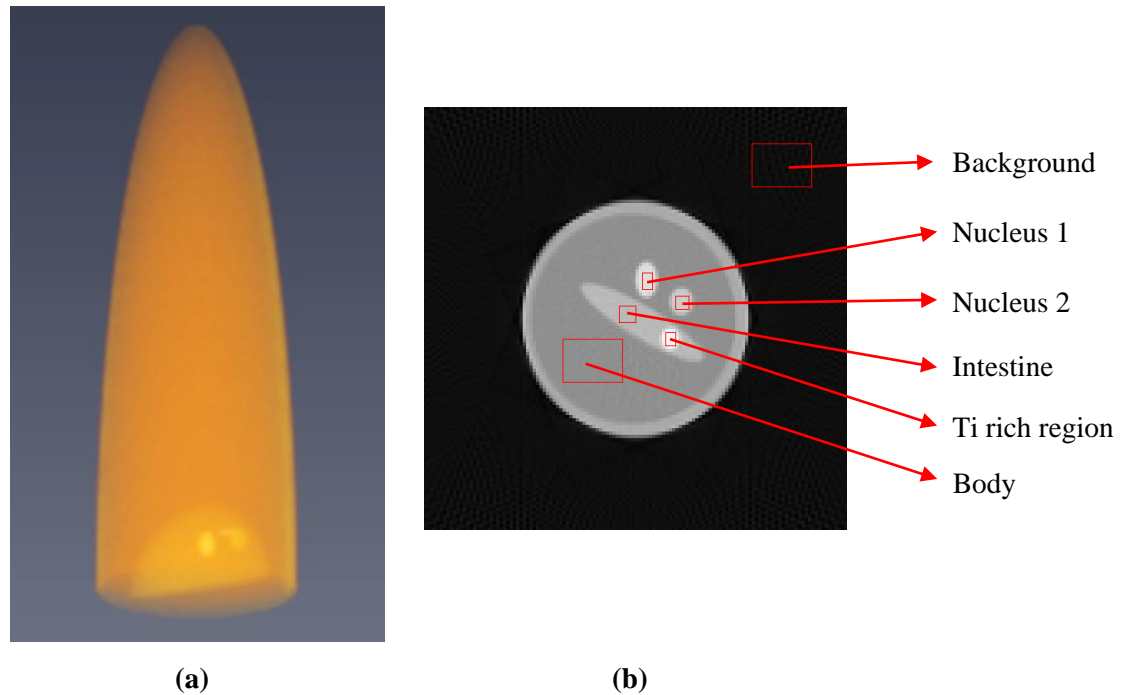


Figure 4 - 20. Profile through the cube phantom (upper left image), comparing the reconstructed images using FBP and MLEM methods to the original Geant4 phantom (reference). The calculated mass density is displayed according to the position along the 128 pixels of the profile (from -4.5 to +4.5  $\mu\text{m}$ ). In this case, the reference density values are constant, at 440 mg/cm<sup>3</sup> within the cube and 0 outside.

### 5.1.3. Mass density of *C. elegans*

STIM-T simulations of 100 projections×128 slices×128 pixels were performed on the *C. elegans* phantom. The 3D distribution of mass density was reconstructed (Figure 4 - 21 (a)).



*Figure 4 - 21. The 3D distribution (a) obtained using FBP method. The color and transparency scale go from transparent dark red (lowest density) to opaque yellow (highest density). The slice of interest is displayed with the six ROI (b).*

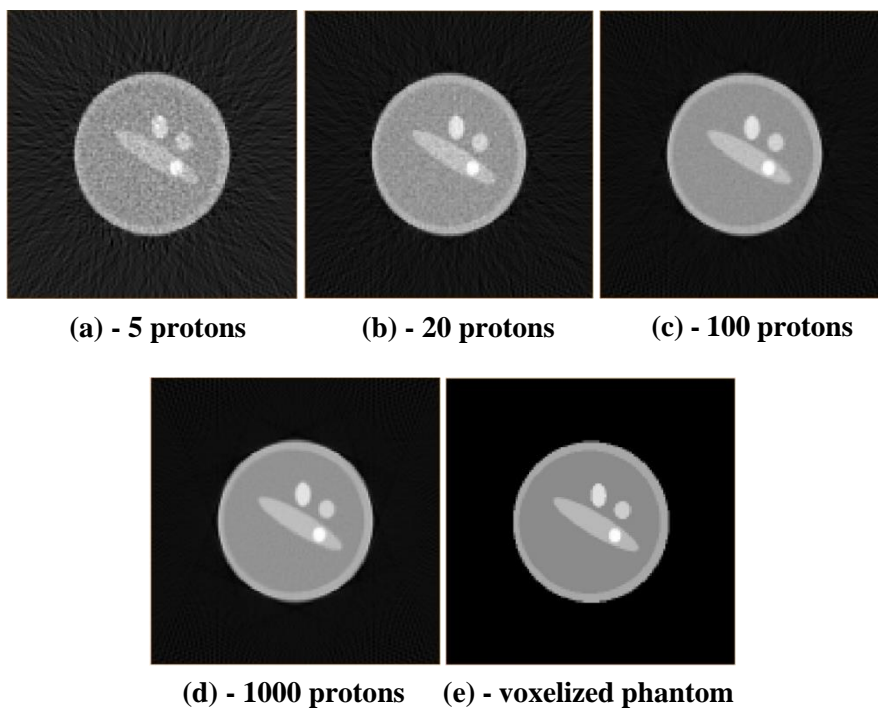
We analyzed the slice of interest (Figure 4 - 17), which corresponds to the slice in PIXE-T simulation. Six rectangular ROI (including the background) avoiding the borders of the ellipsoids were defined. Table 4 - 9 shows the mean densities of *C. elegans* in the different ROI (the background is not considered) using FBP and MLEM methods. Very similar results were obtained for 100 and 1000 protons per shot, and are in agreement with the reference values. The RD are below 2% for all the ROI, using both FBP and MLEM methods.

Table 4 - 9. Mean mass density of *C. elegans* in the five ROI displayed in Figure 4 - 21 (b), using FBP and MLEM methods. The STIM-T simulations results were obtained using 100 or 1000 protons per shot. The given uncertainty corresponds to the standard deviation in the ROI.

Reconstruction method	ROI	100 protons		1000 protons		Reference (mg/cm <sup>3</sup> )
		Mean mass density (mg/cm <sup>3</sup> )	Relative difference (%)	Mean mass density (mg/cm <sup>3</sup> )	Relative difference (%)	
FBP	Body	411 ± 11	<b>0.83</b>	410.9 ± 4.7	<b>0.73</b>	<b>408</b>
	Nucleus 1	666 ± 11	<b>0.43</b>	666.0 ± 5.7	<b>0.46</b>	<b>663</b>
	Nucleus 2	604 ± 12	<b>0.14</b>	604.5 ± 6.0	<b>0.26</b>	<b>603</b>
	Intestine	544.5 ± 9.8	<b>0.65</b>	545.5 ± 4.1	<b>0.83</b>	<b>541</b>
	Ti region	758 ± 11	<b>0.97</b>	757.5 ± 6.5	<b>0.86</b>	<b>751</b>
MLEM	Body	414.3 ± 4.4	<b>1.6</b>	414.1 ± 1.9	<b>1.5</b>	<b>408</b>
	Nucleus 1	670.0 ± 8.6	<b>1.1</b>	670.3 ± 4.5	<b>1.2</b>	<b>663</b>
	Nucleus 2	600.3 ± 7.6	<b>-0.45</b>	600.1 ± 5.5	<b>-0.48</b>	<b>603</b>
	Intestine	548.0 ± 5.8	<b>1.3</b>	549.2 ± 2.8	<b>1.6</b>	<b>541</b>
	Ti region	757 ± 11	<b>0.78</b>	756.6 ± 0.21	<b>0.75</b>	<b>751</b>

#### 5.1.4. Optimal number of incident protons

The results presented in Table 4 - 9 show that the mean mass density is close to the reference value for 100 and 1000 protons, with very similar RD. However using 100 or 1000 protons does have a significant difference on the simulation duration. Thus, it is important to determine the optimal number of protons per shot, allowing minimizing the simulation duration whilst keeping a good accuracy in the reconstructed images. Figure 4 - 22 shows the FBP reconstructed slice obtained with different numbers of protons per shot. Obviously, the quality of image is improved as the number of protons increases.



*Figure 4 - 22. Reconstructed STIM-T slice of C. elegans, using FBP method with ramp filter [15] obtained with different numbers of protons per shot (a-d) and slice from voxelized phantom (e).*

Quantitatively, the mean mass density values were compared with the reference values (Figure 4 - 23). The results were found in agreement with the reference whatever the ROI or the number of protons, with statistical fluctuations decreasing as the number of protons increases.

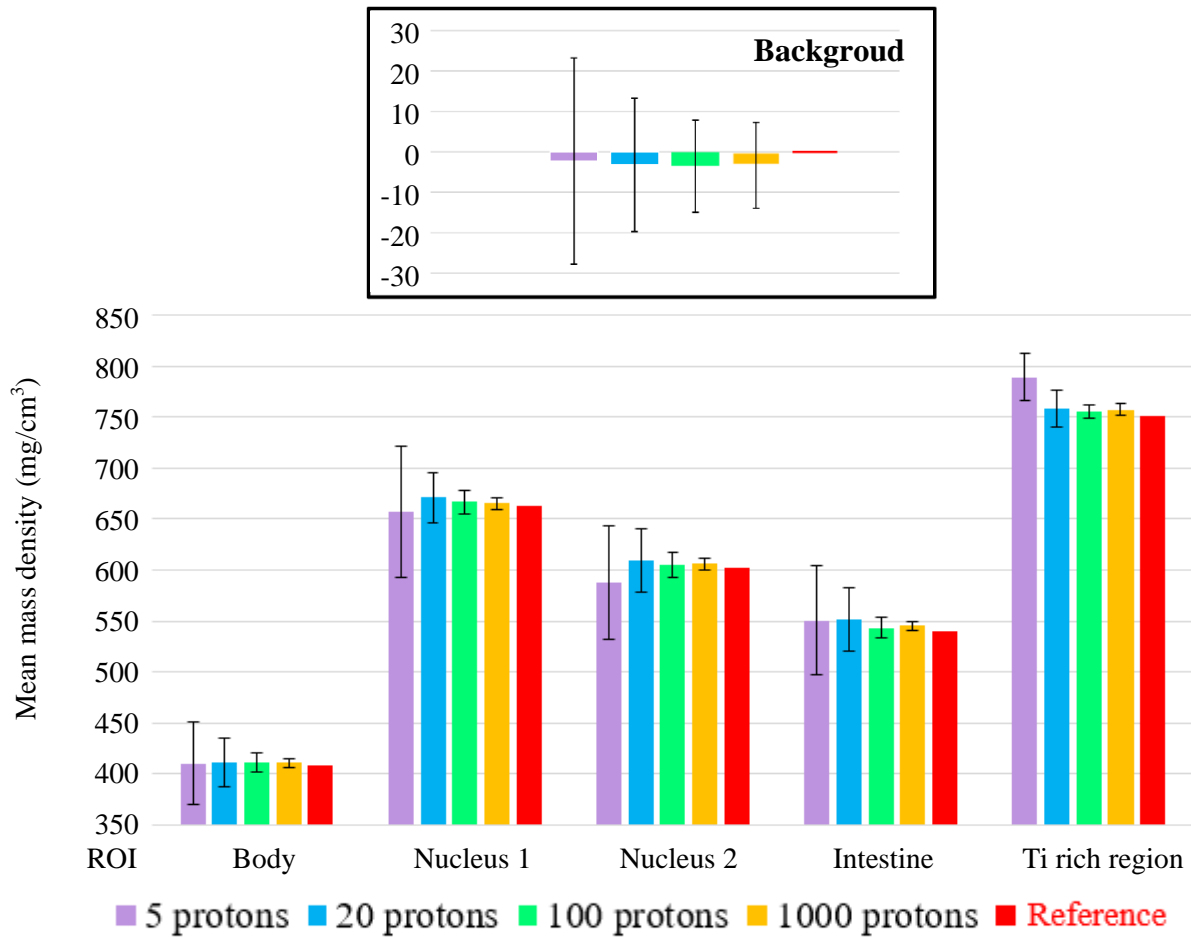


Figure 4 - 23. Mean mass density using FBP reconstruction in the different ROI (as shown in Figure 4 - 21 (b)) of the *C. elegans* phantom, obtained from STIM-T simulation with 5, 20, 100 and 1000 protons per shot, compared to the original Geant4 phantom (reference). The error bars correspond to the standard deviation.

In order to evaluate the evolution of the image quality as a function of the number of protons, we calculated the global discrepancy between the reconstructed images and the original phantom, using NAAD and NRMSD, as explained in section 4.2. We plotted this global relative error as a function of the number of protons per shot (Figure 4 - 24). As expected, for both NAAD and NRMSD, the relative error decreases as the number of protons increases. However, the improvement becomes lesser for higher numbers of protons: for instance, it is conspicuous when going from 5 to 20 protons per shot, corresponding to a 46% decrease for NAAD, whereas there is very little improvement when going from 100 to 1000 protons (with only 5% decrease). The NAAD parameter was eventually preferred for this quantification because it varies more quickly according to the number of protons. We decided to use 100 protons as the optimal number of incident protons, which was also applied for the STIM-T simulations of ICF target.

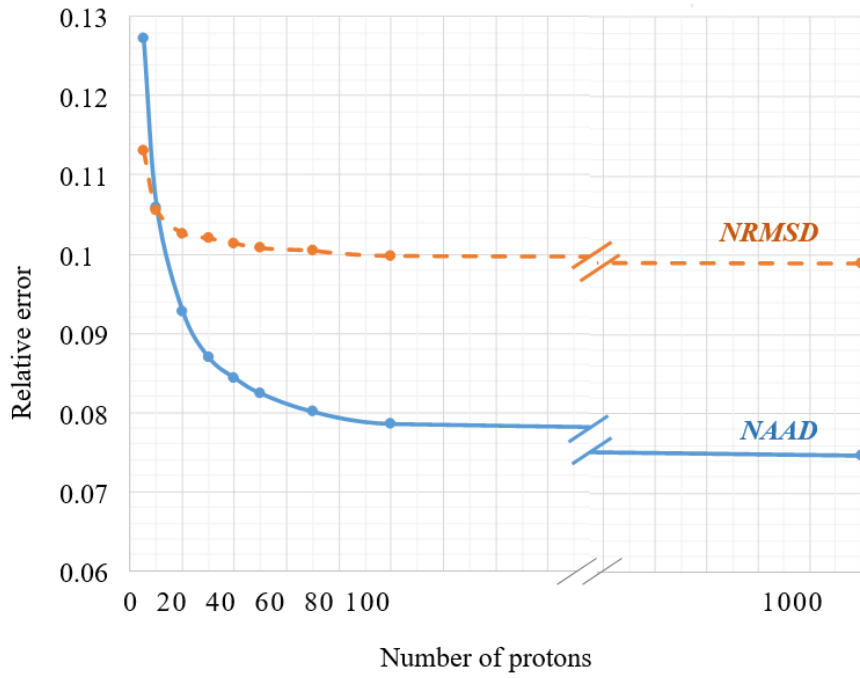


Figure 4 - 24. NRSMD and NAAD evaluation of the relative error between the reconstructed FBP image (ramp filter) and the voxelized *C. elegans* phantom used as a reference. The horizontal scale representing the number of protons was interrupted between 100 and 1000 for clarity, as there is very little variation between these two points.

### 5.1.5. Mass density of ICF target

Based on the study in section 5.1.4, we also chose 100 protons per shot for the STIM-T simulation of ICF target. The simulation was composed of 100 projections $\times$ 128 slices $\times$ 128 pixels. 3D images were obtained using FBP and MLEM methods. The central slice corresponding to the scanned slice in PIXE-T simulation was analyzed (Figure 4 - 25).

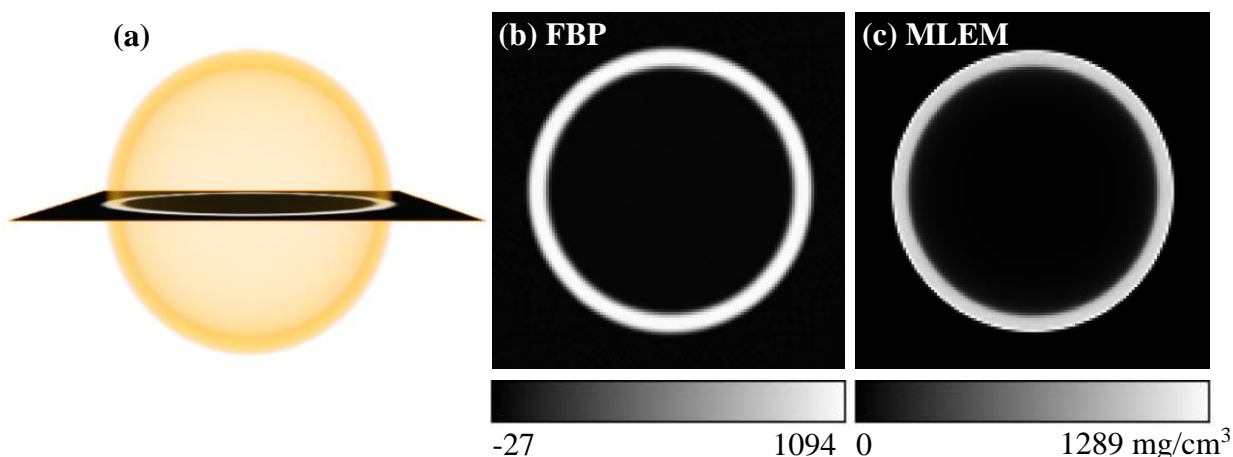


Figure 4 - 25. Reconstruction of the 3D STIM-T image of the phantom (a); central slice obtained using FBP (b) and MLEM (c). The images are displayed here with no additional filter (except the Hann filter [15] used for FBP) nor threshold.

As for *C. elegans*, we compared the reconstructed mass density using FBP and MLEM methods with the reference phantom. For this, we defined four ROI inside the shell, to check whether the reconstructed mass density was uniform (Figure 4 - 26: ROI 1-4). We also defined two ROI in the background to verify whether the calculated mass density was close to 0 (Figure 4 - 26: ROI 5-6). The mean densities in each ROI are shown in the histogram in Figure 4 - 26. ROI 6 was not included in the histogram, because the calculated densities using both methods were very close to 0. Considering each reconstruction method, we observed there was no significant difference between the calculated mass density of ROI 1-4, thus, we considered the mean mass density of ROI 1-4 to compare the accuracy of the different reconstruction methods (Table 4 - 10). For the inner background, the densities were close to 0 (Figure 4 - 26: ROI 5). The uniformity was also observed for the shell region (Figure 4 - 26: ROI 1-4). The calculated mean densities using both methods were in agreement with the reference, within an accuracy  $\leq - 2.5\%$ .



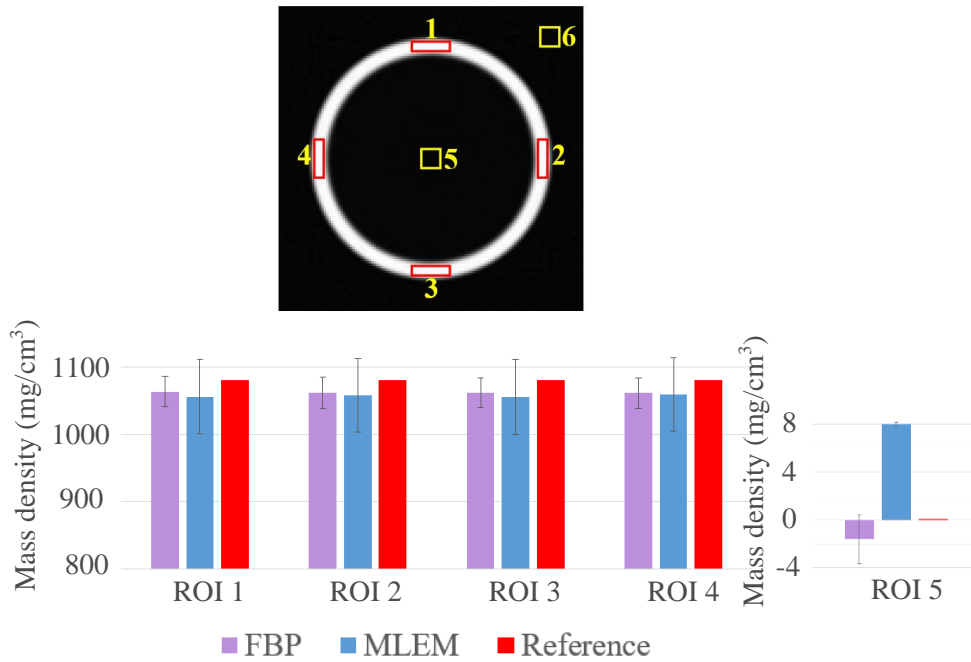


Figure 4 - 26. Six defined ROI, all of them have the same area of 64 pixels (top); Histogram (bottom) of STIM-T mass densities in ROI-1-5, obtained using different reconstruction methods, compared to the reference densities of the original phantom. The error bars correspond to the standard deviation.

Table 4 - 10. Mean mass density calculated by different reconstruction methods from STIM-T simulation results. The mean mass density is the mean value of ROI 1-4. The indicated uncertainty only corresponds to the resulting standard deviation.

	Mean mass density (mg/cm <sup>3</sup> )	Relative difference (%)
<b>FBP</b>	1062 ± 12	-1.7
<b>MLEM</b>	1057 ± 28	-2.2
<b>Reference value</b>	<b>1080</b>	

## 5.2. PIXE-T analysis

### 5.2.1. Mass density of phosphorus in cube

As already explained, in our study phosphorus was the most attenuated element in PIXE analysis. For this reason, the quantification of phosphorus mass density was studied in cube phantoms with different thicknesses. The PIXE-T simulations were performed for the central slice of the cube phantoms of 5  $\mu\text{m}$  and 40  $\mu\text{m}$  respectively. The mean densities in the ROI (Figure 4 - 19 (b)) calculated using FBP and MLEM methods are given in Table 4 - 11. As expected, the results for the cube of 5  $\mu\text{m}$  (thin target)

were in agreement with the reference value for both reconstruction methods, with an accuracy  $\leq 3\%$ . For the cube of 40  $\mu\text{m}$  (thick target), as expected, the reconstructed mass density was underestimated because we did not take into account any correction in the reconstruction. The corrections on X-ray attenuation will be presented in sections 5.3.2 - 5.3.4.

*Table 4 - 11. Mean mass density of phosphorus, obtained from the reconstruction of PIXE-T simulation of the cubes of 5  $\mu\text{m}$  and 40  $\mu\text{m}$ , without taking into account X-ray signal attenuation in the reconstruction process. The ROI used for mean mass density calculation is shown in Figure 4 - 19 (b).*

Phantom type	FBP		MLEM		Reference P mean mass density ( $\text{mg}/\text{cm}^3$ )
	P mean mass density ( $\text{mg}/\text{cm}^3$ )	Relative difference (%)	P mean mass density ( $\text{mg}/\text{cm}^3$ )	Relative difference (%)	
Cube 5 $\mu\text{m}$	$430 \pm 76$	-2.4	$434 \pm 34$	-1.5	<b>440</b>
Cube 40 $\mu\text{m}$	$19.0 \pm 6.1$	-36	$19.5 \pm 3.3$	-35	<b>29.5</b>

### 5.2.2. NLXP and XA corrections of PIXE-T images

The NLXP and XA corrections implemented in TomoRebuild were developed by Hugo Jalenques, during his internship of last year of Master degree in computer science in 2020 [2], on the basis of a previous work [10]. The principle of these corrections will be briefly presented here. The NLXP and XA corrections are matrices of multiplicative factors that are included in the reconstruction process. They are both calculated *prior to PIXE reconstruction* using the 3D distribution of mass density obtained from STIM-T, assuming a global uniform composition in major chemical elements as explained in section 4.1.

#### a) Calculation of correction matrix for NLXP

The NLXP effect is due to the decrease of proton energy into the sample, leading to a variation of ionisation cross section. The NLXP correction is calculated along the path of the beam (Figure 4 - 12), so it requires the distribution of the mass density of the considered slice. More precisely, the X-ray production cross-section  $\sigma$ , for a given chemical element, is a function of the energy  $E$  of the incident proton at the position where the interaction occurs. Thus, the NLXP correction factor at voxel  $(i, j)$  is given by the ratio of the cross section at energy  $E_{ij}$  at this voxel, divided by the cross section at the incident energy  $E_0$ :

$$NLXP(i, j) = \frac{\sigma(E_{ij})}{\sigma(E_0)}$$

***b) Calculation of correction matrix for XA***

The XA effect occurs when the X-ray passes through the material from its emitting point to the detector (Figure 4 - 12). In order to model the large solid angle of the detector, the calculation of XA correction requires the knowledge of the 3D mass density distribution of the analyzed volume, which is obtained from STIM-T for the whole object, not only for one slice. In order to keep the calculation accurate even considering large solid angles, the detector is divided in N surface elements (Figure 4 - 27). For instance, the results presented in this thesis were obtained using 300 surface elements. The correction factor  $XA_k$  is defined considering the X-ray trajectory  $d_k$ , from the emitting voxel  $(i, j)$  to the impact point  $e_k$  on the detector:

$$XA_k = e^{-\mu d_k}$$

where:

- $d_k$  is the thickness through which, the X-ray passes, expressed in terms of areal density in  $\text{g}/\text{cm}^2$ ;
- $\mu$  is the mass attenuation coefficient expressed in  $\text{cm}^2/\text{g}$ ;

The global  $XA(i, j)$  correction at voxel  $(i, j)$  is expressed by the mean value of factors  $XA_k$  on all surface elements:

$$XA(i, j) = \frac{1}{N} \sum_{k=0}^{N-1} XA_k = \frac{1}{N} \sum_{k=0}^{N-1} e^{-\mu d_k}$$

where N is the number of the surface elements.

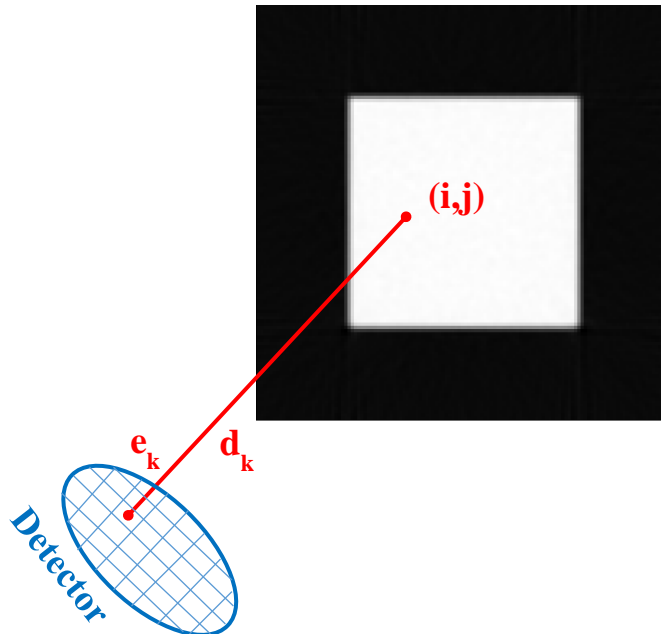


Figure 4 - 27. The areal density  $d_k$  is calculated by integrating the mass density along the distance between the considered voxel  $(i, j)$  of the STIM-T slice and the surface element  $e_k$  of the detector.

### ***c) Final correction matrix***

The final correction at voxel  $(i,j)$  is the product of NLXP and XA factors. It is important to note that the correction matrix has to be calculated for each projection (each angle  $\theta$ ), in order to take into account the direction of the beam and of the detector, relatively to the object. An example of correction matrices (Figure 4 - 28) obtained for phosphorus in the cube phantom of  $40\ \mu\text{m}$ , which is homogeneous in density and composition, shows the effect of NLXP (Figure 4 - 28 (a)) and XA (Figure 4 - 28 (b)) for a specific (arbitrary) projection angle. In Figure 4 - 28 (a), the beam is horizontal, coming from the left hand side (arrows). Thus, the voxels of the phantom need to be corrected more and more when going deeper in the object (towards the right hand side), because the number of X-rays emitted from these voxels is lower and lower due to NLXP. Figure 4 - 28 (b) displays the effect of XA, when for instance the detector is placed at  $135^\circ$  (bottom left). The X-rays emitted from voxels far from the detector undergo a stronger attenuation in the object, so the XA correction is stronger in these regions (up right). The total correction matrix (Figure 4 - 28 (c)) results from the multiplication, voxel to voxel, of NLXP and XA matrices at each projection angle.

These corrections were applied to the cube phantom of  $40\ \mu\text{m}$ , leading to an accuracy  $\leq 1.1\%$  for the calculated mass density of phosphorus, compared to the reference phantom [2].

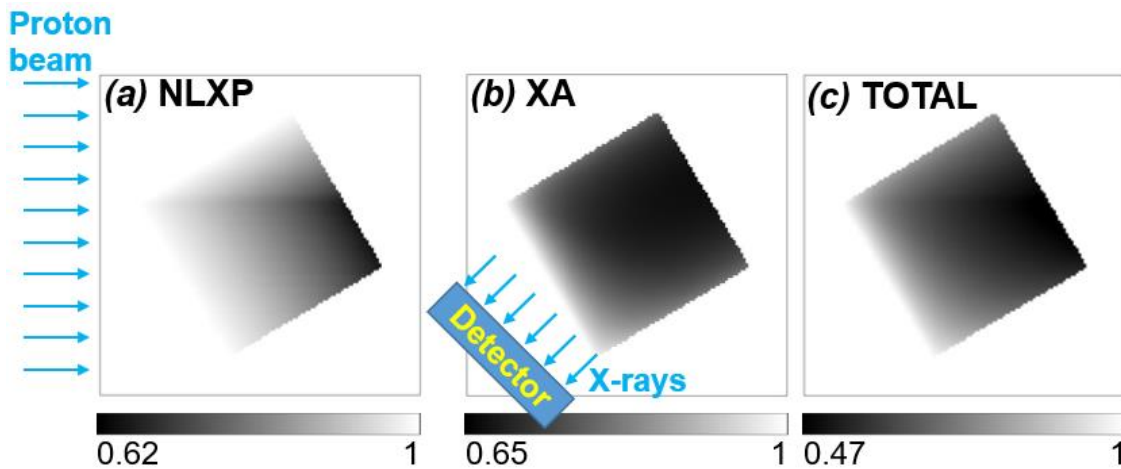


Figure 4 - 28. Correction matrices obtained for phosphorus in the cube phantom of  $40\ \mu\text{m}$ , at projection  $17\ (30.6^\circ)$  arbitrarily taken as an example. Proton energy loss causes NLXP when going deeper in the sample (a); XA correction depends on the position of the emitting voxels according to the X-ray detector (b). The combination of NLXP and XA gives the final correction matrix (c). A linear grey scale was used to code correction values, from black (maximal correction) to white (1, i.e., no correction).

### **5.2.3. Phosphorus and titanium densities for *C. elegans***

PIXE-T simulations were performed for the slice of interest of the *C. elegans* phantom, as shown in Figure 4 - 17. In order to limit the simulation duration to a few days, we considered the following conditions:

- We used a large detection angle ( $70^\circ$  half apex angle) as explained in section 2.4.3;
- We artificially increased the chemical element content in the *C. elegans* phantom: the mass density of P, S, Cl, K, Ca was multiplied by a factor of 10 and the Ti content by a factor of 1000 compared to the original values shown in Table 4 - 2;
- Two X-ray detectors were considered, placed at “typical” (experimental) angles: the first one at  $135^\circ$  from the incident beam, and the second one at  $315^\circ$ , as indicated in Table 4 - 7 [2].

The images of all elements of interest (P, S, Cl, K, Ca, Ti in Figure 4 - 29) were reconstructed taking into account NLXP and XA corrections.

Table 4 - 12 summarizes the results under standard conditions obtained for the lightest (phosphorus,  $Z = 15$ ) and heaviest (titanium,  $Z = 22$ ) elements with and without taking into account the corrections. These elements were chosen for comparison purpose, because XA is expected to be highest for low  $Z$  elements (low X-ray energy) whereas NLXP is expected to be highest for high- $Z$  elements. The RD obtained without taking into account the correction was very high, up to -38% for P. As expected for P, the main difference originates from XA: after correcting XA, the RD dropped to -12%. On the contrary, as expected for Ti, the underestimation of mass density mainly comes from NLXP: the RD dropped to -8.7% with NLXP correction. Taking into account both NLXP and XA corrections, a very good agreement was obtained between reconstructed and reference densities (RD = 3.7% for P and -2.9% for Ti). The sources of error in the reconstruction process include data reduction, MLEM reconstruction and calculation of NLXP and XA correction matrices. These results emphasize an important point: it is commonly believed that PIXE-T images of low  $Z$  elements (such as P) would be more affected by attenuation processes and, for this reason, would require a stronger correction than higher  $Z$  elements. We can notice, thanks to this example, that this argument is indeed relevant regarding XA. However, the underestimation due to NLXP may be of the same order of magnitude for higher  $Z$  elements (such as Ti), and the NLXP effect would lead to a huge discrepancy in the quantification of element content if it is not corrected.

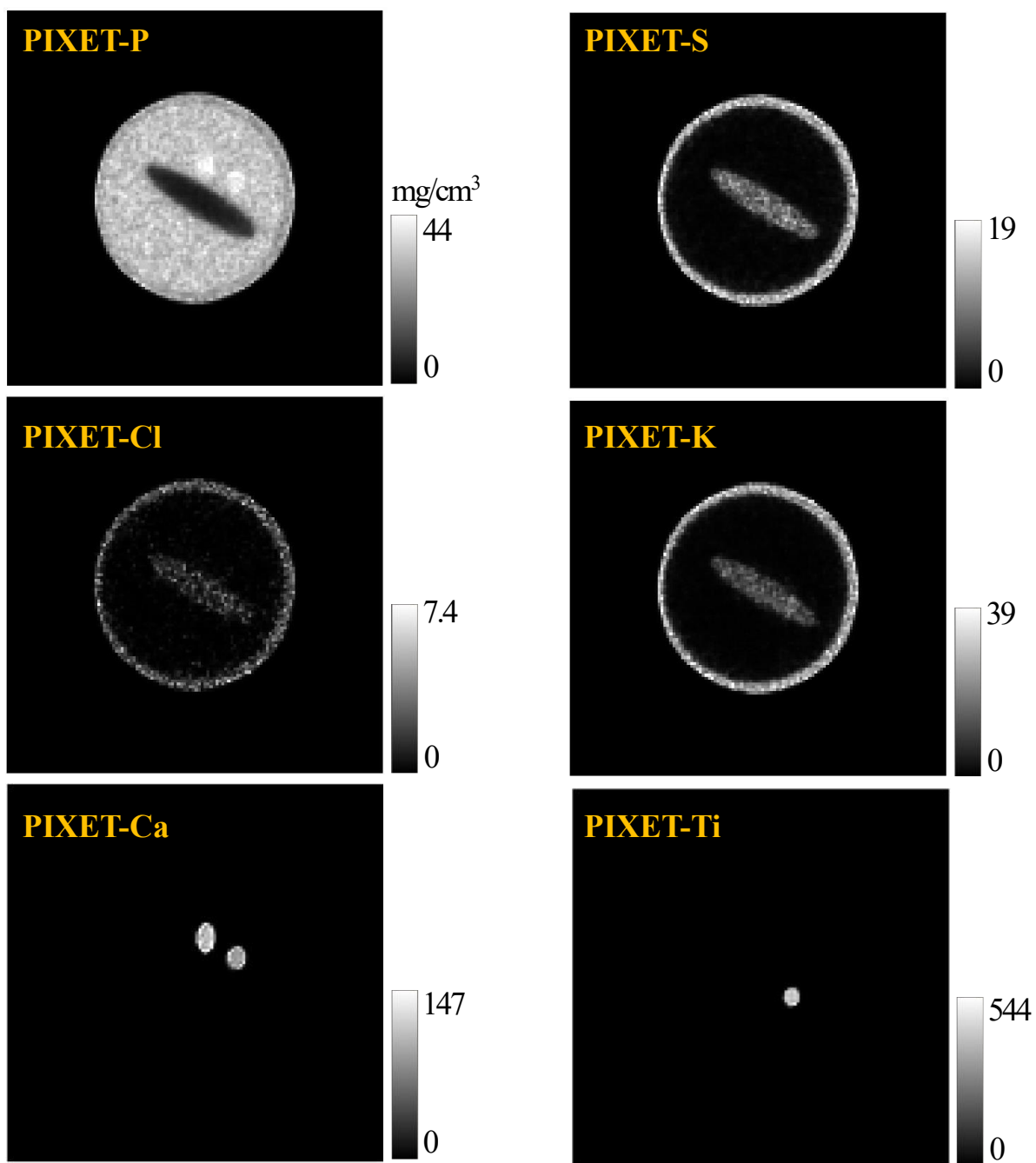


Figure 4 - 29. Reconstructed mass density distributions of elements phosphorus, sulphur, chlorine, potassium, calcium and titanium in the *C. elegans* phantom, taking into account both NLXP and XA corrections. A linear grey scale was used to code mass density values in the slice, from black (density = 0) to white (maximal density).

Table 4 - 12. Mean phosphorus and titanium mass density values in the *C. elegans* phantom, obtained from simulations under standard conditions and reconstructed using MLEM method with and without taking into account the NLXP and XA corrections independently and together. The results were compared with the reference data. The considered ROI are “Body” for phosphorus and “Ti rich region” for titanium, as displayed in Figure 4 - 21 (b).

	P mean density (mg/cm <sup>3</sup> )	Relative difference (%)	Ti mean density (mg/cm <sup>3</sup> )	Relative difference (%)
<b>No correction</b>	18.4 ± 1.8	-38	276 ± 22	-33
<b>NLXP correction only</b>	21.5 ± 2.0	-28	<b>374 ± 29</b>	<b>-8.7</b>
<b>XA correction only</b>	<b>26.2 ± 2.4</b>	<b>-12</b>	294 ± 24	-29
<b>Total correction</b>	<b>30.6 ± 2.7</b>	<b>3.7</b>	<b>398 ± 31</b>	<b>-2.9</b>
<b>Reference value</b>	<b>29.5</b>		<b>409</b>	

#### 5.2.4. Validation of NXLP and XA corrections for *C. elegans*

As explained in section 2.3.6, Geant4’s flexibility allows one to make simulations both under standard and non-standard conditions so that we can access four types of X-ray data (Table 4 - 13), which can be employed to study the effects of NLXP and XA corrections independently. As expected, we observed a significant improvement of the calculated mass density when the required correction was considered and applied. For example, in case 2, the NLXP effect was excluded in the simulation. So the XA correction was the only one required here. If the XA correction was not applied, the calculated density of phosphorus (the most sensitive to XA as explained in section 5.2.3) was, as expected, underestimated (RD -27%). The RD dropped to 4% with the XA correction. Moreover, in case 3, the XA effect was excluded in the simulation. So the NLXP correction was the only one required here. If the NLXP correction was not applied, the calculated density of titanium (the most sensitive to NLXP as explained in section 5.2.3) was, as expected, underestimated (RD -28%). The RD dropped to -1.9% with the NLXP correction. These results not only reflected the necessity but also the effectiveness of the NLXP and XA corrections taken independently or together.

Table 4 - 13. Mean phosphorus and titanium mass density values in the *C. elegans* phantom, obtained from four types of PIXE-T simulated data, reconstructed using MLEM method with and without taking into account independently and totally the NLXP and XA corrections, and compared with the reference data. The considered ROI are “Body” for phosphorus and “Ti rich region” for titanium, as displayed in Figure 4 - 21(b). The uncertainty indicated for each calculated average density corresponds to the standard deviation in the ROI.

PIXE-T data type	Correction implemented	P mean mass density (mg/cm <sup>3</sup> )	Relative difference (%)	Ti mean mass density (mg/cm <sup>3</sup> )	Relative difference (%)
<b>Case 1: both NLXP and XA excluded</b>	No correction required	30.4 ± 1.8	2.9	405 ± 35	-1.1
<b>Case 2: NLXP excluded</b>	XA correction required and applied	<b>30.7 ± 2.3</b>	<b>4.0</b>	401 ± 34	-2.1
	Test without XA correction	<b>21.6 ± 1.7</b>	<b>-27</b>	377 ± 32	-8.0
<b>Case 3: XA excluded</b>	NLXP required and applied	30.4 ± 3.4	3.1	<b>402 ± 29</b>	<b>-1.9</b>
	Test without NLXP correction	26.1 ± 2.0	-12	<b>297 ± 23</b>	<b>-28</b>
<b>Case 4: NLXP and XA not excluded</b>	Both NLXP and XA required and applied	30.6 ± 2.7	3.7	398 ± 31	-2.9
	Test without any correction	18.4 ± 1.8	-38	276 ± 22	-33
<b>Reference value</b>		<b>29.5</b>		<b>409</b>	

### 5.2.5. Mass density of chemical elements for *C. elegans*

Mean mass density values were calculated from PIXE-T simulations under standard conditions, *i.e.*, in similar conditions as experiments, considering the detection of X-rays going out of the *C. elegans* phantom. The mean mass density was obtained for P, S, Cl, K, Ca, Ti in the different ROI displayed in Figure 4 - 21 (b). Table 4 - 14 summarizes the results with and without the required NLXP and XA corrections, compared to the reference values. The discrepancy between the mean mass density calculated in the different ROI went up to 51% without correction. This huge discrepancy was efficiently corrected by using the NLXP and XA correction implemented in TomoRebuild, leading to a satisfactory agreement between calculated densities and reference values, with RD ≤ 10%. The highest RD(s) occur in small (or thin) ROI, for instance the Ti rich region, particularly prone to partial volume effect, *i.e.*, the density values in the ROI were affected by the contiguous regions.



Table 4 - 14. Mean mass density values obtained from the reconstructed PIXE-T images of P, S, Cl, K, Ca, Ti in the *C. elegans* phantom, with and without NLXP and XA corrections, compared to the reference values. The uncertainty indicated for each calculated average density represents the standard deviation in the ROI.

Chemical element	Region of interest	No corrections		NLXP & XA		Reference mass density (mg/cm <sup>3</sup> )
		Mean mass density (mg/cm <sup>3</sup> )	Relative difference (%)	Mean mass density (mg/cm <sup>3</sup> )	Relative difference (%)	
P	Body	18.4±1.8	-38	<b>30.6±2.7</b>	<b>3.7</b>	<b>29.5</b>
	Nucleus 1	20.1±1.4	-47	<b>38.2±2.6</b>	<b>1.9</b>	<b>37.5</b>
	Nucleus 2	19.81±0.80	-47	<b>36.2±1.5</b>	<b>-1.4</b>	<b>36.7</b>
S	Intestine	3.11±0.75	-51	<b>6.0±1.4</b>	<b>-5.5</b>	<b>6.33</b>
	Region Ti	4.3±1.3	-46	<b>8.3±2.4</b>	<b>5.3</b>	<b>7.88</b>
Cl	Intestine	0.72±0.45	-42	<b>1.24±0.76</b>	<b>2.1</b>	<b>1.22</b>
	Region Ti	0.97±0.55	-40	<b>1.70±0.95</b>	<b>5.3</b>	<b>1.61</b>
K	Intestine	7.2±1.8	-33	<b>11.6±2.8</b>	<b>7.7</b>	<b>10.8</b>
	Region Ti	9.1±2.3	-33	<b>14.8±3.5</b>	<b>10</b>	<b>13.4</b>
Ca	Nucleus 1	73.1±7.1	-29	<b>98.0±9.5</b>	<b>-4.6</b>	<b>103</b>
	Nucleus 2	59.9±5.3	-32	<b>80.3±6.8</b>	<b>-7.7</b>	<b>87.0</b>
Ti	Region Ti	276±22	-33	<b>398±31</b>	<b>-2.9</b>	<b>409</b>

### 5.2.6. Validation of NXLP and XA corrections for ICF target phantom

In the previous sections, we have validated the effectiveness of the NLXP and XA corrections on the phantoms composed of biological material, *e.g.*, *C. elegans*. In the framework of a collaboration with Fudan University, our aim was also to validate whether these corrections are suited to ICF targets. Thus, PIXE-T simulations under non-standard conditions were performed for the central slice of the ICF target phantom. Following an approach similar to that of *C. elegans* phantom, we obtained 4 types of PIXE-T data, as described in section 2.3.6. We compared them with the reference data to validate the NXLP and XA corrections independently and together (Table 4 - 15). As expected, NLXP correction is prominent compared to XA for Ge, which is a high Z element. In case 3, the XA effect was excluded in the simulation. So the NLXP correction was the only one required here. If the NLXP correction was not

applied, the calculated mass density of germanium was, as expected, underestimated (RD -39%). The RD dropped to -3.3% with the NLXP correction. Moreover, in case 4, corresponding to the standard conditions where both NLXP and XA corrections were required, the reconstructed mass density with both corrections was in a good agreement (RD -2.9%) with the reference value. These results validated the effectiveness of the TomoRebuild reconstruction using a large solid angle for the ICF target.

*Table 4 - 15. Ge mean mass density values obtained from four types of PIXE-T, with and without taking into account the NLXP and XA corrections, and compared with the reference data. The mean mass density is the mean mass value of ROI 1-4 in Figure 4 - 26. The indicated uncertainty corresponds to the standard deviation.*

<b>PIXE-T data type</b>	<b>Correction implemented</b>	<b>Ge mean mass density (mg/cm<sup>3</sup>)</b>	<b>Relative difference (%)</b>
<b>Case 1:</b> both NLXP and XA excluded	No correction required	53.2 ± 2.9	-1.7
<b>Case 2:</b> NLXP excluded	XA correction required and applied	53.4 ± 2.9	-1.3
	Test without XA correction	52.1 ± 2.9	-3.7
<b>Case 3:</b> XA excluded	NLXP required and applied	<b>52.3 ± 3.4</b>	<b>-3.3</b>
	Test without NLXP correction	<b>33.5 ± 3.7</b>	<b>-39</b>
<b>Case 4:</b> NLXP and XA not excluded	Both NLXP and XA required and applied	52.5 ± 3.4	-2.9
	Test without any correction	32.9 ± 3.6	-40
<b>Reference value</b>		<b>54.0</b>	

### 5.2.7. Comparison of reconstructed images for ICF target between TomoRebuild and JPIXET

As mentioned in section 3.1.3, the main purpose of our study on the ICF target is to test the ability of the different reconstruction methods implemented in the TomoRebuild and JPIXET software packages to produce accurate quantitative images of ICF targets using a large solid angle for the collection of X-rays. Thus, we performed a comparative study between these two codes [14].

For JPIXET, the reconstruction associates the information from STIM-T and PIXE-T at each iteration and for all elements together. The distributions of element content obtained from PIXE-T are used to calculate the stopping power and X-ray absorption of the material at each iteration. The element content (major and minor elements) is normalized at each iteration, so that the sum of all mass fractions is 1. In this way, JPIXET can be used for samples that are not homogeneous in composition. However, a special attention should be paid to the reliability of each element content, as an error occurring on a specific chemical element would propagate to the other elements as well. Here, of course, as there is only one element in the PIXE-T data (Ge), we do not have this concern.

The PIXE-T reconstructed images of Ge mass density obtained by TomoRebuild (TR\_MLEM) and JPIXET are displayed in Figure 4 - 30. As small reconstruction inaccuracies are not clearly visible directly in the reconstructed images, we calculated the difference images (Figure 4 - 31):

*Difference image = Reconstructed image - Reference image.*

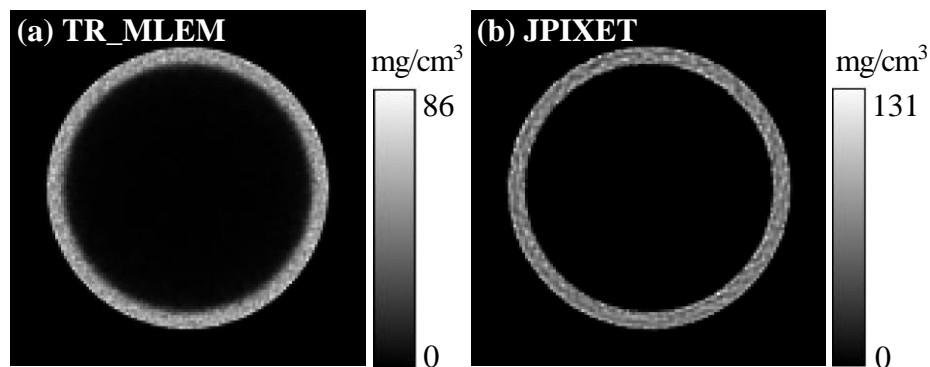


Figure 4 - 30. Reconstructed PIXE-T images using TR\_MLEM (a) and JPIXET (b). The images are displayed here with no additional filter nor threshold, so that they can be directly compared to the voxelized version of the original phantom, as shown in Figure 4 - 31.

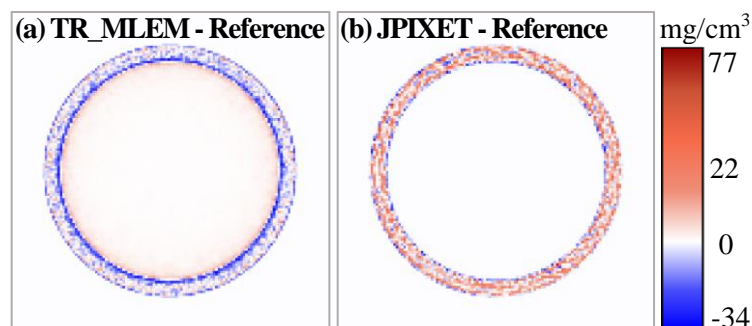


Figure 4 - 31. PIXE-T difference images obtained using TR\_MLEM (a) and JPIXET (b), compared to the original phantom. The same linear color scale was used for the two images for comparison purpose.

Moreover, in order to perform a quantitative comparison, we calculated the Ge mass density in the different ROI (Figure 4 - 32). We observed there was no significant difference for Ge mass density in ROI 1-4, thus, we considered the mean mass density of ROI 1-4 for the comparison of the two reconstruction methods (Table 4 - 16). We observed that for the outer background, both TR\_MLEM and JPIXET produced the expected density 0 (Figure 4 - 31). For the inner background, the density obtained by TR\_MLEM was close to 0 (Figure 4 - 31 and Figure 4 - 32), while exactly 0 for JPIXET. For the shell region, TR\_MLEM gave a more accurate calculated density (RD -2.9%) than JPIXET (RD 6.4%) (Table 4 - 16). Moreover, the density obtained by TR\_MLEM was more uniform than JPIXET: the density fluctuations were found about 40% larger with JPIXET than for TR\_MLEM (Figure 4 - 32 ROI 1-4). However, the definition of borders was better with JPIXET. In summary, TomoRebuild produced more accurate mass density than JPIXET, compared to the original phantom used as a reference. However, a particular attention should be paid to the borders of the shell, which were better defined with JPIXET.

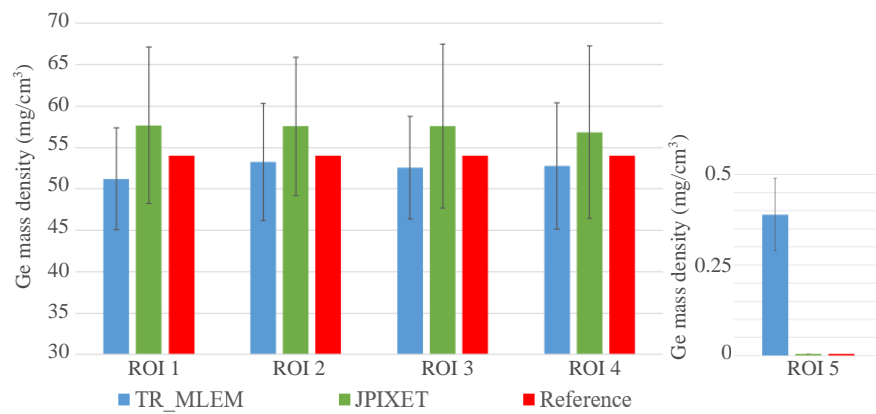


Figure 4 - 32. Histogram of the Ge mass density in ROI 1-5 (displayed in Figure 4 - 26), obtained using different reconstruction methods, compared to the density of the original phantom. ROI 6 was not included because the calculated densities were very close to 0. The error bars correspond to the standard deviation.

Table 4 - 16. Ge mass density in ROI 1-5, obtained using TR\_MLEM and JPIXET methods, compared to the density of the original phantom. The indicated uncertainty corresponds to the standard deviation.

	Ge mean mass density (mg/cm <sup>3</sup> )	Relative difference (%)
TR_MLEM	52.5 ± 3.4	-2.9
JPIXET	57.5 ± 4.8	6.4
<b>Reference value</b>	<b>54.0</b>	

## 6. Conclusion

In this chapter, firstly we demonstrate the application of the Geant4 simulation toolkit as a benchmark for proton micro-tomography. Geant4 simulations produce simulated results that are completely independent of the reconstruction process, so the results can be used to check the accuracy of reconstruction methods. A main achievement is that the NLXP and XA corrections, implemented TomoRebuild for the compensation of X-ray attenuation, have been validated. This study took advantage of Geant4's flexibility. Indeed, Geant4 allows one to have access to data that are impossible to obtain in experiments: *i*) X-rays at the position where they are emitted, for which the XA effect is excluded; *ii*) X-rays generated considering no proton energy loss, for which the production cross-section is constant, *i.e.*, the NLXP effect is excluded.

Secondly, our results also showed the ability of STIM-T and PIXE-T techniques to quantify accurately the mass density and element content in microscopic samples using the reconstruction methods in TomoRebuild:

- For the cube of 5  $\mu\text{m}$  as a thin sample, a good agreement with the original phantom was obtained, with an accuracy  $\leq -2.5\%$  for phosphorus mass density;
- For the cube of 40  $\mu\text{m}$  as a thick sample, the X-ray attenuation due to NLXP and XA was not negligible ( $\sim 35\%$ ) and required relevant corrections. Taking into the NLXP and XA corrections, an accuracy  $\leq 1.1\%$  was obtained for the calculated mass density of phosphorus, compared to the reference phantom;
- For the *C. elegans* phantom, a good agreement for phosphorus (the most sensitive to XA effect) and titanium (the most sensitive to NXLP effect) between reconstructed and reference mass densities was obtained taking into account the NLXP and XA corrections. An accuracy  $\leq 4\%$  for phosphorus and  $\leq -3\%$  for titanium mass density was obtained, whereas the discrepancy was  $-38\%$  and  $-33\%$  respectively for phosphorus and titanium.

We also compared the performance of the two reconstruction software packages, TomoRebuild, and JPIXET, which are the only codes, at present, that are able to take into account large solid angles in the reconstruction process. This study was carried out for the quantification of germanium content in an ICF target. So far, the reconstruction of the ICF target had been performed using a program, which did not take into account the solid angle of the detector, assumed as a point [6, 7]. This assumption required having a small solid angle for the detection in experiments, which led to a long experimental duration ( $\sim 20\text{h}$ ). So using TomoRebuild or JPIXET would be an advantage, because it could significantly reduce the duration of experiments. An accuracy of germanium mass density  $\leq -2.9\%$  for TomoRebuild and  $\leq 6.4\%$  for JPIXET was obtained, taking into account the NLXP and XA corrections. However, JPIXET gave better definition for the borders of the phantom. So, this study validated the efficiency of the reconstruction using TomoRebuild and JPIXET in case of large solid angle.

The development of the *stim\_pixe\_tomography* application was performed in the frame of the international Geant4 collaboration, in agreement with the Advanced Examples working group. A public release of this application, as an advanced example of Geant4, is planned in June 2023. Although the first purpose of this advanced example is to simulate proton micro-tomography, it is worth pointing out that it would be suited to other applications. For example, it could be used to simulate experiments of “classical” (2D) STIM and PIXE imaging, to check their accuracy. Moreover, Geant4 already contains all physical processes for many types of particles, including ions and X-rays in a wide energy range. Thus, other particle sources can be directly used in our simulation code.

## References

- [1] Michelet C, Li Z, Yang W, Incerti S, Desbarats P, Giovannelli J-F, et al. A Geant4 simulation for three-dimensional proton imaging of microscopic samples. *Phys Med.* 2019;65:172-80. <https://doi.org/10.1016/j.ejmp.2019.08.022>.
- [2] Michelet C, Li Z, Jalenques H, Incerti S, Barberet P, Devès G, et al. A Geant4 simulation of X-ray emission for three-dimensional proton imaging of microscopic samples. *Phys Med.* 2022;94:85-93. <https://doi.org/10.1016/j.ejmp.2021.12.002>.
- [3] Habchi C, Gordillo N, Bourret S, Barberet P, Jovet C, Moretto P, et al. Beyond filtered backprojection: A reconstruction software package for ion beam microtomography data. *Nucl Instrum Methods Phys Res B.* 2013;295:42-9. <https://doi.org/10.1016/j.nimb.2012.10.006>.
- [4] Michelet C, Barberet P, Devès G, Bouguelmouna B, Bourret S, Delville M-H, et al. Quantitative reconstruction of PIXE-tomography data for thin samples using GUPIX X-ray emission yields. *Nucl Instrum Methods Phys Res B.* 2015;348:92-9. <https://doi.org/10.1016/j.nimb.2014.11.035>.
- [5] Devès G, Ortega R. Subcellular mass determination by  $4\text{He}^+$  energy-loss micro-spectrometry. *Anal Bioanal Chem.* 2002;374(3):390-4. <https://doi.org/10.1016/10.1007/s00216-002-1511-8>.
- [6] Lu H, He X, Meng J, Guo N, Rong C, Zhang W, et al. Reconstruction of Ge spatial distribution in ICF target using PIXE-T. *Fusion Eng Des.* 2016;113:43-50. <https://doi.org/10.1016/j.fusengdes.2016.10.006>.
- [7] Guo N, Lu H, Wang Q, Meng J, Gao D, Zhang Y, et al. A dual-PIXE tomography setup for reconstruction of Germanium in ICF target. *Nucl Instrum Methods Phys Res B.* 2017;404:162-6. <https://doi.org/10.1016/j.nimb.2017.04.041>.
- [8] Beasley DG, Marques AC, Alves LC, R.C. Fast simulation of Proton Induced X-Ray Emission Tomography using CUDA. *Nucl Instrum Methods Phys Res B.* 2013;306:109-12. <https://doi.org/10.1016/j.nimb.2012.12.053>.
- [9] Beasley DG, Alves LC, Barberet P, Bourret S, Devès G, Gordillo N, et al. A comparison of quantitative reconstruction techniques for PIXE-tomography analysis applied to biological samples. *Nucl Instrum Methods Phys Res B.* 2014;331:248-52. <https://doi.org/10.1016/j.nimb.2014.01.028>.
- [10] Michelet C, Barberet P, Desbarats P, Giovannelli JF, Schou C, Chebil I, et al. An implementation of the NiftyRec medical imaging library for PIXE-tomography reconstruction. *Nucl Instrum Methods Phys Res B.* 2017;404:131-9. <https://doi.org/10.1016/j.nimb.2017.01.067>.
- [11] Michelet C, Barberet P, Moretto P, Sez nec H. Development and applications of STIM- and PIXE-tomography: A review. *Nucl Instrum Methods Phys Res B.* 2015;363:55-60. <https://doi.org/10.1016/j.nimb.2015.08.070>.
- [12] Incerti S, Barberet P, Dévès G, Michelet C, Francis Z, Ivantchenko V, et al. Comparison of experimental proton-induced fluorescence spectra for a selection of thin high-Z samples with Geant4 Monte Carlo simulations. *Nucl Instrum Methods Phys Res B.* 2015;358:210-22. <https://doi.org/10.1016/j.nimb.2015.06.029>.

- [13] Bearden JA. The Scale of X-Ray Wavelengths. *Phys Rev.* 1935;47(11):883-4. <https://doi.org/10.1103/PhysRev.47.883>.
- [14] Li Z, Incerti S, Beasley D, Shen H, Wang S, Seznec H, et al. Accuracy of three-dimensional proton imaging of an inertial confinement fusion target assessed by Geant4 simulation. *Nucl Instrum Methods Phys Res B.* 2023;536:38-44. <https://doi.org/10.1016/j.nimb.2022.12.026>.
- [15] Van Laere K, Koole M, Lemahieu I, Dierckx R. Image filtering in single-photon emission computed tomography: principles and applications. *Comput Med Imaging Graph.* 2001;25(2):127-33. [https://doi.org/10.1016/s0895-6111\(00\)00063-x](https://doi.org/10.1016/s0895-6111(00)00063-x).





## Chapter 5: Conclusions and perspectives

---

In conclusion, this thesis firstly described in chapter 2 the implementation of the EPICS2017 database for Geant4 Livermore photon models. The models regarding four photon processes have been updated using EPICS2017 photon data, which are either directly read by the models, or used through a parameterization:

- For the gamma conversion: the total cross-section data have been updated in format of tabulated points for *G4LivermoreGammaConversionModel* and *G4LivermoreGammaConversion5DModel*. The number of the updated cross-section points is increased (by a factor of about three) in order to be suited to linear interpolation;
- For Compton effect:
  - The total cross-section data are updated for *G4LivermoreComptonModel* in format of tabulated points with more points (also by a factor of about three);
  - The parameterization for scattering function data is updated and improved with new fitting parameters. The scattering function is fitted in two regions regarding the momentum transfer (region 1 for low momentum transfer, and region 2 for high). The precision of the updated parameterization of scattering function, in terms of mean relative difference of fitted values compared to tabulated values on all elements ( $Z$ : 1-100), is improved compared to Geant4 10.6, by a factor of roughly 1000 for region 1 and 2.8 for region 2.
- For the photoelectric effect: the total and subshell cross-section data are updated for *G4LivermorePhotoElectricModel*, according to the incident photon energy, which is separated in 4 consecutive regions:
  - In regions 1 and 2: the total cross-section is accessed in format of tabulated points;
  - In regions 3 and 4: the total and subshell cross-sections are parameterized. The precision of the parameterization is slightly improved by a factor of 1.9 for region 3 and 1.3 for region 4.
- For Rayleigh scattering:
  - The total cross-section is updated for *G4LivermoreRayleighModel* in format of tabulated points;
  - The parameterization of the form factor used for the calculation of the angular distribution of the scattered photon is updated. The precision of the parameterization is improved by a factor of 1.3.

The implementation of updated photon models is validated through a comparative study with respect to the XCOM database. In this study, we calculate the mass attenuation coefficient for both total photon

interaction and each process, using Geant4 10.6 (implementing EPDL97) and the updated models based on EPICS2017. The results obtained from the simulations are found in good agreement with the XCOM data. As a result, the updated photon models have been available since the public release of Geant4 11.0 in December 2021. However, if users wish to use the EPDL97 database in Livermore models for comparison purpose, a UI command “*/process/em/LivermoreData argument*”, where *argument* refers to either “*livermore*”, or “*epics\_2017*”, allows one to choose EPDL97 or EPDL2017 for cross-section data.

The implementation of EPICS2017 in Livermore models has been carried-out in the frame of two research groups of the Geant4 collaboration: the Electromagnetic Physics Working Group and Medical Simulation Benchmarking (G4-Med) group. It has been presented in four Geant4 Collaboration Meetings [C1<sup>7</sup>-C4] and led to two publications in peer-reviewed journals [P1, P2] and one is currently in progress. [P6]. Moreover, we have recently updated the Livermore photon models (released in 2021) in response to the evolution of the requirements in terms of C++ code format recommended by the Electromagnetic Physics working group, for the new Geant4 version released in June 2023.

Secondly in chapter 3, the thesis presented the modification of electron data (EEDL2017) in EPICS2017, compared to the previous version (EEDL91). Differences were only observed for ionisation and excitation cross-sections at low energy, due to the modifications of binding energies of outer subshells. The impact of those changes on Livermore ionisation model was studied by comparing the cross-section and stopping power obtained from EEDL2017 and those calculated from the existing Livermore model, based on EEDL91. A good agreement was found. As a result, we conclude that it is not necessary to update Livermore electron models with the EPICS2017 database.

Lastly in chapter 4, the thesis showed the application of Livermore models for the simulation of proton micro-tomography imaging. More precisely, we designed a benchmark simulation to evaluate the accuracy of the reconstruction methods used to obtain the tomographic images. The first step of this development was to design numerical phantoms with density and composition derived from experimental data. Then, we simulated the STIM-T and PIXE-T experiments and obtained the simulated projections that were used as an input for the reconstruction of images. The obtained tomographic images were then compared with the original numerical phantom. In this way, we assessed the accuracy of the calculated density values and the effectiveness of the X-ray attenuation corrections implemented in the reconstruction codes. The validation of the corrections took advantage of Geant4’s flexibility, which allows one to have access to data that are impossible to obtain in experiments: *i*) X-rays at the position where they are emitted, for which the XA (X-ray absorption) effect is excluded; *ii*) X-rays generated considering no proton energy loss, for which

---

<sup>7</sup> The reference number refers to the “Publications and Conferences” presented in the next section.

the production cross-section is constant, *i.e.*, the NLXP (Non-linear X-ray production) effect is excluded. In this study, we also showed the ability of STIM-T and PIXE-T techniques to quantify accurately the mass density and element content in microscopic samples. For example, for the *C. elegans* phantom, an accuracy  $\leq 4\%$  for phosphorus and  $\leq -3\%$  for titanium mass density were obtained when the corrections were taken into account, whereas the discrepancy was  $-38\%$  and  $-33\%$  respectively when the corrections were not considered. In addition, our simulation application, named *stim\_pixe\_tomography* has been included as a Geant4 advanced example in the public release of Geant4 planned in June 2023. This example is the first one dedicated to micro-tomography simulations. Although it has been initially designed for STIM and PIXE tomography, it is also suited to “classical” (2D) STIM and PIXE imaging. Moreover, it is applicable to different types of incident particles, for instance ions, X-rays or electrons. This work has resulted in three publications in peer-reviewed journals [P3-P5]. It was also presented as a poster at the ICNMTA 2022 international conference [C1] and in a Geant4 collaboration meeting [O5].

I would like to explore now several perspectives relevant to this PhD, regarding future developments, both on Livermore models and proton micro-tomography.

### **Perspectives for Livermore models**

For Livermore photon models, a first interesting perspective deals with Rayleigh scattering cross-section. As mentioned in chapter 2, we have roughly compared Rayleigh scattering cross-section of EPDL2017 and EPDL97 with some of the experimental data for  $Z = 18$ . The results show that EPDL2017 values are much closer to experimental measurements than EPDL97. This comparison is not complete because it is out of the scope of this PhD project. However, it would be valuable to conduct a comprehensive review of the available experimental data and make a more systematic and precise comparison in future studies to validate the accuracy of EPDL2017 data. The second perspective that we would like to put forward for Livermore models concerns the calculation of cross-sections for materials. At present, the total cross-section of a material is calculated by a linear combination of the atomic cross-sections of each element according to the atomic fractions, since the EPICS2017 data are suited for cold, neutral, isolated atoms. However, for the purpose of improving the precision simulation, it would be interesting to incorporate new sets of cross-sections, based on experimental data or theoretical assumptions, that take into account diverse effects impacting cross-sections, such as density effect, molecular effect and for crystals for instance, binding effect. Such advancements have been achieved in other sub-packages. For example in the Geant4-DNA extension, water is already treated as a molecule. Another extension, MicroElec [1], is aimed to model the effect of ionising radiation in microelectronic components. It describes more precisely the particle-matter interactions, for silicon and several other materials such as Cu, Ge and SiO<sub>2</sub>.

We would like now to give an overview of the application of the updated Livermore photon models described in the present thesis. In fact, the Geant4 electromagnetic (EM) physics processes are employed

extensively in a wide range of simulation applications across various research fields, such as high energy and nuclear physics experiments, beam transport, medical physics, cosmic ray interactions and radiation effects in space. The Geant4 EM physics are built by Geant4 EM constructors and include many alternative physics models. Livermore models are obviously used in the *G4EmLivermorePhysics*, specifically dedicated to the interactions at low energy. However, they are also used by the Geant4 EM standard physics constructors, such as *G4EmStandardPhysics*, which is the default EM physics constructor and *G4EmStandardPhysics\_option4*, which is considered the most accurate. In these standard physics constructors, Livermore models are used by default for photoelectric effect and Rayleigh scattering processes. This is also the case for Geant4-DNA physics constructors, such as *G4EmDNAPhysics*. Hence, the impact of updating these models is significant for the whole Geant4 community.

### **Perspectives for proton micro-tomography**

Regarding the advanced example *stim\_pixe\_tomography*, we initially designed it for the simulation proton micro-tomography experiments, more specifically STIM and PIXE micro-tomography. However, its applications are wider; I would like to point out some of them:

- It is applicable to micro-tomography experiments using different particle sources, for instance electrons and (synchrotron-) X-rays;
- It is also suited for “classical” (2D) imaging, for example in order to check the accuracy of quantitative images obtained with protons (STIM, PIXE), or any other particle source;
- It is useful to optimize the duration of experiments. For instance, as described in chapter 4, it has been used to validate the reconstruction methods using a large solid angle, which enable the placement of the detector in close proximity to the samples during tomography experiments, resulting in substantial reduction in experiment duration. Similarly, the number of incident protons was optimized using this advanced example. It can also be used to optimize other experimental conditions, for example the optimal number of projections;
- It is not limited to samples that are homogeneous in their global composition or composed mainly of light elements, such as biological samples or inertial confinement targets. Our simulation can handle any type of sample, as long as the relevant physics processes involve interactions at the atomic level. However, it is important to note that our simulation does not include molecular or crystal effects.

The *stim\_pixe\_tomography* example will be used by the iRiBio team for future developments aiming at improving reconstruction algorithms. For example, it is planned to develop a new reconstruction algorithm based on artificial intelligence, in order to optimize the operational procedure of micro-tomography experiments. The optimization consists in the simplification of the experimental set-up. At the moment, all experiments of proton micro-tomography in the world use a vertical rotation axis, on top of which the micro-object to be analyzed is fixed. A simpler approach is planned by performing 3D

tomography directly on the cell culture support. This approach necessitates the development of a new reconstruction algorithm tailored to the specific experimental conditions. The *stim\_pixe\_tomography* example will undoubtedly be used to check the accuracy of reconstructed images.

## Reference

[1] Gibaru Q, Inguibert C, Caron P, Raine M, Lambert D, Puech J. Geant4 physics processes for microdosimetry and secondary electron emission simulation: Extension of MicroElec to very low energies and 11 materials (C, Al, Si, Ti, Ni, Cu, Ge, Ag, W, Kapton and SiO<sub>2</sub>). Nucl Instrum Methods Phys Res B. 2021;487:66-77. <https://doi.org/10.1016/j.nimb.2020.11.016>.

# Publications and Conferences

---

## Publications

- Articles published in international peer-reviewed journals

[P1] Li Z, Michelet C, Incerti S, Ivanchenko V, Novak M, Guatelli S, et al. Implementation of the EPICS2017 database for photons in Geant4. *Phys Med.* 2022;95:94-115. <https://doi.org/10.1016/j.ejmp.2022.01.008>.

[P2] Sakata D, Hirayama R, Shin W-G, Belli M, Tabocchini MA, Stewart RD, et al. Prediction of DNA rejoining kinetics and cell survival after proton irradiation for V79 cells using Geant4-DNA. *Phys Med.* 2023;105:102508. <https://doi.org/10.1016/j.ejmp.2022.11.012>.

[P3] Li Z, Incerti S, Beasley D, Shen H, Wang S, Seznec H, et al. Accuracy of three-dimensional proton imaging of an inertial confinement fusion target assessed by Geant4 simulation. *Nucl Instrum Methods Phys Res B.* 2023;536:38-44. <https://doi.org/10.1016/j.nimb.2022.12.026>.

[P4] Michelet C, Li Z, Jalenques H, Incerti S, Barberet P, Devès G, et al. A Geant4 simulation of X-ray emission for three-dimensional proton imaging of microscopic samples. *Phys Med.* 2022;94:85-93. <https://doi.org/10.1016/j.ejmp.2021.12.002>.

[P5] Michelet C, Li Z, Yang W, Incerti S, Desbarats P, Giovannelli J-F, et al. A Geant4 simulation for three-dimensional proton imaging of microscopic samples. *Phys Med.* 2019;65:172-80. <https://doi.org/10.1016/j.ejmp.2019.08.022>.

- Publication in progress

[P6]: G4-Med Group: Recent developments of Geant4 for bio-medical physics applications - to be submitted to *Physica Medica* (2023).

## International conference

[C1] Z. Li, C. Michelet, S. Incerti, P. Barberet, D. Beasley, H. Shen, S. Wang, H. Seznec. Accuracy of 3D quantitative imaging of microscopic samples evaluated by Geant4 simulation. 18<sup>th</sup> International Conference on Nuclear Microprobe Technology and Applications (ICNMTA 2022), September 11-16, 2022 in Ljubljana, Slovenia.

## Oral contributions to collaboration meetings

[O1] Implementation of EPICS2017 models for photons. 25<sup>th</sup> Geant4 Collaboration Meeting, 18-25 September, 2020, online. <https://indico.cern.ch/event/942142/contributions/3984141/>.



[O2] Implementation of EPICS2017 models for photons. Geant4-DNA 2020 Collaboration Meeting, 5<sup>th</sup> February, 2021, online. <https://indico.in2p3.fr/event/22921/contributions/89760/>.

[O3] Implementation of the EPICS2017 database for photons in Geant4. 26<sup>th</sup> Geant4 Collaboration Meeting, 13-24 September, 2021, online. <https://indico.cern.ch/event/1052654/contributions/4524557/>.

[O4] Implementation of the EPICS2017 database for photons in Geant4. Geant4-DNA 2021 Collaboration Meeting, 22<sup>th</sup> December, 2021, online. <https://indico.in2p3.fr/event/25464/contributions/103822/>.

[O5] An advanced example for 3D imaging of microscopic samples by proton tomography. 27<sup>th</sup> Geant4 Collaboration Meeting, 26-30 September 2022, IRISA Laboratory, Rennes, France. <https://indico.cern.ch/event/1156193/contributions/5047041/>.

# International collaborations

---

- For the implementation of EPICS2017 in Livermore models:
  - Vladimir Ivanchenko (Tomsk State University) and Mihaly Novak, Geant4 Electromagnetic Physics Working Group, CERN
  - Susanna Guatelli (University of Wollongong), Geant4 Medical Simulation Benchmarking group (G4-Med)
- For proton micro-tomography:
  - Susanna Guatelli (University of Wollongong), Geant4 Advanced Examples group
  - Hao Shen and Shimei Wang, Key Laboratory of Nuclear Physics and Ion beam Application, Fudan University
  - Daniel Beasley, School of Biomedical Engineering & Imaging Sciences, King's College London



# Appendices

---

## Appendix A: Atomic subshell designators

*Table A - 1: Atomic subshells in EPICS2017 are specified by prescribed floating point designators.*

Designator	Subshell	Designator	Subshell	Designator	Subshell
1	K (1s1/2)	21	N4 (4d3/2)	41	P1 (6s1/2)
2	L (2)	22	N5 (4d5/2)	42	P23 (6p)
3	L1 (2s1/2)	23	N67 (4f)	43	P2 (6p1/2)
4	L23 (2p)	24	N6 (4f5/2)	44	P3 (6p3/2)
5	L2 (2p1/2)	25	N7 (4f7/2)	45	P45 (6d)
6	L3 (2p3/2)	26	O (5)	46	P4 (6d3/2)
7	M (3)	27	O1 (5s1/2)	47	P5 (6d5/2)
8	M1 (3s1/2)	28	O23 (5p)	48	P67 (6f)
9	M23 (3p)	29	O2 (5p1/2)	49	P6 (6f5/2)
10	M2 (3p1/2)	30	O3 (5p3/2)	50	P7 (6f7/2)
11	M3 (3p3/2)	31	O45 (5d)	51	P89 (6g)
12	M45 (3d)	32	O4 (5d3/2)	52	P8 (6g7/2)
13	M4 (3d3/2)	33	O5 (5d5/2)	53	P9 (6g9/2)
14	M5 (3d5/2)	34	O67 (5f)	54	P1011 (6h)
15	N (4)	35	O6 (5f5/2)	55	P10 (6h9/2)
16	N1 (4s1/2)	36	O7 (5f7/2)	56	P11 (6h11/2)
17	N23 (4p)	37	O89 (5g)	57	Q (7)
18	N2 (4p1/2)	38	O8 (5g7/2)	58	Q1 (7s1/2)
19	N3 (4p3/2)	39	O9 (5g9/2)	59	Q23 (7p)
20	N45 (4d)	40	P (6)	60	Q2 (7p1/2)
				61	Q3 (7p3/2)

## Appendix B: Simulation with constant proton energy

```

201 inline void G4Step::UpdateTrack()
202 {
203     // To avoid the circular dependency between G4Track, G4Step
204     // and G4StepPoint, G4Step has to manage the update actions.
205     // position, time
206     fpTrack->SetPosition( aValue: fpPostStepPoint->GetPosition());
207     fpTrack->SetGlobalTime( aValue: fpPostStepPoint->GetGlobalTime());
208     fpTrack->SetLocalTime( aValue: fpPostStepPoint->GetLocalTime());
209     fpTrack->SetProperTime( aValue: fpPostStepPoint->GetProperTime());
210     // energy, momentum, polarization
211     fpTrack->SetMomentumDirection( aValue: fpPostStepPoint->GetMomentumDirection());
212     fpTrack->SetKineticEnergy( aValue: fpPostStepPoint->GetKineticEnergy());
213     fpTrack->SetPolarization( aValue: fpPostStepPoint->GetPolarization());
214     // mass charge
215     G4DynamicParticle* pParticle =
216         (G4DynamicParticle*) (fpTrack->GetDynamicParticle());
217     pParticle->SetMass( newMass: fpPostStepPoint->GetMass());
218     pParticle->SetCharge( newCharge: fpPostStepPoint->GetCharge());
219     // step length
220     fpTrack->SetStepLength( fStepLength);

```

Initial code in *G4Step.icc*

Modified code in *G4Step.icc* (example at 1.5 MeV)

```

201 inline void G4Step::UpdateTrack()
202 {
203     // To avoid the circular dependency between G4Track, G4Step
204     // and G4StepPoint, G4Step has to manage the update actions.
205     // position, time
206     fpTrack->SetPosition( aValue: fpPostStepPoint->GetPosition());
207     fpTrack->SetGlobalTime( aValue: fpPostStepPoint->GetGlobalTime());
208     fpTrack->SetLocalTime( aValue: fpPostStepPoint->GetLocalTime());
209     fpTrack->SetProperTime( aValue: fpPostStepPoint->GetProperTime());
210     // energy, momentum, polarization
211     fpTrack->SetMomentumDirection( aValue: fpPostStepPoint->GetMomentumDirection());
212     if(fpTrack->GetParentID() == 0 && fpTrack->GetDefinition()->GetParticleName() == "proton"){
213         fpTrack->SetKineticEnergy( aValue: 1.5*CLHEP::MeV);
214     }
215     else fpTrack->SetKineticEnergy( aValue: fpPostStepPoint->GetKineticEnergy());
216     fpTrack->SetPolarization( aValue: fpPostStepPoint->GetPolarization());
217     // mass charge

```

Figure B - 1: Modification of *G4Step.icc* Geant4 source code, in order to turn off the proton energy loss process. The proton energy is re-set at its initial value (e.g., 1.5 MeV) after each interaction step.